

CO Multi-line Imaging of Nearby Galaxies (COMING) IV. Overview of the Project

Kazuo SORAI^{1, 2, 3, 4, 5}, Nario KUNO^{4, 5}, Kazuyuki MURAOKA⁶, Yusuke MIYAMOTO^{7, 8}, Hiroyuki KANEKO⁷, Hiroyuki NAKANISHI⁹, Naomasa NAKAI^{4, 5, 10}, Kazuki YANAGITANI⁶, Takahiro TANAKA⁴, Yuya SATO⁴, Dragan SALAK¹⁰, Michiko UMEI², Kana MOROKUMA-MATSUI^{7, 8, 11, 12}, Naoko MATSUMOTO^{13, 14}, Saeko UENO⁹, Hsi-An PAN¹⁵, Yuto NOMA¹⁰, Tsutomu, T. TAKEUCHI¹⁶, Moe YODA¹⁶, Mayu KURODA⁶, Atsushi YASUDA⁴, Yoshiyuki YAJIMA², Nagisa OI¹⁷, Shugo SHIBATA², Masumichi SETA¹⁰, Yoshimasa WATANABE^{4, 5, 18}, Shoichiro KITA⁴, Ryusei KOMATSUZAKI⁴, Ayumi KAJIKAWA^{2, 3}, Yu YASHIMA^{2, 3}, Suchetha COORAY¹⁶, Hiroyuki BAJI⁶, Yoko SEGAWA², Takami TASHIRO², Miho TAKEDA⁶, Nozomi KISHIDA², Takuya HATAKEYAMA⁴, Yuto TOMIYASU⁴ and Chey SAITA⁹

¹Department of Physics, Faculty of Science, Hokkaido University, Kita 10 Nishi 8, Kita-ku, Sapporo 060-0810, Japan

²Department of CosmoSciences, Graduate School of Science, Hokkaido University, Kita 10 Nishi 8, Kita-ku, Sapporo 060-0810, Japan

³Department of Physics, School of Science, Hokkaido University, Kita 10 Nishi 8, Kita-ku, Sapporo 060-0810, Japan

⁴Division of Physics, Faculty of Pure and Applied Sciences, University of Tsukuba, 1-1-1 Tennodai, Tsukuba, Ibaraki 305-8571, Japan

⁵Tomonaga Center for the History of the Universe (TCHoU), University of Tsukuba, 1-1-1 Tennodai, Tsukuba, Ibaraki 305-8571, Japan

⁶Department of Physical Science, Osaka Prefecture University, Gakuen 1-1, Sakai, Osaka 599-8531, Japan

⁷Nobeyama Radio Observatory, Minamimaki, Minamisaku, Nagano 384-1305, Japan

⁸Chile Observatory, 2-21-1 Osawa, Mitaka, Tokyo 181-8588, Japan

⁹Graduate School of Science and Engineering, Kagoshima University, 1-21-35 Korimoto, Kagoshima, Kagoshima 890-0065, Japan

¹⁰Department of Physics, School of Science and Technology, Kwansai Gakuin University, Gakuen 2-1, Sanda, Hyogo 669-1337, Japan

¹¹Institute of Space and Astronautical Science, Japan Aerospace Exploration Agency, 3-1-1 Yoshinodai, Chuo-ku, Sagami-hara, Kanagawa 252-5210, Japan

¹²Institute of Astronomy, Graduate School of Science, The University of Tokyo, 2-21-1 Osawa, Mitaka, Tokyo 181-0015, Japan

¹³The Research Institute for Time Studies, Yamaguchi University, Yoshida 1677-1, Yamaguchi, Yamaguchi 753-8511, Japan

¹⁴Mizusawa VLBI Observatory, National Astronomical Observatory of Japan, 2-21-1 Osawa, Mitaka, Tokyo 181-8588, Japan

¹⁵Institute of Astronomy and Astrophysics, Academia Sinica, 11F of AS/NTU Astronomy-Mathematics Building, No.1, Sec. 4, Roosevelt Rd, Taipei 10617, Taiwan

¹⁶Division of Particle and Astrophysical Science, Nagoya University, Furo-cho, Chikusa-ku,

Nagoya, Aichi 464-8602, Japan

¹⁷Tokyo University of Science, Faculty of Science Division II, Liberal Arts, 1-3, Kagurazaka
Shinjuku-ku Tokyo 162-8601 Japan

¹⁸College of Engineering, Nihon University, 1 Nakagawara, Tokusada, Tamuramachi,
Koriyama, Fukushima 963-8642, Japan

*E-mail: sorai@astro1.sci.hokudai.ac.jp

Received 2018 December 17; Accepted 2019 September 18

Abstract

Observations of the molecular gas in galaxies are vital to understanding the evolution and star-forming histories of galaxies. However, galaxies with molecular gas maps of their whole discs having sufficient resolution to distinguish galactic structures are severely lacking. Millimeter wavelength studies at a high angular resolution across multiple lines and transitions are particularly needed, severely limiting our ability to infer the universal properties of molecular gas in galaxies. Hence, we conducted a legacy project with the 45 m telescope of the Nobeyama Radio Observatory, called the CO Multi-line Imaging of Nearby Galaxies (COMING), which simultaneously observed 147 galaxies with high far-infrared flux in ^{12}CO , ^{13}CO , and C^{18}O $J = 1 - 0$ lines. The total molecular gas mass was derived using the standard CO-to- H_2 conversion factor and found to be positively correlated with the total stellar mass derived from the WISE $3.4\ \mu\text{m}$ band data. The fraction of the total molecular gas mass to the total stellar mass in galaxies does not depend on their Hubble types nor the existence of a galactic bar, although when galaxies in individual morphological types are investigated separately, the fraction seems to decrease with the total stellar mass in early-type galaxies and vice versa in late-type galaxies. No differences in the distribution of the total molecular gas mass, stellar mass, and the total molecular gas to stellar mass ratio was observed between barred and non-barred galaxies, which is likely the result of our sample selection criteria, in that we prioritized observing FIR bright (and thus molecular gas-rich) galaxies.

Key words: galaxies: ISM — galaxies: statistics — atlases — surveys — methods: data analysis

1 Introduction

How and where stars form in galaxies are clues to understanding galaxy evolution, and require information about the distribution, dynamics, and physical properties of their molecular gas content. H II regions and massive stars are found in spiral arms (Lynds 1980; García Gómez & Athanassoula 1993; Thilker et al. 2002; Oey et al. 2003; Bresolin et al. 2005), while only a few are found in the bar of some barred spiral galaxies (Koopmann et al. 2001; James et al. 2004; Hernandez et al. 2005; Erroz-Ferrer et al. 2015). Interacting and merging galaxies often display an abundance of star-forming regions in both their interface regions, especially compared to their spiral arms (Koopmann et al. 2001; Wang et al. 2004; Torres-Flores et al. 2014), while little new stars form even in the spiral arms of some galaxies (van den Bergh 1976; Kennicutt & Edgar 1986; Masters et al. 2010; Fraser-McKelvie et al. 2016). These observational results indicate that star for-

mation is not uniform both within and between different galaxies. Some questions must be answered for us to understand the causes of a variety of star formations within a galaxy and among galaxies.

Many studies have observed the distribution and dynamics of molecular gas in galaxies. Molecular gas in spiral galaxy M51 is primarily concentrated along the two grand-design spiral arms, but also detected in the interarm regions (García-Burillo et al. 1993; Nakai et al. 1994). The velocity of molecular gas qualitatively changes at the spiral arm in accordance with density wave theory, and the estimated elliptical motion can explain the surface density contrast of the molecular gas between the spiral arms and the interarm regions (Kuno & Nakai 1997). Flocculent galaxies also display molecular gas concentrations along their spiral arms, such as in NGC 5055 (Kuno et al. 1997). On-the-fly (OTF) observations of the barred spiral galaxy M83 showed that the CO disc has a sharp edge, while the H I disc more gradually extends to larger radii (Crosthwaite

et al. 2002).

In the recent years, CO observations with high spatial resolution have resolved giant molecular clouds (GMCs) in galaxies. Giant molecular cloud associations (GMAs) are dominant in the spiral arms and broken up into GMCs in the interarm regions in M 51 (Koda et al. 2009). In the barred spiral galaxy NGC 4303, the molecular gas in the bar has a lower star formation efficiency (SFE) than that in the spiral arms, where the SFE is the star formation rate (SFR) divided by the molecular gas mass (Momose et al. 2010). The SFE depends on the environment at sub-kpc scales, and increases with the surface density of the molecular gas (Momose et al. 2013). Meanwhile, in the local spiral galaxy M 33, the molecular gas fractions are loosely correlated with the neutral gas fraction observed at the GMC scales, with particular variations in the inner disc (Tosaki et al. 2011). A CARMA (Combined Array for Research in Millimeter Astronomy interferometer) and Nobeyama Nearby galaxies (CANON) survey resolved approximately 200 GMCs in the inner discs of five galaxies and revealed that they are similar to those in the Milky Way (Donovan Meyer et al. 2013). PAWS (Plateau de Bure Interferometer Arcsecond Whirlpool Survey, Schinnerer et al. 2013) observed M 51 at ~ 40 pc resolution and found that the dynamical environment of the GMCs significantly influences their star-forming capability (Meidt et al. 2013), and that feedback from massive stars affects the dependency of the GMC properties on the environment (Colombo et al. 2014). Observations of M 100 with Atacama Large Millimeter/Submillimeter Array (ALMA) revealed that the GMA properties depend on the environment: GMAs are compact in the circumnuclear region, but diffuse in interarm regions, and their velocity dispersions are higher in the circumnuclear region and the bar than the other regions (Pan & Kuno 2017).

A few notable systematic surveys have mapped gas across the entire surface of galaxies at a sub-kpc resolution. Berkeley-Illinois-Maryland Association millimeter interferometer Survey of Nearby Galaxies, also known as BIMA SONG, imaged 44 nearby galaxies (Helfer et al. 2003) via interferometry and single-dish observations. Meanwhile, the Nobeyama CO Atlas of nearby galaxies (Kuno et al. 2007) mapped 40 galaxies with a single-dish telescope. These observations revealed higher molecular gas concentrations toward the galactic center in barred spiral galaxies compared to unbarred spirals (Sheth et al. 2005; Kuno et al. 2007). Some galaxies located near the center of the Virgo cluster have revealed a higher fraction of molecular gas to the total neutral gas, including H I gas, which is interpreted as ram pressure stripping of H I gas or induced molecular gas formation caused by a higher external pres-

sure in cluster environments (Nakanishi et al. 2006). A total of 28 Virgo cluster spirals were also mapped with the Five College Radio Astronomy Observatory (FCRAO) 14 m telescope (Chung et al. 2009b); however, some galaxies overlap with one another. The total number of mapped galaxies in these three surveys was 74.

Many mapping observations of molecular gas, whose sample size numbers were 10 or fewer, and surveys with interferometers covering only the central regions have also been made [Sakamoto et al. 1999; Sofue et al. 2003; CARMA STING (Survey Toward Infrared-bright Nearby Galaxies), Rahman et al. 2012]. However, combining such data is not necessarily suitable for comparing many galaxies because spatial resolutions and instrument sensitivity can wildly differ between surveys. In addition, observations with interferometers alone miss extended emission (i.e., are “resolved out”); hence, there are concerns that such observations underestimate the total molecular gas mass of the target galaxies. If mapping does not extend across the entirety of the galactic disc, then correct information on the molecular gas and star formation in outer regions, particularly in interacting galaxies, are impossible to obtain.

Surveys targeting higher- J transitions have also been conducted, although they carry added caveats for estimating the total molecular gas masses of the target galaxies. HERACLES (HEterodyne Receiver Array CO Line Extragalactic Survey, Leroy et al. 2009) provided sensitive images of 48 nearby galaxies in ^{12}CO ($J = 2 - 1$). The relation between the surface density and the velocity dispersion of GMCs in nearby galaxies was reported (Sun et al. 2018) based on the recent very high-resolution observations with ALMA in ^{12}CO ($J = 2 - 1$) [PHANGS-ALMA (Physics at High Angular resolution in Nearby Galaxies with ALMA), A. K., Leroy, et al. (in preparation)]. JCMT Nearby Galaxies Legacy Survey (NGLS, Wilson et al. 2012) mapped 155 galaxies in ^{12}CO ($J = 3 - 2$). Such high transition data are particularly useful for excitation analysis combined with $J = 1 - 0$. However, the estimation of the molecular gas mass assuming a constant intensity ratio has a considerable uncertainty (e.g., $J = 2 - 1/J = 1 - 0$) because the ratio is not constant within a galaxy (Sakamoto et al. 1997; Koda et al. 2012; Leroy et al. 2013).

Several single-point observations have provided key insights into the relation between molecular gas content and galaxy morphology and evolution. The FCRAO survey of 300 galaxies reported that the molecular gas distribution against the optical galaxy size depends on morphology (Young et al. 1995). Komugi et al. (2008) observed 68 galaxies. They showed larger central concentrations of molecular gas in earlier-type galaxies and the impact of

the inner bulge on the gas concentrations. Large CO surveys have recently provided clues of galaxy evolution by comparison with stellar mass information. COLD GASS [CO Legacy Data base for the GASS (GALEX Arecibo SDSS Survey)] observed ~ 350 galaxies and showed that the relation between molecular gas fraction and stellar mass strongly depends on $\text{NUV} - r$ color (Saintonge et al. 2011). The Herschel Reference Survey observed 59 galaxies (Boselli et al. 2014a) and illustrated that the molecular gas mass fraction only slightly depends on morphology, but strongly depends on the stellar mass and the specific SFR (Boselli, et al. 2014b). The fraction increases with the redshift in the range of $0 \lesssim z \lesssim 3$ (Daddi et al. 2010; Popping et al. 2012; Saintonge et al. 2013; Popping et al. 2015; Dessauges-Zavadsky et al. 2017), and this evolution depends on the stellar mass (Dessauges-Zavadsky et al. 2015; Morokuma-Matsui & Baba 2015).

We have limited spatially resolved information on the physical conditions of molecular gas (e.g., whether the density and the temperature of molecular gas in GMCs differ between the arm, interarm, and bar regions of disc galaxies). Although the most general tracer of molecular gas in galaxies is ^{12}CO ($J = 1 - 0$), we cannot estimate the molecular gas density and the temperature from a single transition. Molecular lines are excited under various physical conditions; hence, we have to observe multiple lines to constrain the physical conditions of molecular gas. In the case of multiple ^{12}CO line observations, we have to carefully compare the data because the line frequencies are very different from each other, and as a result, different lines are measured with different telescopes or taken at different spatial resolutions. Although we can observe ^{13}CO or C^{18}O lines with the same telescope at nearly the same spatial resolution, these lines are very weak, and mapping the whole disc is a time-consuming task [Watanabe et al. 2011; CARMA STING, Cao et al. 2017; EMPIRE (EMIR Multiline Probe of the ISM Regulating Galaxy Evolution) survey, Cormier et al. 2018]. Such efforts have revealed the properties of molecular gas in several local galaxies. In the bar ends of NGC 3627, the ^{12}CO and ^{13}CO measurements suggest a very high molecular gas density, which results in a very high SFE (Watanabe et al. 2011). In contrast, the $^{12}\text{CO} / ^{13}\text{CO}$ intensity ratios do not clearly correlate with the SFR (Cao et al. 2017). Despite such efforts, a great deal of progress must still be made on understanding how the properties of molecular gas varies both within and between galaxies.

High-resolution and high-sensitivity mapping capabilities have recently expanded targets from local spiral galaxies to early-type or low- z galaxies. The CARMA ATLAS^{3D} molecular gas imaging survey observed 30 early-type galax-

ies and showed various CO morphologies and a wide distribution of $^{13}\text{CO} / ^{12}\text{CO}$ ratios (Alatalo et al. 2013, 2015). Meanwhile, the Evolution of Molecular Gas in Normal Galaxies (EGNoG) survey imaged 31 star-forming galaxies from $z = 0.05$ to $z = 0.5$ and illustrated molecular gas depletion times and fractions (Bauermeister et al. 2013). The Extragalactic Database for Galaxy Evolution (EDGE) – Calar Alto Legacy Integral Field Area (CALIFA) survey (Bolatto et al. 2017) observed 126 relatively distant galaxies and presented a fairly constant molecular-to-stellar mass ratio across spiral galaxies and an approximately linear relation between the resolved surface densities of the SFR and molecular gas. Meanwhile, the Valparaíso ALMA Line Emission Survey (VALES) observed 67 galaxies up to $z = 0.35$ with ALMA and found that the molecular gas distribution is, on average, ~ 0.6 times more compact than the optical size (Villanueva et al. 2017).

We conducted the project CO Multi-line Imaging of Nearby Galaxies (COMING), which is one of the Nobeyama Radio Observatory (NRO) legacy projects, using the 45 m telescope to quantitatively improve our understanding of the spatially resolved, galaxy-scale distribution of molecular gas. The OTF observations with the multi-beam receiver, FOur-beam REceiver System on the 45 m Telescope (FOREST) (Minamidani et al. 2016) enabled us to make efficient maps toward a large number of galaxies. We simultaneously observed the ^{12}CO , ^{13}CO , and C^{18}O lines using the wide intermediate frequency (IF) band of FOREST. Some preliminary results for individual galaxies have already been published (Muraoka et al. 2016; Hatakeyama et al. 2017; Yajima et al. 2019), and this paper presents a project overview. Sections 2 and 3 present the sample selection and observations, respectively. Sections 4 and 5 show the data reduction, analysis software development, data analysis, and archival data, respectively. Section 6 presents the results and discussion. Finally, section 7 summarizes the project overview.

2 Sample

The initial sample selection consisted of 344 far-infrared (FIR) bright galaxies from the “Nearby Galaxies Catalog” (Tully 1988). The number of the CO images of galaxies was much smaller than that in optical or infrared regimes; thus, we gave priority to galaxies expected to be bright in CO, although the completeness of the samples is important in understanding the galaxy evolution. Accordingly, we selected candidates biased to the FIR flux that is known to be well correlated with the CO flux (Young & Scoville 1991) from the Nearby Galaxies Catalog. We used the selection criteria of $100\mu\text{m}$ flux $S_{100\mu\text{m}} \geq 10$ Jy in “IRAS catalogue

of Point Sources” (Helou & Walker 1988) or the $140\ \mu\text{m}$ flux $S_{140\ \mu\text{m}} \geq 10\ \text{Jy}$ in “AKARI/FIS All-Sky Survey Point Source Catalogues” (Yamamura et al. 2010). We checked that all sources common to both samples satisfied both criteria. Elliptical galaxies were removed from our sample candidates even if they satisfied the criteria because CO emission was not expected to be detected within a reasonable observing time. M31 and M33 were also eliminated in spite of satisfying the criteria because both galaxies would require excessively large maps that demanding a long observing time.

Next, we selected galaxies from the abovementioned parent sample, most of which have a large extent in optical images, and have not yet been observed using the 45 m telescope, thereby resulting in 238 galaxies. The sample included galaxies previously observed with the 45 m telescope because we intended to compare our new OTF maps with the previous ones (Muraoka et al. 2016). In addition, some previous observations were less sensitive. This selection was done to increase the number of galaxy CO maps available within a limited observation time. We resolved the galactic structure in detail by assigning a higher priority to galaxies with (1) a large optical diameter (D_{25}), (2) a lower inclination angle when D_{25} is similar, and (3) with former observational works having a higher spatial resolution, such as CANON (Donovan Meyer et al. 2013) (we added Mrk33) or CARMA STING (Rahman et al. 2012). We also included pair galaxies, where only one of the pair satisfies the criteria because the molecular gas in the interacting systems may spread over a wide area, including intergalactic regions (Kaneko et al. 2013). We assigned the priority code (A, B, and C) to the 238 selected galaxies according to the apparent galaxy size with or without previous CO (interferometric) data and interest of individual members of the survey team. Practical constraints, such as available observing time and weather, limited the actual number of the observed galaxies to 147.

Table 1 and figures 1 – 4 show the morphology, optical diameter, distance, position angle (PA) of the major axis, inclination (i) of the galactic disc, and FIR fluxes of the 147 observed galaxies. We adopted the distance of each galaxy from the redshift-independent distances in the NASA/IPAC Extragalactic Database (NED)¹ prioritizing the following: (1) distance with the minimum error of the distance modulus taken after 2013; (2) the same as (1) if no matches, but the latest data taken after 2003; and (3) the same as (2) if no matches, but taken before 2003. The distances of the galaxies identified as members of the Virgo cluster are assumed to be the same value of 16.5 Mpc (Mei et al. 2007). The distances of the interacting galaxies are

¹ (<http://ned.ipac.caltech.edu>).

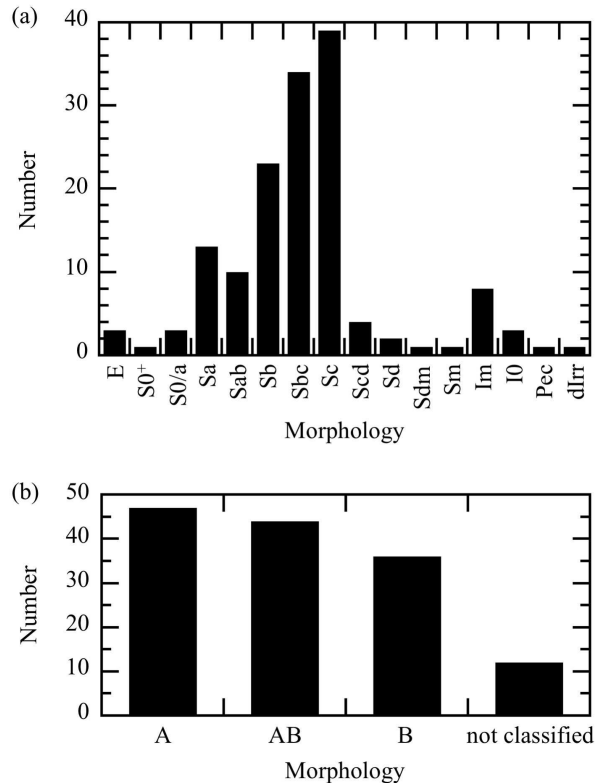


Fig. 1. Morphological type of the sample galaxies: (a) Hubble types and (b) barred or non-barred spirals. The “E” and “Pec” types are not included in panel (b).

considered similar to each other. We adopted PA and i that were measured kinematically and determined at the same time, where possible. When no such data exist, we adopted the pair of PA and i measured by fitting brightness distribution by an ellipse or PA and i measured individually. PA is the receding side of the semi-major axis, unless no kinematical information exists. PA is expressed within $\pm 180^\circ$, where 0° corresponds to the north, and the angle is measured counterclockwise. Our kinematical analysis has shown that PA and i of NGC 2967 are quite different from the data estimated in previous works (Salak et al. 2019); however, we do not adopt the latest values herein.

The observed galaxies have a bias toward Sb to Sc types with few early- and late-type galaxies because constraints on the observing conditions restricted our observation of the entire original sample. The presence or absence of a bar classified as SA, SAB, or SB is distributed throughout the sample. The observation ranking system described in subsection 3.2 particularly selected smaller galaxies because the weather conditions in the last two observation seasons were poor.

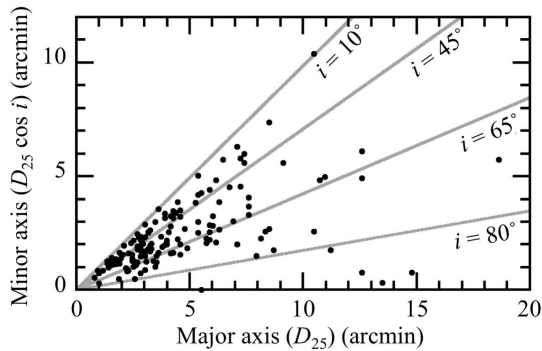


Fig. 2. Apparent optical sizes of the sample galaxies. The gray lines indicate a specified inclination (i).

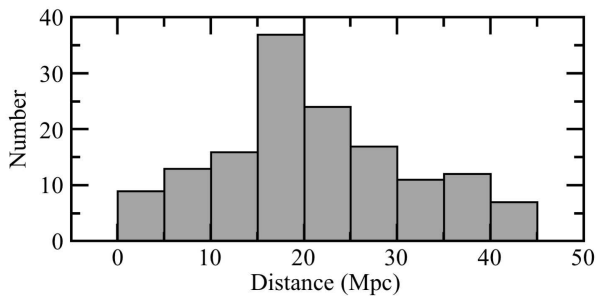


Fig. 3. Distances of the sample galaxies.

3 Observations

The observations were made with the NRO 45 m telescope. Three CO isotopomers were simultaneously observed with the OTF mode. We developed an observation ranking system that objectively selects the optimal target to maximize the survey efficiency. This system was used in the last two seasons.

3.1 System setting and OTF mapping

Simultaneous observations of ^{12}CO ($J = 1 - 0$) (rest frequency: 115.271202 GHz), ^{13}CO ($J = 1 - 0$) (rest frequency: 110.201353 GHz), and C^{18}O ($J = 1 - 0$) (rest frequency: 109.782173 GHz) were made with FOREST over four seasons: from 2015 April to May, from 2015 December to 2016 May, from 2016 December to 2017 May, and from 2017 December to 2018 April (table 2). FOREST has four beams, and each beam can receive dual-polarization 8GHz bandwidth data for each sideband (upper and lower sidebands). The beam size of each beam was $\sim 14''$ in 110GHz and 115GHz bands. SAM45 (Kuno et al. 2011; Kamazaki et al. 2012), which consists of 16 correlators, is available as a backend. We used SAM45 in a wide-band mode with 2GHz bandwidth and 4096 channels corresponding to a

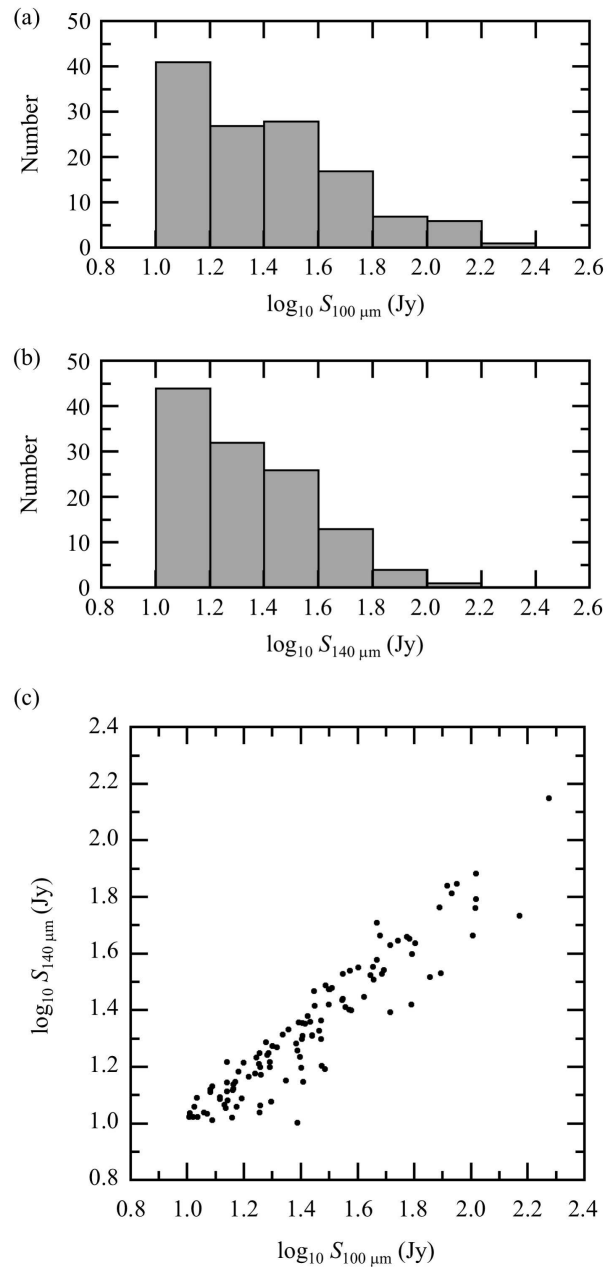


Fig. 4. FIR flux of the sample galaxies. (a) IRAS 100 μm . (b) AKARI 140 μm . (c) Correlation plot of both fluxes. The histograms include galaxies without other wavelength data.

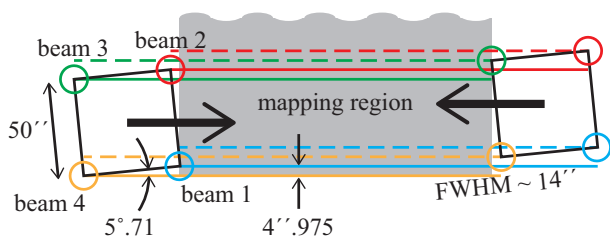


Fig. 5. OTF scanning pattern. FOREST with 50'' side was inclined 5°.71. The broad arrows indicate the scanning directions. The five-time round-trip scans with an offset of 4''.975 uniformly cover the mapped regions.

frequency resolution of 488 MHz.² Two correlators were assigned for each beam and polarization. The center frequencies were set to 115.271202 GHz for ^{12}CO ($J=1-0$) and 109.991763 GHz for ^{13}CO ($J=1-0$) and C^{18}O ($J=1-0$), respectively. We measured the image rejection ratio (IRR) of each side band of each beam every observation day. The typical system noise temperatures (T_{sys}) in each observation season were 560 K, 340 K, 360 K, and 390 K in ^{12}CO and 300 K, 170 K, 180 K, and 180 K in ^{13}CO and C^{18}O , respectively (table 2).

We observed the OTF-mapping mode to achieve a typical sensitivity of 30 mK in the antenna temperature (T_{A}^*) scale corresponding to ~ 70 mK in the main beam brightness temperature (T_{MB}) scale. Each region in a given target was mapped with more than one beam to reduce the influence caused by the difference in the performances of the four beams. Figure 5 shows that we rotated FOREST 5°.71 against the scan direction and raster scanned in 4''.975 separation, which was ~ 1.4 times higher than the Nyquist sampling of the 14'' beam to cover the mapped region with five round trips. This mapping method enabled us to minimize the peripheral regions with a high noise temperature. We adopted two orthogonal scan directions and made the noise temperatures of each direction as even as possible. Two points 10' offset from the map center were observed as the off-source positions. Although the off-source positions were kept far away from the Galactic disc, unfortunately, unknown Galactic molecular clouds may exist at the off-source points of UGCA 86 and NGC 1569 at the same receding velocity of the galaxies; thus, some profiles of these two galaxies were contaminated by “absorption” patterns.

We scanned each galaxy to cover 70% of D_{25} in diameter. Previous works (Nishiyama et al. 2001; Kuno et al. 2007) have shown that 70% of D_{25} of a galaxy covers the main region, where the CO emission is concentrated within a reasonable observation time. The scan directions were

along the galaxy major and minor axes to maximize efficiency, while those of the interacting systems were along the right ascension and declination covering the whole system. Observations were made referencing the equatorial coordinates, except for NGC 2268 and NGC 2276 with a declination of $> 80^\circ$. Both galaxies were observed in the galactic coordinates to avoid a large variation of the right ascension. The scan length along the minor axis of the galaxy was adopted by multiplying the length along the major axis by $\cos i$ listed in Tully (1988). The PA and i for setting an observing region were different from those listed in table 1, which we used for the data analysis (section 5), because we observed referring the PAs mainly listed in the Third Reference Catalogue of Bright Galaxies (RC3, de Vaucouleurs et al. 1991); however, it was convenient for the data analysis to refer to the kinematically derived PAs or use IR images. Table 3 lists the observation parameters.

Telescope pointing was checked roughly every hour by observing a bright source near the target galaxy, resulting in a pointing accuracy higher than 5''. We observed Galactic SiO maser sources in SiO ($v=1, J=1-0$) (rest frequency: 43.122090 GHz) and ($v=2, J=1-0$) (rest frequency: 42.820570 GHz). We observed quasars in continuum at 43 GHz when no strong SiO maser sources were found near the target. We did not use the data taken between these two pointing observations if the offset of the telescope pointing between the two pointing observations was larger than 5''. We also did not use the data taken under the bad condition of the radio seeing higher than 5'' – 8'', except for a few instances where the seeing monitors malfunctioned.

The intensity calibration was made with the chopper wheel method. The hot load was observed for every approximately 10 min. Corrections among the four beams of FOREST were made through the observations of the standard sources every observation day. The standard sources were the W 3 core [$(\alpha, \delta)_{\text{B1950.0}} = (2^{\text{h}}21^{\text{m}}53^{\text{s}}.2, +61^\circ 52' 21''.0)$] or IRC +10216 [$(\alpha, \delta)_{\text{B1950.0}} = (09^{\text{h}}45^{\text{m}}15^{\text{s}}.0, +13^\circ 30' 45''.0)$]. We also tried observing TMC-1 [$(\alpha, \delta)_{\text{B1950.0}} = (04^{\text{h}}38^{\text{m}}38^{\text{s}}.6, +25^\circ 35' 45''.0)$], but the emission was very weak; thus, we did not use it as a standard source. We mapped a region with a side of approximately 3' around the standard source with all four beams of FOREST. The intensities of the IRC +10216 and W 3 core showed a daily variation of $\sim 1-8\%$, which might be caused by the uncertainty of the IF attenuators. Subsection 4.1 presents the details on the calibration method.

² Some observations of a standard source IRC +10216 were made in 1 GHz bandwidth per IF band, but this does not affect the calibration results.

3.2 Observation ranking system

We introduced an observation ranking system in the last two observation seasons, which typically reduced the total observing time to complete a map by 37% compared to the first two seasons without this system. Selecting an optimum target from a sample of various right ascensions and declinations is a non-trivial exercise. Thus, we developed an observation system that ranked and selected the optimal target to minimize the : (1) observation time for each galaxy, (2) slewing time of the telescope, and (3) unusable data caused by pointing inaccuracy. We also put priority on finishing a galaxy instead of starting to map a new one, if possible, to promptly progress the data analysis.

We numerically express these factors as follows and compare the weights of the products of the factors, a priority index “ R ”:

$$R \equiv f_{\text{obs,eff}} f_{\text{slw}} f_{\text{point}} f_{\text{prop}} f_{\text{comp}}, \quad (1)$$

where $f_{\text{obs,eff}}$ is a factor representing the observation efficiency; f_{slw} represents the antenna slewing time; f_{point} denotes the pointing accuracy; f_{prop} expresses the scientific priority within our project team; and f_{comp} is the degree of completeness for a given target galaxy. A higher observation priority was given to the targets with a higher R value. Quantity R was immediately updated through a quick data reduction after each observation. Each factor and evaluation method were described in the subsections that follow, but note that this is somewhat a trial case for this system, and is, by no means, perfectly optimized. The goal was simply to select an optimal target under various observational conditions.

3.2.1 Factor of observation efficiency

Factor $f_{\text{obs,eff}}$ consists of two factors:

$$f_{\text{obs,eff}} \equiv f_{\text{atm}} f_{\text{map}}, \quad (2)$$

where f_{atm} represents an atmospheric factor, and f_{map} represents a mapping factor. We should observe a target with as low T_{sys} as possible, especially in an apparently large galaxy, to reduce the total survey time.

We formulated a f_{atm} weighted by T_{sys} because the observations at a lower T_{sys} [i.e., at a higher elevation (EL), figure 6a] saved our limited observing time. The factor had a higher weight when a target was observed at a higher EL . Scaling is presented as follows:

$$f_{\text{atm}} \equiv \frac{t_{\text{integ}}(EL_{\text{max}})}{t_{\text{integ}}(EL)} = \left[\frac{T_{\text{sys}}(EL_{\text{max}})}{T_{\text{sys}}(EL)} \right]^2, \quad (3)$$

where $t_{\text{integ}}(EL)$ is the necessary integration time for the observation at an elevation EL , and EL_{max} is the upper culmination EL or 80° , the latter being the EL limit for

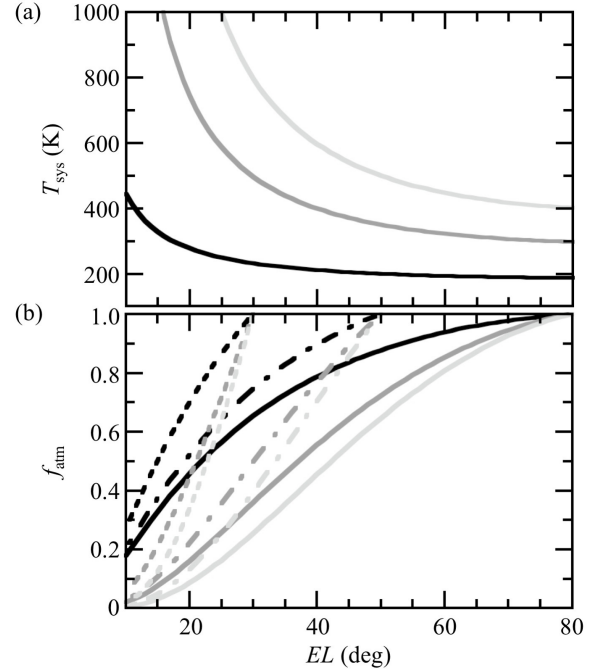


Fig. 6. (a) System noise temperature (T_{sys}) as a function of the elevation (EL). Lines for $T_{\text{sys}} = 200$ K (black), 350 K (dark gray), and 500 K (light gray) at $EL = 50^\circ$ are plotted. (b) Atmospheric factor (f_{atm}) as a function of the elevation. The colors are the same as (a). The lines for the elevation at the culmination of 80° (solid line), 50° (dash-dotted line), and 30° (dotted line) are plotted.

the telescope operation. $T_{\text{sys}}(EL)$ is T_{sys} at the EL of the target. $T_{\text{sys}}(EL)$ was calculated using the measured value before the observation and assuming that an optical depth only depends on the EL . That is, f_{atm} did not include effects caused by weather fluctuations. The f_{atm} factor was plotted in figure 6b for various conditions.

We defined f_{map} to observe apparently larger galaxies under a lower T_{sys} and smaller galaxies under a higher T_{sys} . We expressed this behavior as the relative integration time necessary for our survey sensitivity of $T_{\text{A}}^* = 30$ mK.

$$f_{\text{map}} \equiv 0.8 + \frac{t_{\text{integ}}(T_{\text{sys},260}) - t_{\text{integ}}(T_{\text{sys}})}{t_{\text{integ}}(T_{\text{sys},260})} \times \frac{t_{\text{dump}}}{t_{\text{pix}}} \times 5, \quad (4)$$

where $t_{\text{integ}}(T_{\text{sys},260})$ and $t_{\text{integ}}(T_{\text{sys}})$ are the necessary integration times under the condition of $T_{\text{sys}} = 260$ K of FOREST at 115 GHz, which is typical of good observing conditions, and T_{sys} at the present instant, respectively. t_{pix} is the integration time for 1 pixel per observing script for OTF mapping. t_{pix} decreased with the size of the target galaxies because the scan speed was different from one galaxy to another. The dump time of the backend t_{dump} was introduced for normalization. Factors 0.8 and 5 were adopted as constants such that all factors have a similar weight. Figure 7 shows the f_{map} behavior for a square-shaped observing map. In principle, efficiency has no max-

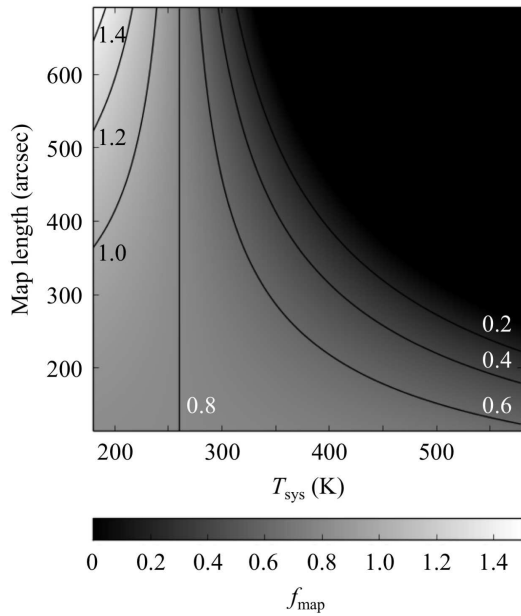


Fig. 7. Mapping factor (f_{map}) as a function of the system noise temperature and the map length. The target map is assumed to be square. Several contours are shown at the indicated levels spaced by 0.2.

imum value for very low T_{sys} ; however, such conditions are unlikely in practice.

3.2.2 Other factors

The speed of the telescope slew was $\sim 18^\circ \text{min}^{-1}$; therefore, we defined an antenna-tracking factor to provide a higher weight for the closer target to the present telescope direction:

$$f_{\text{slw}} \equiv 0.5 + \frac{1}{1 + |AZ_{\text{tel}} - AZ_{\text{obj}}|/90}, \quad (5)$$

where AZ_{tel} is the present azimuth of the telescope, and AZ_{obj} is the azimuth of the target object. Factor 0.5 was introduced such that f_{slw} became unity when the 45 m telescope caught up with a target in 5 min (i.e., the target was 90° away in azimuth).

Telescope pointing affects the usable data acquisition. The pointing factor f_{point} was affected by an angle between the telescope and the wind direction and the telescope elevation. A pointing source with a weak intensity needs longer integration time and iteration for accurate pointing. However, we simply set this factor to unity because no suitable relation was found between pointing and wind during the observational period.

We introduced factor f_{prop} for weighting by our scientific priority. f_{prop} is defined by the values of “default” priority in a decreasing order of: A, B, or C and the number of proposals by our project members containing the target, N , as:

$$f_{\text{prop}} \equiv R_{\text{priority}} + \frac{N}{20}. \quad (6)$$

Here, R_{priority} is a coefficient corresponding to the default priority, that is, 1.0 for priority A, 0.8 for B, and 0.0 for C.

The completeness of the observation is expressed as:

$$f_{\text{comp}} \equiv 1 + \frac{x}{1000}, \quad (7)$$

where x is the percentile of the observation completeness, and $f_{\text{comp}} = 0$ is set when the observations of a specific target have been completed. The factor took a value between 1.0 and 1.1 for the uncompleted targets.

4 Data reduction

Data reduction consisted of two parts: intensity scaling of the four beams of FOREST to a T_{MB} scale and data integration with baseline subtraction. We developed PYTHON scripts for the automatic data reduction: COMING Auto-Reduction Tools (COMING ART) for the latter step, which allowed the data reduction to be highly objective and reproducible.

4.1 Calibration

We corrected the relative intensity among the observational instruments using the integrated intensity of the standard sources taken with each beam and the polarization of FOREST. First, we made the integrated intensity maps in the ^{12}CO and ^{13}CO lines observed with each beam in 25×25 pixels in $7''.5$ spacing. The pixel spacing was different from the target maps of $6''$ (subsection 4.2), but this did not affect our calibration results because 1) the spacing was near the Nyquist rates, and we compared the relative intensities among the calibration data and 2) we searched for the peak position in each ^{12}CO map (figure 8a). We adopted the peak position of ^{12}CO with the same beam and polarization as the ^{13}CO peak because the ^{13}CO intensity was comparatively weak, making the definition of a precise peak position difficult. Some integrated intensity maps and the spectrum of the peak position appeared inconsistent when taken under poor pointing or seeing conditions. We did not use such data for the calibration.

One of the IF bands of beam 1, which seemed to be stable within each observation season, was adopted as the standard array. That is, the intensity scale taken with the other arrays was calibrated to the data taken with the standard array. Beam 1 was selected because it was on the optic axis of the telescope, and the beam efficiency was measured by the NRO.

Most of the integrated intensity maps of the calibra-

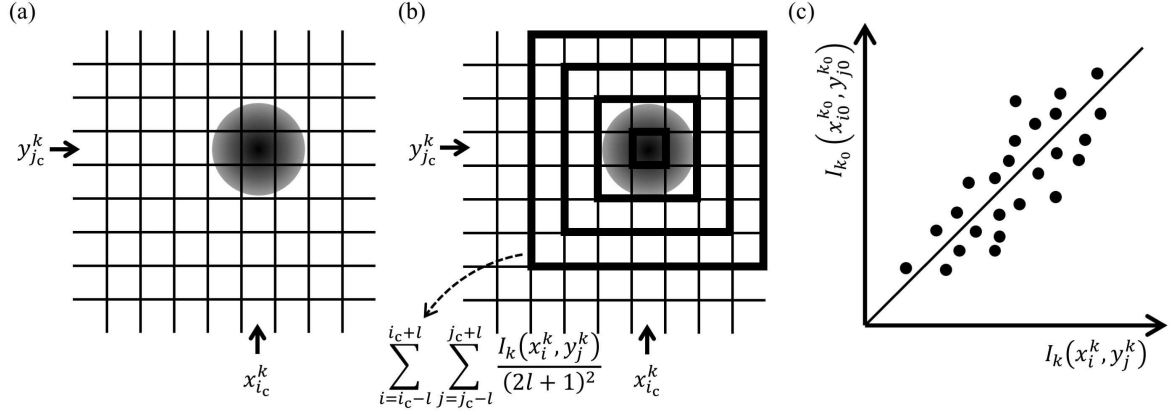


Fig. 8. Illustration of our calibration methods. (a) First, the pixel corresponding to the peak intensity is identified. (b) An average is then taken over $l \times l$ pixels ($l = 0, 1, 2, \dots$) around the peak pixel $(x_{i_c}^k, y_{j_c}^k)$. The averaged pixels are surrounded by the thick squares in the case of $l = 0, 1, 2, 3$. (c) Correlation among the $l \times l$ pixels around the peak position of the standard array and those of the other arrays was measured by the least squares fitting with a linear function.

tion source obtained during the period of 2018 March to April contained unexpected artifacts in a band of pixels because the reference frequency signal shifted during the OTF scans, resulting in parts of the observed data block being separated in frequency. One source object block was constructed by combining the separated data blocks, but this resulted in an erroneous band of pixels at the separation boundary. Thus, this contaminated region was masked and reconstructed using the information from the unaffected areas. The reconstruction was done using a modified version of the Papoulis-Gerchberg algorithm, which extrapolates the masked region by iterative Fourier transformations with certain assumptions. The reconstruction method was tested on the calibration images without issue, and a successful reconstruction was observed with an error of $\sim 1\%$. A detailed explanation about the obtained artifact, methodology, and reconstruction results for the affected images can be found in Cooray et al. (2019).

The precise calibration required measurements of the intrinsic intensity of the standard sources that was estimated by avoiding bad weather conditions as much as possible. The pointing errors induced by sudden wind or halation in an image because of bad seeing reduced the intensity calibration precision. Hence, we measured the peak intensity and the intensities averaged over 3×3 , 5×5 , 7×7 , 9×9 , and 11×11 pixels around the peak of the integrated intensity map, and compared them with the corresponding data taken with the standard array.

We measured the temporal scaling factors in the two following ways: The first is defined as:

$$f_{1,l}^k = \frac{\sum_{i_0=i_{c0}-l}^{i_{c0}+l} \sum_{j_0=j_{c0}-l}^{j_{c0}+l} I_{k_0}(x_{i_0}^{k_0}, y_{j_0}^{k_0})}{\sum_{i=i_c-l}^{i_c+l} \sum_{j=j_c-l}^{j_c+l} I_k(x_i^k, y_j^k)}$$

$$(l = 0, 1, 2, 3, 4, 5). \quad (8)$$

Here, $l = 0, 1, 2, \dots$ correspond to using only the peak, 3×3 pixels around the peak, 5×5 pixels around the peak, and so on (figure 8b). We described each pixel in a 25×25 pixels map taken with the array “ k ” as (x_i^k, y_j^k) ($i, j = 1, 2, 3, \dots, 25; k = 1, 2, 3, \dots, 16$) and the found peak position as $(x_{i_c}^k, y_{j_c}^k)$. Subscript “0” represents the standard array value. $I_k(x_i^k, y_j^k)$ is the integrated intensity at the pixel (x_i^k, y_j^k) of the array “ k ” and k_0 represents the standard array. The other is defined as a gradient of the least squares fitting of the linear function (figure 8c):

$$\begin{aligned} I_{k_0}(x_{i_0}^{k_0}, y_{j_0}^{k_0}) &= f_{2,l}^k I_k(x_i^k, y_j^k) \\ (i_0 &= i_{c0} - l, i_{c0} - l + 1, \dots, i_{c0} + l; \\ j_0 &= j_{c0} - l, j_{c0} - l + 1, \dots, j_{c0} + l; \\ i &= i_c - l, i_c - l + 1, \dots, i_c + l; \\ j &= j_c - l, j_c - l + 1, \dots, j_c + l; \\ l &= 1, 2, 3, 4, 5). \end{aligned} \quad (9)$$

We compared these temporally scaling factors, $f_{1,l}^k$ ($l = 0, 1, 2, 3, 4, 5$), $f_{2,l}^k$ ($l = 1, 2, 3, 4, 5$), and found that the average of 11×11 pixels around the peak ($f_{1,5}^k$) seemed to be the most stable. However, the intensity showed a noticeable scatter between the observational days even when using 11×11 pixels. Thus, we did not calibrate the data daily, but calibrated them using the averaged scaling factor over some observational periods (3 – 83 days, typically ~ 20 days) divided by the maintenance of FOREST or the local oscillators that possibly affected the intensity scaling.

The data taken with the standard arrays were multiplied by the IRR correction factors as follows:

$$f_{\text{IRR}} = 1 + 10^{-\frac{\text{IRR}}{10}} \quad (10)$$

where IRR is the image rejection ratio in dB measured at the beginning of every observation day (subsection 3.1). After this step, the intensity scale of the standard array became the T_A^* scale. This correction was not done for the data taken with the other arrays because we directly scaled the intensity taken with those arrays with the intensity of the standard array in the T_A^* scale.

The data of the standard sources taken in the second observation season were divided by the main beam efficiency (η_{MB}) of the 45 m telescope, while those taken in the other seasons were scaled to be the same intensity as the former data. The main beam efficiencies of the telescope of $\eta_{MB}(115\text{GHz}) = 45 \pm 2\%$ and $\eta_{MB}(110\text{GHz}) = 43 \pm 2\%$ provided by the NRO³ were used to convert the data taken in the second observation season into the T_{MB} scale. Only $\eta_{MB}(115\text{GHz}) = 39 \pm 3\%$ was public⁴ in the first observation season, and η_{MB} was not measured in the third observation season because of an unforeseen telescope impairment. We also did not use $\eta_{MB}(115\text{GHz}) = 43 \pm 4\%$ and $\eta_{MB}(110\text{GHz}) = 44 \pm 4\%$ in the fourth observation season⁵ because the intensity of the standard objects was inconsistent with the previous values when we used these efficiencies. Therefore, we did not divide the data taken in the three seasons, except for the second observation season by η_{MB} . However, we used the scaling factors that corresponded to the intensity of the standard sources to those taken in the second observation season.

4.2 Auto-reduction scripts, COMING ART

We developed and used the data reduction scripts COMING ART based on the Nobeyama OTF Software Tools for Analysis and Reduction (NOSTAR) developed by the NRO. These scripts were composed of several steps, including the evaluation of the baseline undulation, flagging of bad data, basket weaving, and automatic baseline subtraction. Figure 9 shows an overview of the procedures in the pipeline. We could reduce data with very high objectivity and reproducibility using the COMING ART. Each step in figure 9 is explained below.

4.2.1 Step 1: data formation and intensity scaling

CO maps were generated as a data cube with $6''$ spacing and a velocity width of 10km s^{-1} . We selected a correlator dump time of SAM45 of 0.1s according to Sawada et al. (2008), which resulted in an OTF scan speed of approximately $4''$ to $39''$ per second depending on the map size. The data were split with a task **Split** in the NOSTAR and

calibrated with a task **Scaling** in the NOSTAR using the scaling factors described in subsection 4.1. We produced data cubes in the abovementioned intervals according to Sawada et al. (2008). The effective spatial resolution of the OTF maps was $17''$ in both 115 GHz and 110 GHz, which was larger than the size of the observation beam of $14''$. The data cubes were then subject to the reduction steps described below.

4.2.2 Step 2: baseline subtraction

A linear baseline was fitted for the two velocity ranges with 350km s^{-1} width on both sides of the emission range using the task **Baseline** in the NOSTAR. The velocity range of emission was based on the previous ^{12}CO or H I data rounded to a multiple of 10km s^{-1} . The two baseline ranges were immediately set adjacent to the emission range.

4.2.3 Step 3: discarding heavily undulated spectra (“auto-flag”)

This step begins with evaluating the rms noise of an ideal non-undulated spectrum using a fast Fourier transform (FFT) analysis and removing lower-frequency components. The baseline undulation over a wide frequency range was non-trivial because distinguishing it from the wide and weak emission line of a galaxy was very difficult. Even a loose undulation increased the rms noise and prevented the evaluation of the degree of undulation; thus, we performed an FFT analysis and calculated the rms noise of the spectrum whose frequency components lower than 7.3 MHz were removed, $\sigma_{\text{non-smoothed,FFT}}$. The 7.3 MHz frequency was empirically adopted from the analysis of the observed data of several galaxies. Figures 10a and b show examples of the undulated spectra. Figures 10c and d depict the Fourier transforms of these undulated spectra. We obtained undulation-corrected spectra (figures 10e and f) when we masked the frequency components lower than 7.3 MHz shown in the gray hatch in these panels.

Second, we flagged and removed the poor-quality data after checking the rms noise behavior considering a *salvage factor*. When a spectrum is smoothed by summing up the channels, the rms noise should inversely decrease proportional to a square root of the number of the summed-up channels if the spectrum no longer suffers from undulation. Almost all the spectra will be identified as poor-quality data if we strictly apply this criterion; thus, we introduced a salvage factor f_{salvage} , which was larger than unity and lower than ~ 4 , in the case of

$$\frac{\sigma_{\text{non-smoothed,FFT}}}{\sqrt{n}} \times f_{\text{salvage}} < \sigma_{n\text{-smoothed}}, \quad (11)$$

where $\sigma_{n\text{-smoothed}}$ is the rms noise for the n -channel

³ (<https://www.nro.nao.ac.jp/~nro45mrt/html/prop/eff/eff2015.html>).

⁴ (<https://www.nro.nao.ac.jp/~nro45mrt/html/prop/eff/eff2014.html>).

⁵ (https://www.nro.nao.ac.jp/~nro45mrt/html/prop/eff/eff_latest.html).

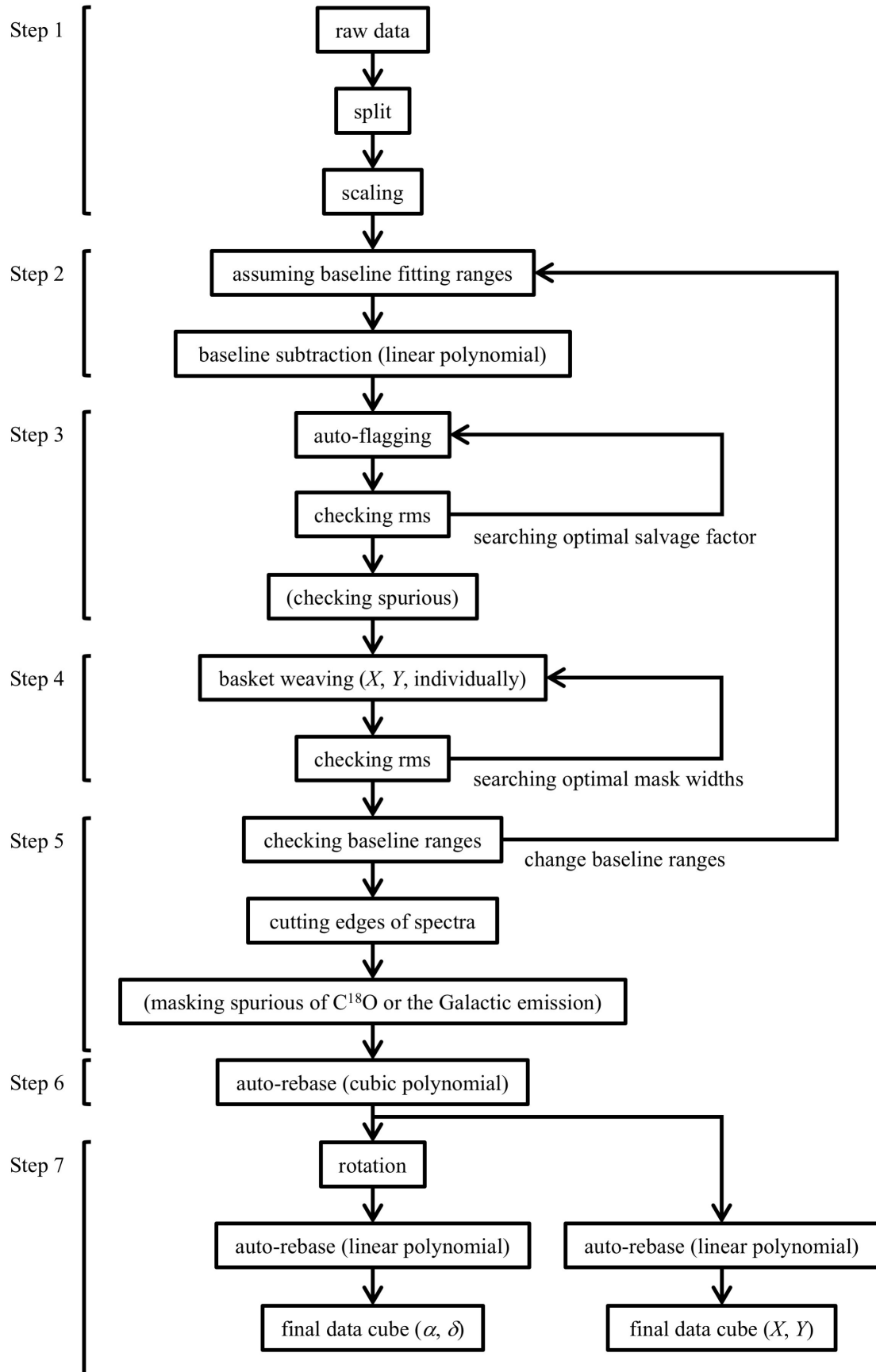


Fig. 9. Concept of data reduction scripts, COMING ART.

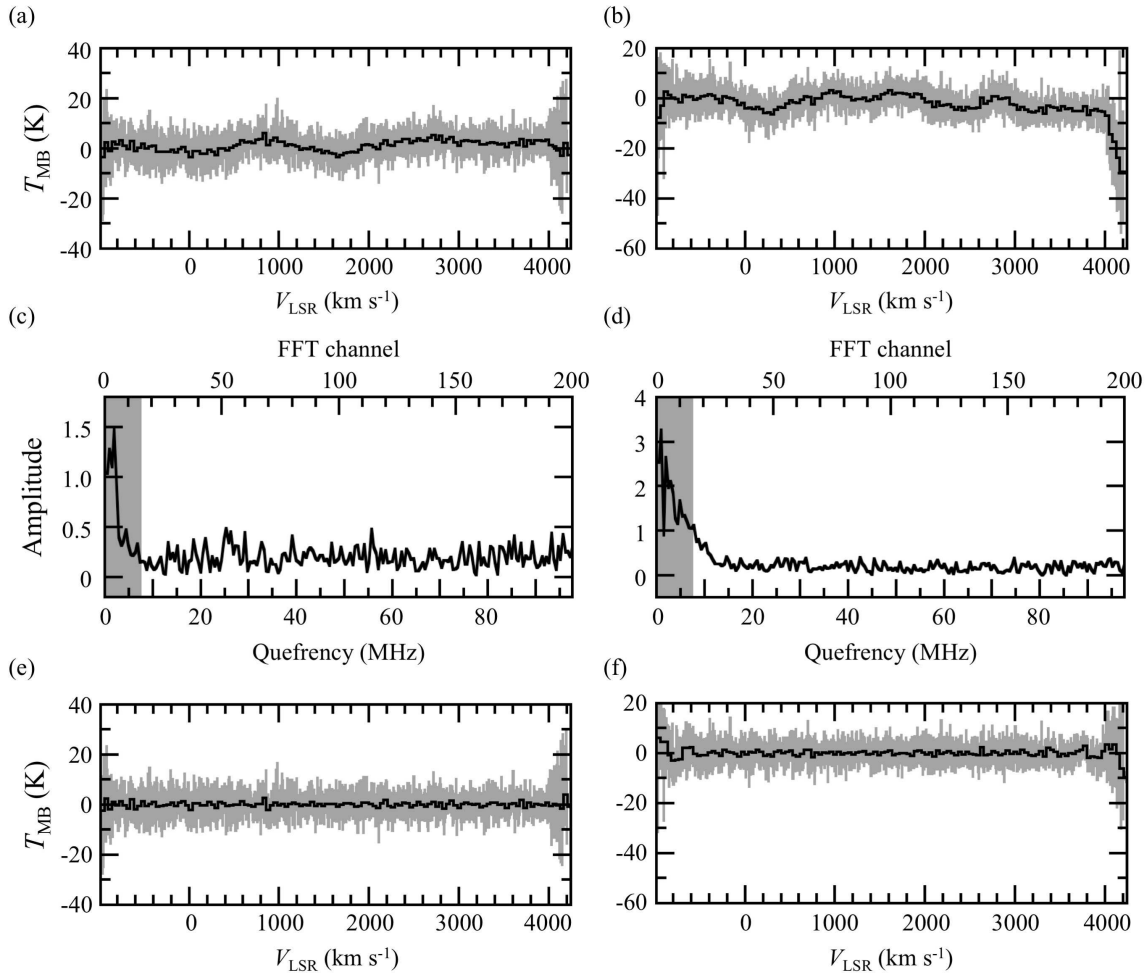


Fig. 10. Examples of the undulating spectra of NGC 337. (a), (b) Gray lines are original spectra and black lines are 32-ch smoothed spectra. (c), (d) The Fourier transforms of (a) and (b), respectively. Data below 200 channels are plotted. Gray hatched regions indicate below 15 FFT channels, which corresponds to 7.3 MHz in quefrequency. (e), (f) Spectra masked lower than 7.3 MHz in quefrequency of (a) and (b), respectively. Gray lines are masked spectra and black lines are 32-ch smoothed spectra.

smoothed spectrum. We will then discard that specific spectrum. We smoothed a spectrum of 4096 channels for every 32 channels and evaluated the baseline undulation by comparing the rms of the smoothed spectrum with that of the non-smoothed one. In this process, the rms was calculated for all channels, including the channels containing the CO emission, except for the NGC 3034. The emission of NGC 3034 was particularly strong; therefore, the rms was calculated for the channels over the default baseline ranges. The resultant rms noise had a local minimum or monotonously decreased with the increasing f_{salvage} (figure 11) because removing the spectra with the undulated baselines resulted in a lower rms noise at first, but decreasing the number of spectra in the integration then increased the noise levels. We fixed n as 32 and assigned 1.4 to 4.0 in steps of 0.2 for f_{salvage} . We then searched for the min-

imum value of the resultant rms noise, and adopted the salvage factor when the resultant rms was minimum. This flagging method was called **auto-flag**. After flagging the poor-quality data, the resulting data cube was constructed with a task **Make Map** in the NOSTAR.

4.2.4 Step 4: basket weaving

Basket weaving is an effective method of decreasing the impact of the scanning effect for scan observations (Emerson & Gräve 1988). The width is masked for a Fourier transformed map to reduce the scanning noise seen in the original map. Although the same mask width is adopted for the X- and Y-directions in a task **Basket-Weave** in the NOSTAR, the procedure is not necessarily effective for a map with a large aspect ratio, such as an edge-on galaxy. Basket weaving was performed herein by independently as-

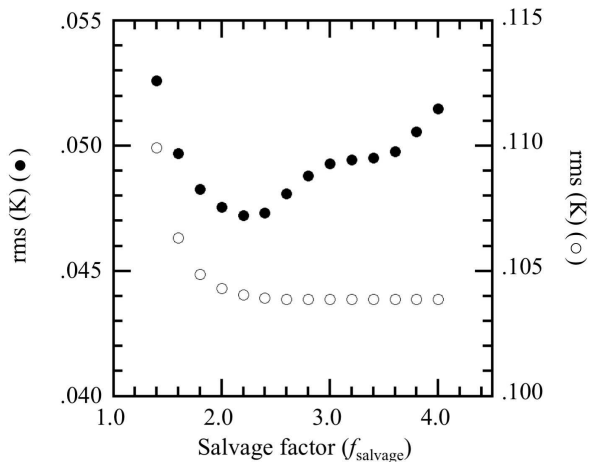


Fig. 11. Behavior of the rms with the salvage factor (f_{salvage}). The filled circles show an example of a case with a local minimum (NGC 660), while the open circles depicts a case with a declining rms (NGC 628).

signing a mask width along the major (X -direction) and minor (Y -direction) axes of a given map, then adopting mask widths to minimize the resultant rms noise.

4.2.5 Step 5: checking the baseline ranges and flagging of spurious channels

For the data whose signal range overflowed into the initial baseline range, the baseline range was revised, and the abovementioned procedures were iterated (figure 9); otherwise, the data were fine-tuned. Checking was made by the eye for a profile map and a spatially integrated total spectrum in ^{12}CO of each galaxy. After the *signal range* confirmation, we adopted the final *baseline ranges*, which were both sides of the signal range with a width of 200 km s^{-1} . We then cut both outsides of the baseline range. We masked the channels to zero intensity when spiky spurious features were seen in the spectra. This procedure was applied to some data of C^{18}O . The channels smeared by the Galactic emission in NGC 1569 and UGCA 86 were also masked.

4.2.6 Step 6: baseline subtraction with a cubic polynomial (“auto-rebase”)

We fitted the baseline again to optimize the zero level in each spectrum. We then applied a cubic polynomial as a baseline. We evaluated the possibility that a cubic polynomial fitting for the baseline extinguishes or reduces the galaxy emission. We calculated the rms noises in the *baseline ranges* and the *emission range* of a model Gaussian profile emission with sinusoidal undulation and various signal-to-noise (S/N) ratios. This simple evaluation indicated that the cubic polynomial fitting more effectively

reduces the rms noise compared to a linear fitting without deleting the real emission.

We determined the emission ranges in the following manner: identifying which part of the spectrum indicates emission, in the case the velocity field of a galaxy is unknown, is not necessarily trivial. We created a data cube smoothed by 3×3 pixels in space. Within this smoothed cube, we identified the channels with $S/N > 2.5$ and designated them as the *emission channels*. All remaining channels, including the 200 km s^{-1} range outside of the signal range, were identified as the *baseline channels* used to fit a final baseline. This technique is called **auto-rebase**. The emission for the three CO lines was searched for in this manner, but the searching emission range of ^{13}CO and C^{18}O was restricted to the emission channels of ^{12}CO because both lines were weak in comparison.

4.2.7 Step 7: coordinate transformation and “auto-rebase”

The data cube was rotated to align with the equatorial coordinates. We performed **auto-rebase** with a linear baseline subtraction again for the original and rotated data. The spatial resolution of a map along the X - and Y -directions was slightly higher than that of a map in the equatorial coordinates because the pixel interval of the equatorial map was coarser. Thus, we prepared both cubes, although we used the equatorial coordinate cubes for the subsequent analysis. The process after scaling was automated as a single PYTHON script.

We calculated the rms noise for each pixel over the whole baseline channels and made an rms noise map. The average of the rms noise map was recorded as the typical rms noise in the header of the resulting FITS data cube. We also made FITS cubes where the baseline channels were represented as unity, and the emission channels were represented as zero. The final data cubes are available at the Japanese Virtual Observatory (JVO) website⁶.

5 Data analysis

5.1 CO

The integrated intensity maps were constructed by summing up the emission channels for each pixel

$$\begin{aligned}
 I(\alpha, \delta) &= \int T_{\text{MB}}(\alpha, \delta, v) dv \\
 &= \sum_{k \in \text{Emission channels}} T_{\text{MB}}(\alpha, \delta, k) \Delta v_{\text{ch}}, \quad (12)
 \end{aligned}$$

for each line of ^{12}CO , ^{13}CO , or C^{18}O , where k is the channel number, and Δv_{ch} is the velocity width of a channel

⁶ (<https://jvo.nao.ac.jp/portal/nobeyama/coming.do>).

(10 km s^{-1}). The error of the integrated intensity was calculated as:

$$\sigma_{\text{integ}} = \sigma_{\text{rms}} \times \sqrt{\Delta V_{\text{signal}} \times \Delta v_{\text{ch}}}, \quad (13)$$

where σ_{rms} is the rms noise calculated over the baseline channels, and ΔV_{signal} is the total velocity width of the emission channels. Note that ΔV_{signal} became zero for the emission-free pixels when we applied the **auto-rebase** to the data; thus, σ_{integ} was also zero following equation (13). This clearly underestimated the error of the integrated intensity of each pixel; therefore, we calculated the average width of the emission channels for the pixels with more than one emission channel and adopted this average as a typical emission width and applied it to equation (13) for the emission-free pixels. In the case of C^{18}O , even this typical emission width became zero because the emission was hardly detected. We applied a typical line width of ^{13}CO instead of that of C^{18}O in this case.

The total molecular gas mass of a galaxy M_{mol} was calculated by summing up the pixels within an infrared-defined radius described in subsection 5.2 and applying the standard conversion factor (Bolatto et al. 2013):

$$X_{12\text{CO}} \equiv \frac{\mathcal{N}(\text{H}_2)}{I_{12\text{CO}}} = 2 \times 10^{20} [\text{cm}^{-2} (\text{K km s}^{-1})^{-1}]. \quad (14)$$

This conversion factor had an error of 30% (Bolatto et al. 2013), but we did not include this error in our error analysis. We also did not consider the calibration uncertainty of < 10% when summing up the calibration fluctuation described in subsection 3.1 and the fluctuation in η_{MB} described in subsection 4.1. Thus, M_{mol} may have an uncertainty of $\sim 30\%$, which is not explicitly included. We further multiplied by a factor of 1.36 to include the contributions from He.

The first- and second-degree moment maps were made using the CASA routine **immoments**. The first-degree moment

$$\frac{\int v T_{\text{MB}}(\alpha, \delta, v) dv}{\int T_{\text{MB}}(\alpha, \delta, v) dv} \equiv \bar{v} \quad (15)$$

provides an intensity-weighted mean velocity, while the second-degree moment

$$\sqrt{\frac{\int (v - \bar{v})^2 T_{\text{MB}}(\alpha, \delta, v) dv}{\int T_{\text{MB}}(\alpha, \delta, v) dv}} \equiv \Delta v \quad (16)$$

provides the velocity dispersion. We smoothed and masked the data following the method outlined in Miyamoto et al. (2018) to avoid the invalid moment values caused by noise. First, the data were convolved with 1.5 times of the beam size, and then the intensity-weighted moments and the rms noise were calculated for the spatially smoothed cubes. Second, the pixels whose S/N of the integrated intensity was lower than 4 were masked using these smoothed data.

5.2 WISE $3.4 \mu\text{m}$

We analyzed the archival $3.4 \mu\text{m}$ band data of the WISE (Wright et al. 2010) All-Sky Survey to measure the stellar mass of our sample galaxies. According to Wen et al. (2013), a $3.4 \mu\text{m}$ luminosity provides a reasonable index of the stellar mass of galaxies. We downloaded the data corresponding to the coordinates of the galactic center listed in table 3 from the NASA/IPAC Infrared Science Archive⁷. The downloaded images covered more than two times of D_{25} . A pixel scale of the images was $1.''375$. The background level was estimated from a histogram of the pixel values within a ring between radii $2 \times R_{25}$ and $3 \times R_{25}$ ($R_{25} \equiv D_{25}/2$) and subtracted following the documents from the WISE project⁸. Panel (a) of figures 12, 13 and supplementary figures 1 – 134 in the supplementary section of the online version depict the background-subtracted images.

Many Galactic stars were imaged in the WISE $3.4 \mu\text{m}$ images; hence, we roughly masked these stars to measure a more precise stellar mass. We identified the Galactic stars by simply assuming that they corresponded to bright, point-like sources. Although the typical resolution of the Atlas image of $3.4 \mu\text{m}$ is $\approx 8.''3$, we fitted a Gaussian with a 1.3 times larger FWHM than the resolution to capture the extended halo around the brightest Galactic stars. We checked all the images in the logarithmic intensity scale and confirmed that the Galactic stars were removed. Some images showed strong spider diffraction patterns caused by very bright stars. These images were identified and automatically masked. The pixels on the stars and the spider diffraction patterns were substituted with an average value around the stars or the spider diffraction patterns.

This rough identification caused some misidentification of the Galactic stars, especially for the galaxies just behind the Galactic plane or galaxies with bright foreground stars. We could not mask a foreground Galactic cluster in UGCA 86. Many foreground stars resulted in a large uncertainty in the infrared flux in IC 10 and IC 356. One or two bright stars with spider diffraction patterns also resulted in an uncertainty in NGC 1569 and NGC 2276. In the case of NGC 5792, a bright star could not be completely subtracted, and the galaxy emission was overestimated. We did not use the stellar mass and its related values for UGCA 86 because our measured stellar mass had large associated uncertainties. In the case of NGC 1055, NGC 3338, NGC 3627, NGC 5055, and NGC 6951, a foreground bright star likely contributes to additional uncertainty. In NGC 5364 and NGC 5907, two foreground stars

⁷ (<http://irsa.ipac.caltech.edu/Missions/wise.html>).

⁸ (http://wise2.ipac.caltech.edu/docs/release/allsky/expsup/sec1_4c.html).

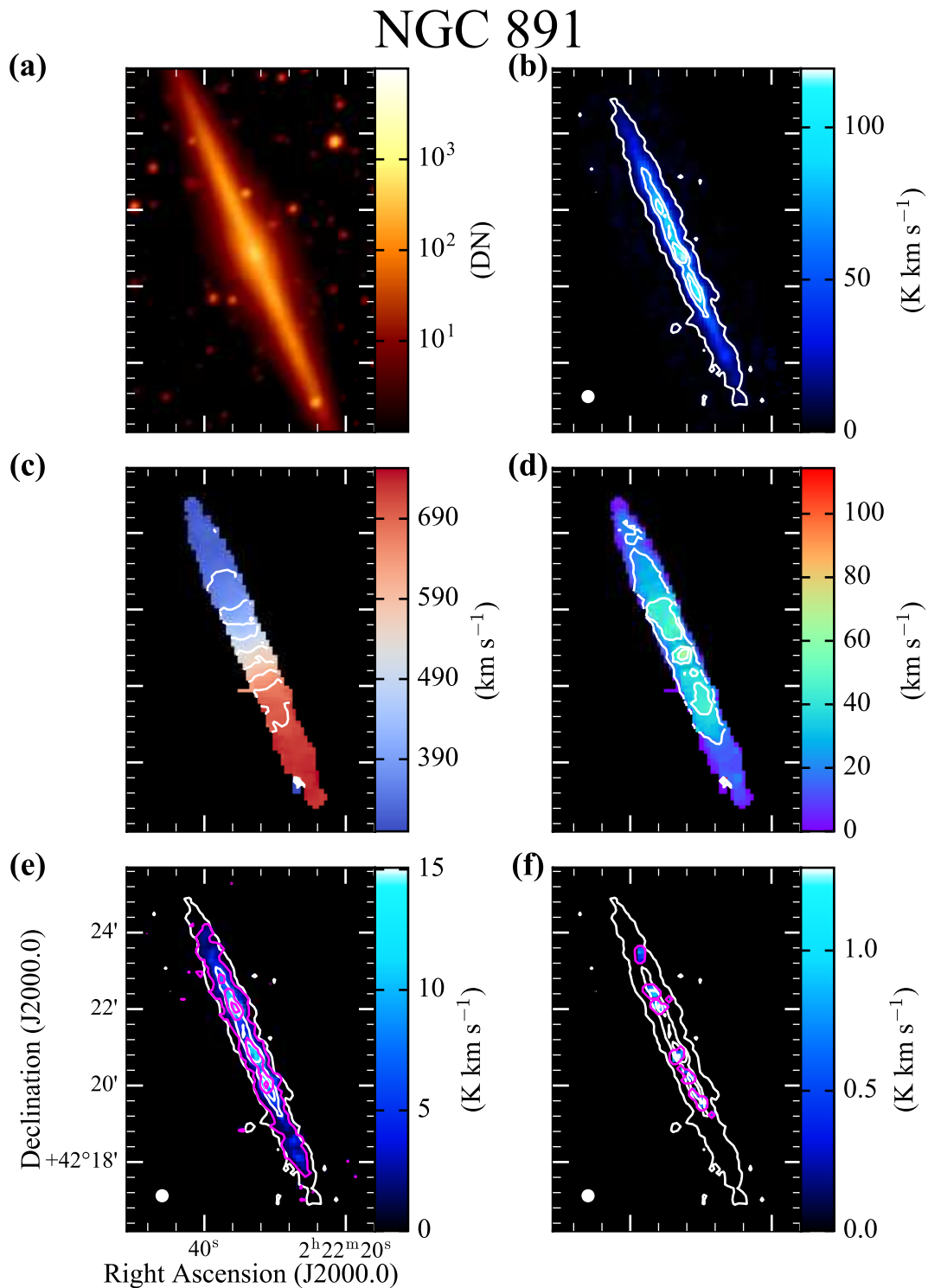


Fig. 12. NGC 891. (a) Background-subtracted WISE $3.4\ \mu\text{m}$ image. (b) Integrated intensity of ^{12}CO ($J = 1 - 0$). The contours are plotted at 5%, 40%, and 60% of the maximum intensity of $152.45\ \text{K km s}^{-1}$. (c) First-degree moment map of ^{12}CO . The contours are in $45\ \text{km s}^{-1}$ steps. (d) Second-degree moment map of ^{12}CO with the contours in steps of $20\ \text{km s}^{-1}$. (e) Integrated intensity of ^{13}CO ($J = 1 - 0$). The white contours are the same as the panel (b). The magenta contours are plotted at 5%, 45% and 85% of the maximum intensity of $16.53\ \text{K km s}^{-1}$ in ^{13}CO . (f) Integrated intensity of C^{18}O ($J = 1 - 0$). White contours are the same as the panel (b). The magenta contours are plotted at 5% of the maximum intensity of $2.26\ \text{K km s}^{-1}$ in C^{18}O . The OTF beam size is indicated as a white filled circle in the bottom-left corner in panel (b), (e), and (f).

NGC 3627

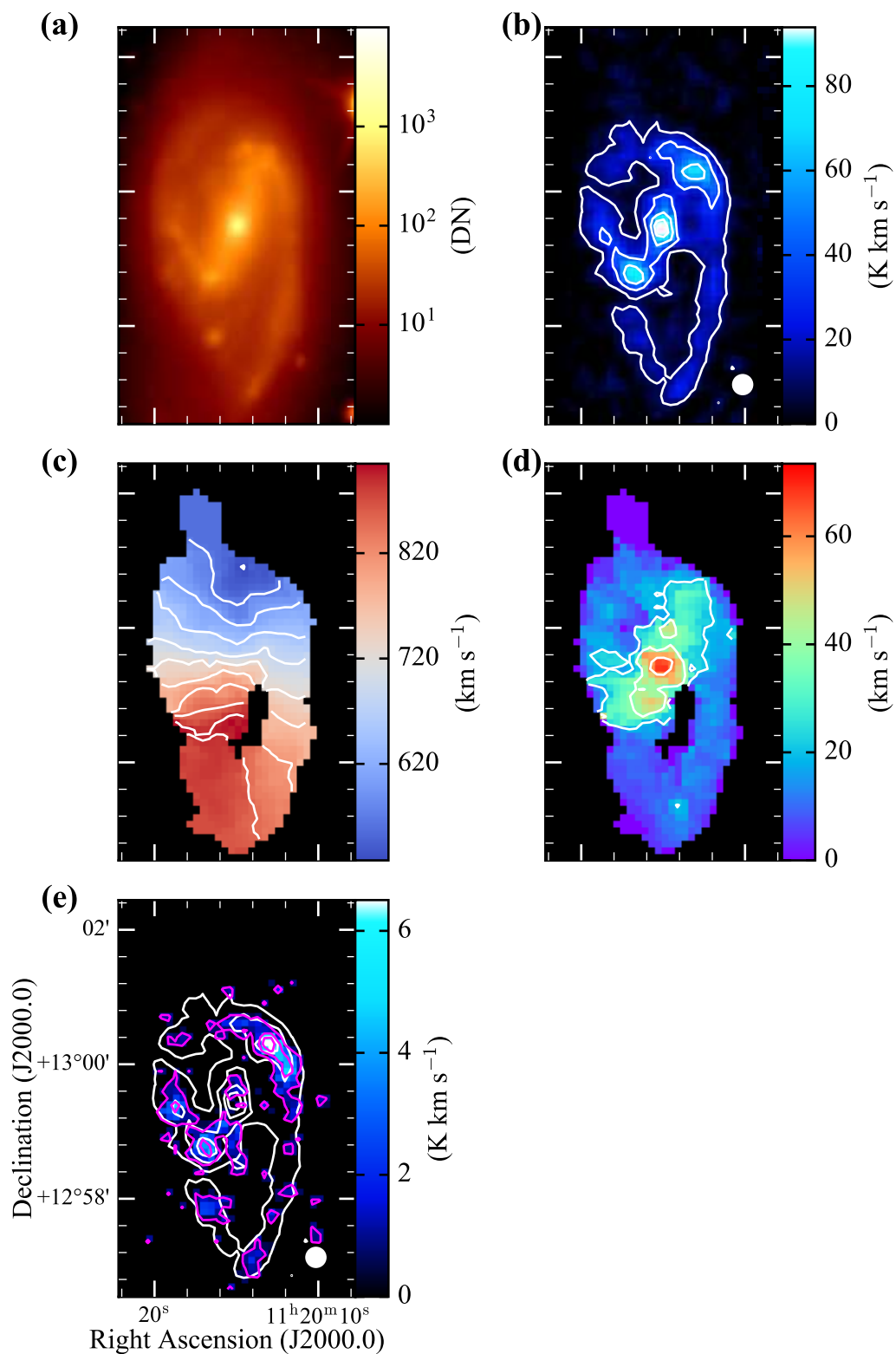


Fig. 13. Same as figure 12, but for NGC 3627. The contours are plotted at 10%, 30%, 55%, and 80% of the maximum intensity of 109.87 K km s⁻¹ in (b) and (e) (*white*), in steps of 40 km s⁻¹ in (c), in steps of 20 km s⁻¹ in (d), and at 10%, 45%, and 80% of the maximum intensity of 7.88 K km s⁻¹ in (e) (*magenta*).

could not be removed because of their positions coincident with the target galactic discs. However, the data contamination for these seven galaxies seems only minor within an error bar and remains as such in our sample for further analysis. Our star masking, except for the six galaxies (i.e., IC 10, UGCA 86, IC 356, NGC 1569, NGC 2276, and NGC 5792) with a large uncertainty, affects the derived total stellar mass of approximately 10% at most, as obtained from the comparison of the star-masked and non-masked data.

We measured the typical radial extent of $3.4\mu\text{m}$ images and adopted it as a galaxy radius (hereafter $R_{3.4\mu\text{m}}$). We then constructed a radial distribution from the star-masked images using the galaxy parameters listed in table 1 and interpolated in $1''$ spacing. The $R_{3.4\mu\text{m}}$ radius is defined as the radius where the radially averaged intensity becomes smaller than the dispersion (1σ) of the background pixels. This radius typically corresponds to a bending point of the radial profiles. The stellar distributions for the interacting galaxies were divided into each galaxy using the local minima near the line linking both galaxy centers. Individual radial profiles were then calculated. Our samples contained “no” clear overlapping regions in the interacting systems, which would, otherwise, complicate this approach. We make special note of NGC 660, where the extended optical emission indicates a $\text{PA} = 170^\circ$ and $i = 67.7^\circ$, which was quite different from the values adopted in table 1, although we adopted the former for putting a high priority on outer disc. The radial distribution of the four edge-on galaxies, namely NGC 891, NGC 3628, NGC 4302, and NGC 5907, which have inclinations higher than 85° were made only using the data on the major axis.

$R_{3.4\mu\text{m}}$ is typically more than 30% larger than R_{25} . We compared both radii in figure 14a. Although most galaxies had a larger $R_{3.4\mu\text{m}}$ than R_{25} , a few galaxies had smaller $R_{3.4\mu\text{m}}$ than R_{25} (e.g., NGC 628). We also compared $R_{3.4\mu\text{m}}$ and the semi-major axis reported in the Spitzer Survey of Stellar Structure in Galaxies (S^4G , Sheth et al. 2010) for the 115 galaxies⁹ common between that and COMING (figure 14b).

The total stellar mass of a galaxy was calculated from the star-masked images using the formula from Wen et al. (2013). The star-masked images were converted into luminosity scale using the adopted distance listed in table 1 within a projected ellipse, where $R_{3.4\mu\text{m}}$ was calculated. The total luminosity of a galaxy was converted into the total stellar mass according to the following equation (Wen et al. 2013):

⁹ The number of common samples between our survey and S^4G is 116, but the semi-major axis of NGC 4647 is not listed.

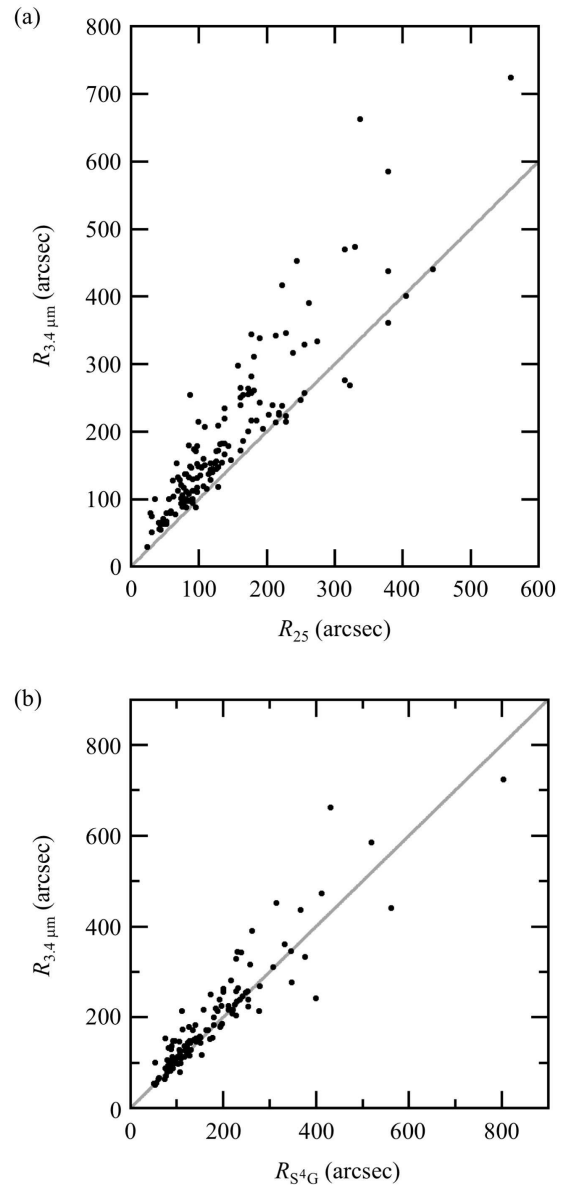


Fig. 14. Relation between the radius derived from WISE $3.4\mu\text{m}$ data in this work ($R_{3.4\mu\text{m}}$) and the optical radius ($R_{25} = D_{25}/2$). The solid line indicates $R_{3.4\mu\text{m}} = R_{25}$. (b) Same as (a), but comparing with the semi-major axis in S^4G (Sheth et al. 2010).

$$\log_{10} \left(\frac{M_*}{M_\odot} \right) = (0.679 \pm 0.002) + (1.033 \pm 0.001) \times \log_{10} \left(\frac{\nu L_\nu(3.4 \mu\text{m})}{L_\odot} \right). \quad (17)$$

We did not consider herein the contribution from the active galactic nucleus (AGN) to the $3.4 \mu\text{m}$ luminosity. Some interacting galaxies overlapped each other, and our image separation process resulted in a comparatively poorer flux accuracy in these systems. The stellar mass of NGC 660 was calculated within the ellipse projected using $\text{PA} = 170^\circ$ and $i = 67.7^\circ$ (i.e., determined from CO). The stellar mass of the four edge-on galaxies was calculated within a rectangular region with the major axis length corresponding to $2R_{3.4 \mu\text{m}}$. The pixel values along the lines parallel to the major axis were averaged. Its distribution in the direction perpendicular to the major axis was then used in the same way as measuring $R_{3.4 \mu\text{m}}$. The shorter axis was adopted to be twice this value.

We compared our derived stellar masses with those measured in S^4G (Sheth et al. 2010; Muñoz-Mateos et al. 2013; Querejeta et al. 2015) after substituting their adopted galaxy distance for our adopted value (figure 15). The comparison was done for 115 galaxies common to both samples. The errors were comparable to or smaller than the size of each marker, and we did not consider these errors because of the adopted models (i.e., only the contribution from the flux errors). The stellar mass derived in this work was typically approximately 20% lower than that in the previous work, although the measured sizes were not necessarily common (figure 14b). This offset is mainly explained by our conservative star masking method which masks slightly larger area than the extent of stars and background subtraction. The offset cannot be explained by difference of the assumed IMFs, as it has a contrary effect (Zahid et al. 2012): Kroupa IMF (Kroupa 2001) for Wen et al. (2013) and Chabrier IMF (Chabrier 2003) for S^4G (Querejeta et al. 2015). In addition, a minor offset was found between the WISE $3.4 \mu\text{m}$ band and the Spitzer $3.6 \mu\text{m}$ band at a higher magnitude (Wen et al. 2013). Table 4 lists the total stellar masses and $R_{3.4 \mu\text{m}}$.

6 Results and discussion

6.1 Spectra, integrated intensity maps, and moment maps

Figure 16 presents a selection of ^{12}CO spectra with various velocity widths and also depicts the spectra of ^{13}CO and C^{18}O at the same position in the same galaxy. The ^{13}CO emission was typically several to 10 times weaker than the ^{12}CO emission; thus, the S/N ratio of the ^{13}CO spectra

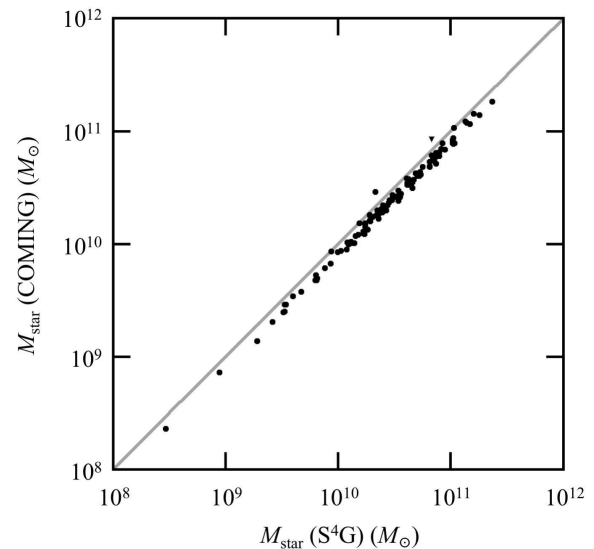


Fig. 15. Stellar masses derived in this work and S^4G (Sheth et al. 2010). The solid line indicates that both masses are equal. The errors are comparable to or smaller than the size of each marker. The triangle indicates the upper limit of the stellar mass estimated in this work.

was low despite the lower T_{sys} values of ^{13}CO compared to that of ^{12}CO . The C^{18}O emission was much weaker than the ^{12}CO emission. For example, the peak intensity of a C^{18}O spectrum of NGC 891 in figure 16 was $\sim 2.9\sigma$, which was only a marginal detection. Only 14 positions in 11 galaxies showed the integrated intensity of C^{18}O exceeding $\sim 4\sigma$ and ^{12}CO exceeding $\sim 3\sigma$. However, comparing these spectra with the ^{12}CO spectra at the same positions, two of the spectra appeared to be merely noise, while four cannot be clearly considered as detection.

Panel (b) of figures 12 and 13 and supplementary figures 1 – 134 (supplementary section of the online version) show the integrated intensity maps of ^{12}CO . The S/N ratio (or noise level) was not uniform within an integrated intensity map because of the different velocity widths of the emission channels. Thus, we drew contours at some percentiles of the maximum intensity in each map. We set the lowest contour levels to match the emission extent of the first-degree moment maps by eye because the first-degree moment maps were produced by smoothing and masking, and were likely to trace the real emission extent. Some galaxies showed a molecular gas distribution similar to the stellar distribution tracing spiral arms and/or a bar, while some showed quite different patterns (e.g., ring-like features), as reported in previous works (e.g., Young et al. 1995). The radial distribution of molecular gas will be discussed in a forthcoming paper (Y. Miyamoto et al., in preparation). As described in subsection 3.1, the UGCA 86 and NGC 1569 spectra suffered from Galactic emission on the

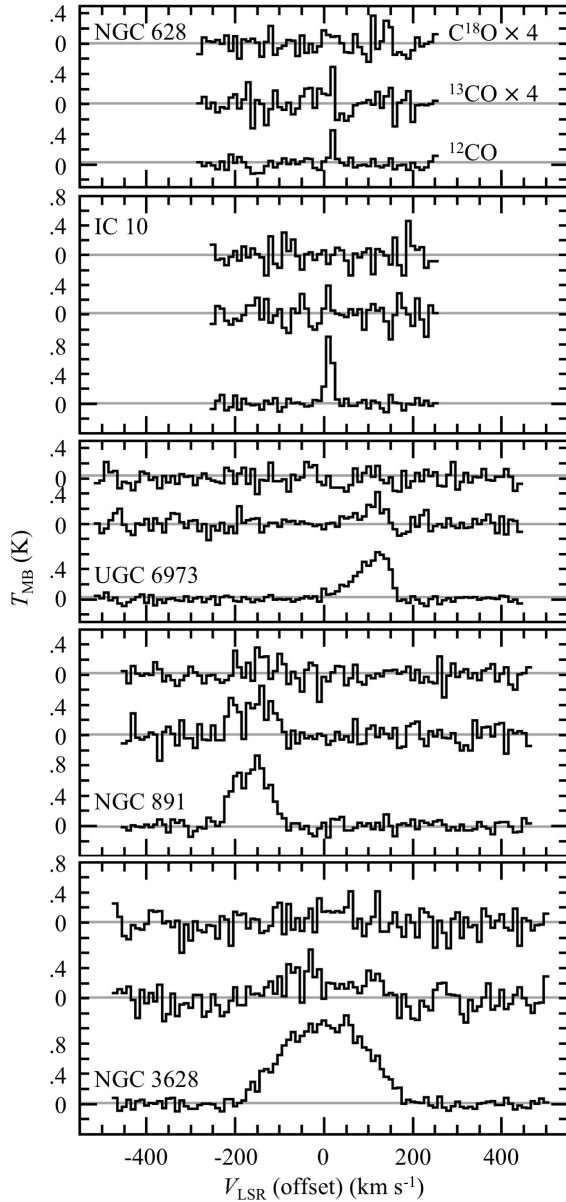


Fig. 16. Examples of the CO spectra for five galaxies. The galaxy name is shown in each panel. The three transitions of $C^{18}O \times 4$ (top), $^{13}CO \times 4$ (middle), and ^{12}CO (bottom) are shown in each panel.

off-source positions. The velocity of the Galactic emission slightly overlapped in the case of NGC 1569; thus, the integrated intensity suffered from a lower limit. The Galactic emission overlapped in the case of UGC A86; therefore, the integrated intensity included the contribution from the Galactic emission.

Panel (e) of figures 12 and 13 and supplementary figures 3 – 130 (supplementary section of the online version) show the integrated intensity maps of ^{13}CO of select galaxies. The ^{12}CO integrated intensity in each map was overlaid as white contours [the same as panel (b)]. Magenta contours are the level representing the significance of the ^{13}CO integrated intensity detection. The percentile level of the lowest contour in most cases is the same as the lowest one of ^{12}CO , except in cases where the ^{13}CO map is noisy. The sensitivity of our observations in ^{13}CO was insufficient; thus, the integrated intensity maps for this line suffered from considerable noise contamination. We only presented herein the galaxies with more than 3 pixels higher than 4σ in the ^{13}CO integrated intensity and higher than 3σ in the ^{12}CO integrated intensity.

Figures 17 – 19 depict the correlation plots between the ^{13}CO and ^{12}CO integrated intensities according to Pearson's product moment correlation coefficient between the integrated intensities $[\rho_{I(^{12}CO),I(^{13}CO)}]$. Figure 17 shows the galaxies with $|\rho_{I(^{12}CO),I(^{13}CO)}| \geq 0.7$, while figures 18 and 19 depict those with $0.4 \leq |\rho_{I(^{12}CO),I(^{13}CO)}| < 0.7$ and $|\rho_{I(^{12}CO),I(^{13}CO)}| < 0.4$, respectively. The data plotted in each panel are the pixels surrounded by the magenta contours in panel (e) of figures 12 and 13 and supplementary figures 3 – 130 (supplementary section of the online version). The correlation coefficient is an indicator of the resemblance, although the value does not necessarily reflect the apparent resemblance between the two maps.

A comparison of the integrated intensity maps in both lines and correlation plots indicated that approximately 20 of the ^{13}CO integrated intensity maps (galaxies shown in figures 19 and 18) were noticeably different to or at least dissimilar to those of ^{12}CO , although the S/N ratios of the ^{13}CO integrated intensity maps were poorer. About half of the lower $\rho_{I(^{12}CO),I(^{13}CO)}$ shown in figure 19 (i.e., NGC 157, NGC 278, NGC 2633, NGC 3655, NGC 5005, NGC 5678, NGC 5676, and NGC 6574) and two galaxies in figure 18 (i.e., NGC 4030 and NGC 4258) exhibited a depletion of the ^{13}CO emission in the central region. These galaxies had an H II region-like AGN, which suggests a ^{13}CO depletion in the central region (Taniguchi & Ohya 1998; Taniguchi et al. 1999). In NGC 3627, the ^{12}CO integrated intensity map showed the brightest peak at the center of the galaxy and two secondary peaks at each bar end, while the ^{13}CO integrated intensity map showed

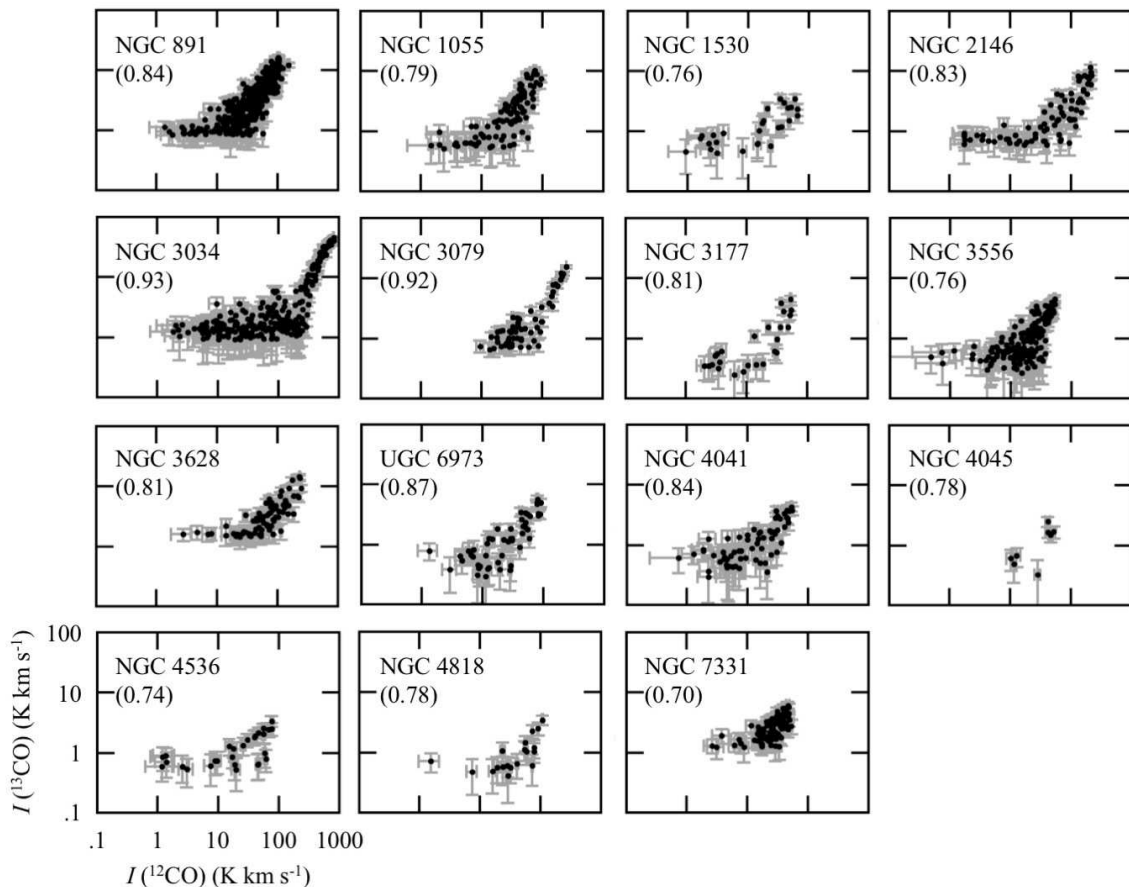


Fig. 17. Correlation plots between the ^{13}CO and ^{12}CO integrated intensities for galaxies whose Pearson's product moment correlation coefficient between both integrated intensities $[\rho_{I(^{12}\text{CO}), I(^{13}\text{CO})}]$ is higher than or equal to 0.7. The correlation coefficient is shown in parentheses below the galaxy name. The data in the pixels surrounded by the magenta contours in the ^{13}CO integrated intensity maps are plotted. The error bars are shown in gray lines.

the brightest peak at the northern bar end as shown in Watanabe et al. (2011). In NGC 660 and NGC 4666, the ^{12}CO integrated intensity maps illustrated a single peak distribution located at the center of the galaxies, while the ^{13}CO maps presented another peak and the central one. In the case of NGC 660, the off-center peak was brighter than the central peak in ^{13}CO . The peaks at the two bar ends in the ^{13}CO integrated intensity map were found in NGC 4527. The enhancement of the ^{13}CO emission at the bar ends was caused by the higher molecular gas density (Watanabe et al. 2011; Yajima et al. 2019).

The fact that the ^{12}CO and ^{13}CO maps significantly differed in some galaxies suggests that the physical properties of the molecular gas and/or abundances are not constant within a galaxy. We can also obtain the spectra with high significance in both CO lines when we stack the data with the same morphological characteristics (e.g., spiral arms or the bar) by aligning their spectra using the velocity field (Schruba et al. 2011; Morokuma-Matsui et al. 2015). Such stacked ^{13}CO spectra were made and compared with ^{12}CO

in Muraoka et al. (2016) and Yajima et al. (2019).

The integrated intensity maps of C^{18}O were only presented for NGC 891 (figure 12f or supplementary figure 12f), NGC 1055 (supplementary figure 14f), and NGC 3034 (supplementary figure 42f) in the supplementary section of the online version. These galaxies were those with more than 2 pixels higher than 4σ in C^{18}O integrated intensity and higher than 3σ in ^{12}CO integrated intensity. All these galaxies were edge-on; thus, the column density of the molecular gas can be obtained. The S/N ratios of the C^{18}O integrated intensity maps were much lower than those of ^{13}CO because the C^{18}O emission was comparatively weaker. The stacking of spectra via velocity alignment could lead to the C^{18}O detection in some galaxies.

Panels (c) and (d) of figures 12 and 13 and supplementary figures 1 – 132 (supplementary section of the online version) show the first- and second-degree moment maps in ^{12}CO . These maps were made through masking (subsection 5.1); thus, the emission patterns in these maps were more smoothed and extended compared to the integrated

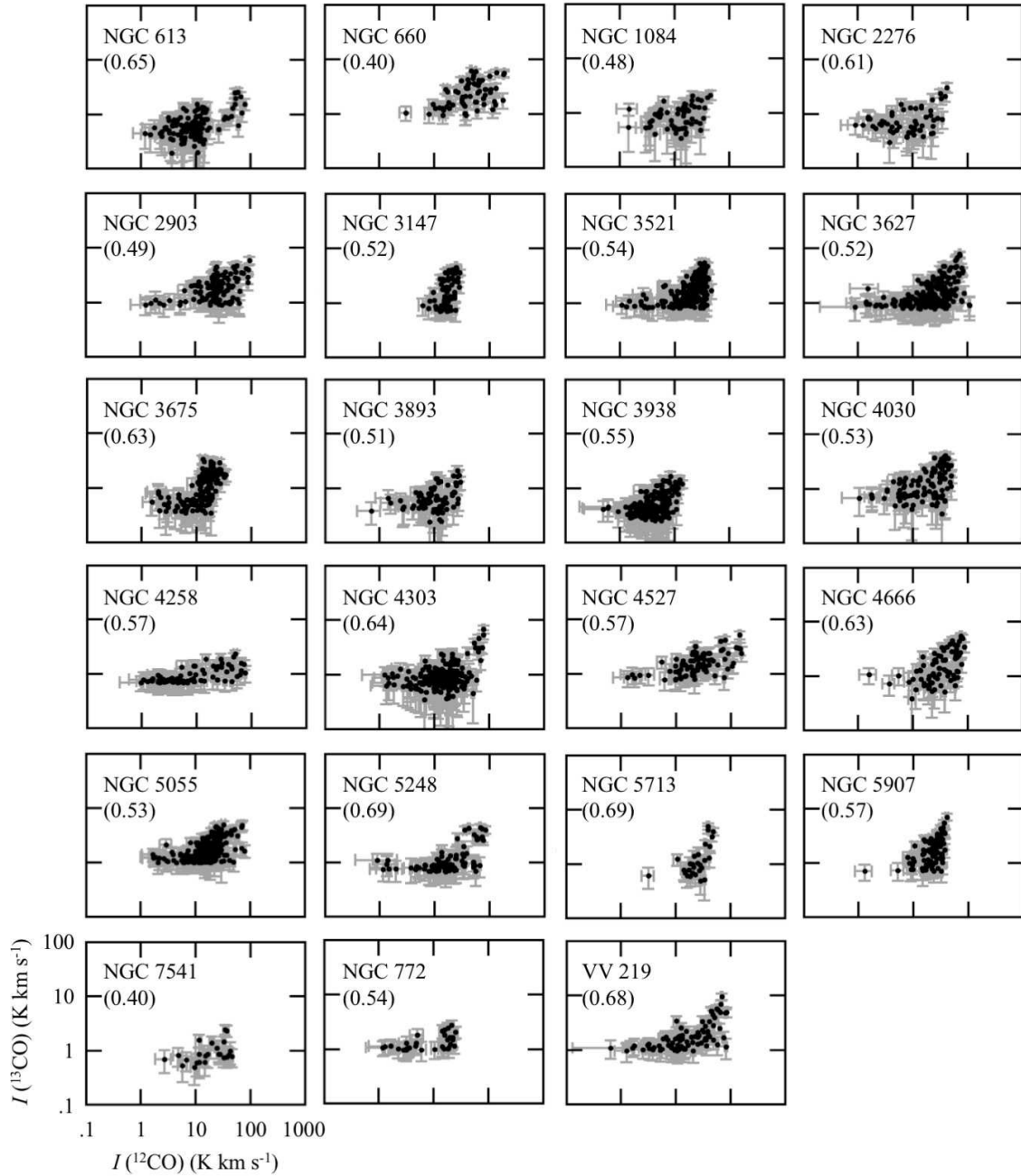


Fig. 18. Same as figure 17, but for galaxies with $0.4 \leq |\rho_{I(^{12}\text{CO}), I(^{13}\text{CO})}| < 0.7$.

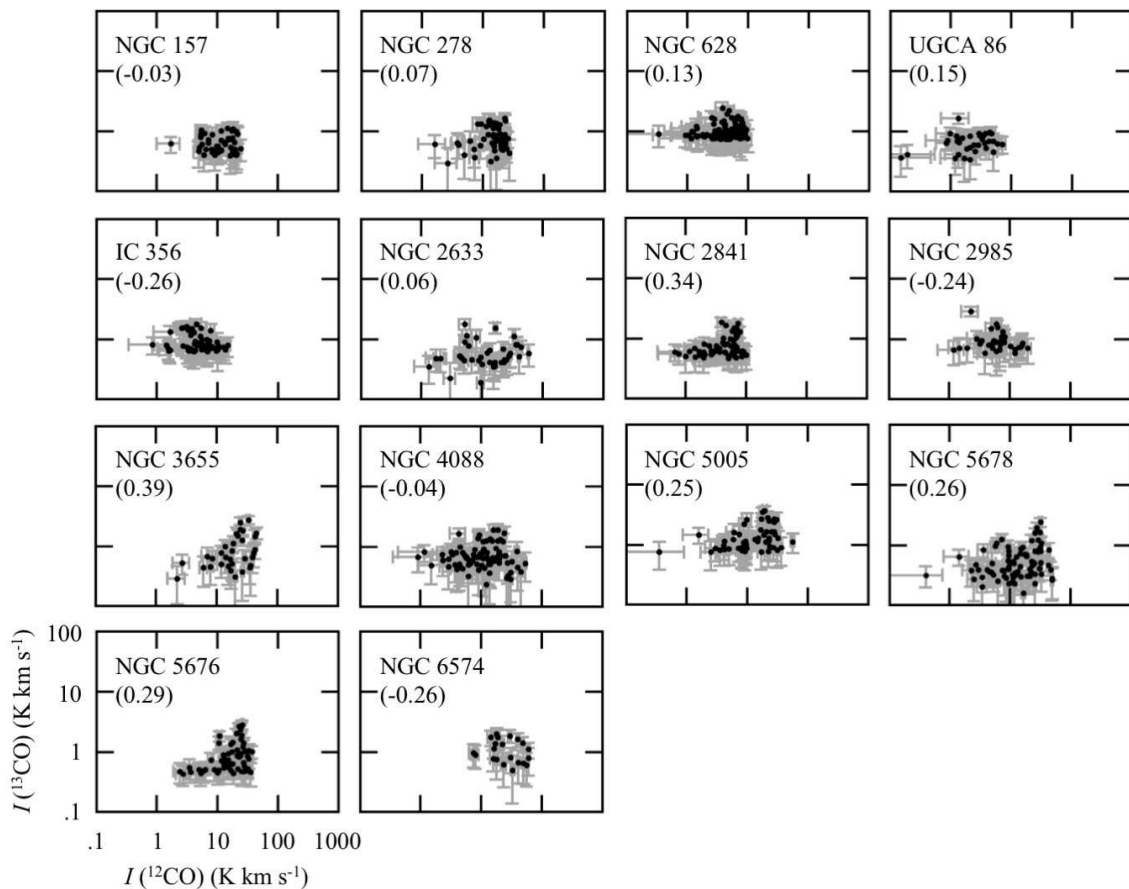


Fig. 19. Same as figure 17, but for galaxies with $|\rho_{I(12\text{CO}), I(13\text{CO})}| < 0.4$.

intensity maps. However, even after this step, some spiky noise remained, and had a smearing effect on the moment maps. The discrepancy between the emission extents in the moment maps and the integrated intensity map was remarkable in the case where the emission in each pixel in the integrated intensity map was just below the 4σ threshold. One of the noticeable cases was that of IC 356. On the contrary, such masking created zero emission pixels for the first- and second-degree moment maps of some galaxies. These moment maps were not presented in the figures for the 19 galaxies, including the two paired galaxies.

Most of the first-degree moment maps presented a circular rotation pattern, while most of the second-degree moment maps presented the highest velocity dispersion in the central region of the galaxy. Such velocity fields made it possible to judge the receding side of the galaxy major axis. Table 1 shows the results. The velocity field of NGC 2967 in supplementary figure 39 predicted a very different PA from the one listed in table 1, which was derived from its outer disc (Salo et al. 2015). A more detailed analysis also showed that the PA of the inner disc of NGC 2967 was

different from the abovementioned adopted value (Salak et al. 2019). The rotation curve of the molecular gas, PA, and i measured by fitting molecular gas distribution will be presented in Y. Miyamoto, et al. (in preparation). The molecular gas dynamics was discussed in Salak et al. (2019) along with the kinematically determined PA and i .

6.2 Mass

The total CO luminosity ($L'_{12\text{CO}}$ in units $\text{K km s}^{-1} \text{pc}^2$; Solomon et al. 1992) and the corresponding molecular mass (M_{mol}) within the observed region were calculated. The CO emission was essentially confined within the mapped region (subsection 3.1); therefore, these luminosities and masses were effectively the total CO luminosity and the gas mass within $R_{3.4\mu\text{m}}$. Table 4 lists both quantities. We did not use the total molecular gas mass in UGCA 86 hereafter because the estimated value had a large uncertainty, as described in subsection 6.1.

The M_{mol} distribution along the Hubble sequence indicates that galaxies with Sb and Sbc types have the tendency to host a larger molecular gas content, although the

scatter is considerable (figure 20a). The geometric mean value of M_{mol} highlighted this trend, showing this peak and noticeably lower values in the irregular and peculiar galaxies. This trend was consistent with that in the previous works (Komugi et al. 2008). The distribution of the total stellar mass (M_{star}) along the Hubble sequence was similar to that of the total molecular gas (figure 20b).

The fraction of the total molecular gas mass to the total stellar mass, $M_{\text{mol}}/M_{\text{star}}$, showed no clear trend against the Hubble type (figure 20c). Despite our sample having a strong bias toward molecular gas-rich FIR bright galaxies, these results were consistent with more complete observational samples [e.g., those of Saintonge et al. (2011) (showing no difference in the concentration index rather than the Hubble type), Boselli, et al. (2014b), Bolatto et al. (2017), and Young & Scoville (1991) (comparing the ratio of the molecular gas mass to the dynamical mass)]. We also showed herein the fraction of the total molecular gas mass to the total baryonic mass, that is, the sum of the molecular and stellar masses [$M_{\text{mol}}/(M_{\text{mol}} + M_{\text{star}})$] along the Hubble sequence in figure 20d. The molecular gas mass fraction was small; thus, the tendency of $M_{\text{mol}}/(M_{\text{mol}} + M_{\text{star}})$ was very similar to that of $M_{\text{mol}}/M_{\text{star}}$. We ignored the atomic gas mass because it typically contributed much less than the molecular gas to the baryonic mass within a radius where the molecular gas was dominant (Honma et al. 1995). Thus, hereafter, we used $M_{\text{mol}}/M_{\text{star}}$ as a proxy for molecular gas to baryon ratio.

M_{mol} correlated with M_{star} over three orders of magnitude (figure 21). That is, M_{mol} increased with M_{star} . This trend was already predicted in figure 20, in which M_{mol} and M_{star} behaved in a similar way, and $M_{\text{mol}}/M_{\text{star}}$ was constant over the Hubble types. Although we applied the standard conversion factor to every location in each galaxy, the factor is not constant, and could depend on the physical and chemical conditions of molecular gas (e.g., Kennicutt & Evans 2012; Bolatto et al. 2013). Deriving variable conversion factors in various positions in individual galaxies and calculating a more precise molecular gas mass will be reported in a future study. The relation between the molecular gas and the star formation in these samples was presented in Muraoka et al. (2019) and will be also reported in a future study.

We also showed the relation between $M_{\text{mol}}/M_{\text{star}}$ and M_{star} in figure 22. The errors were comparable to or smaller than the size of each marker. The relation between both quantities was expected to provide a constraint on constructing the galaxy formation and evolution models (Morokuma-Matsui & Baba 2015; Saintonge et al. 2017). The span was similar to the results for the local galaxies in the previous works, in which a decreasing trend after

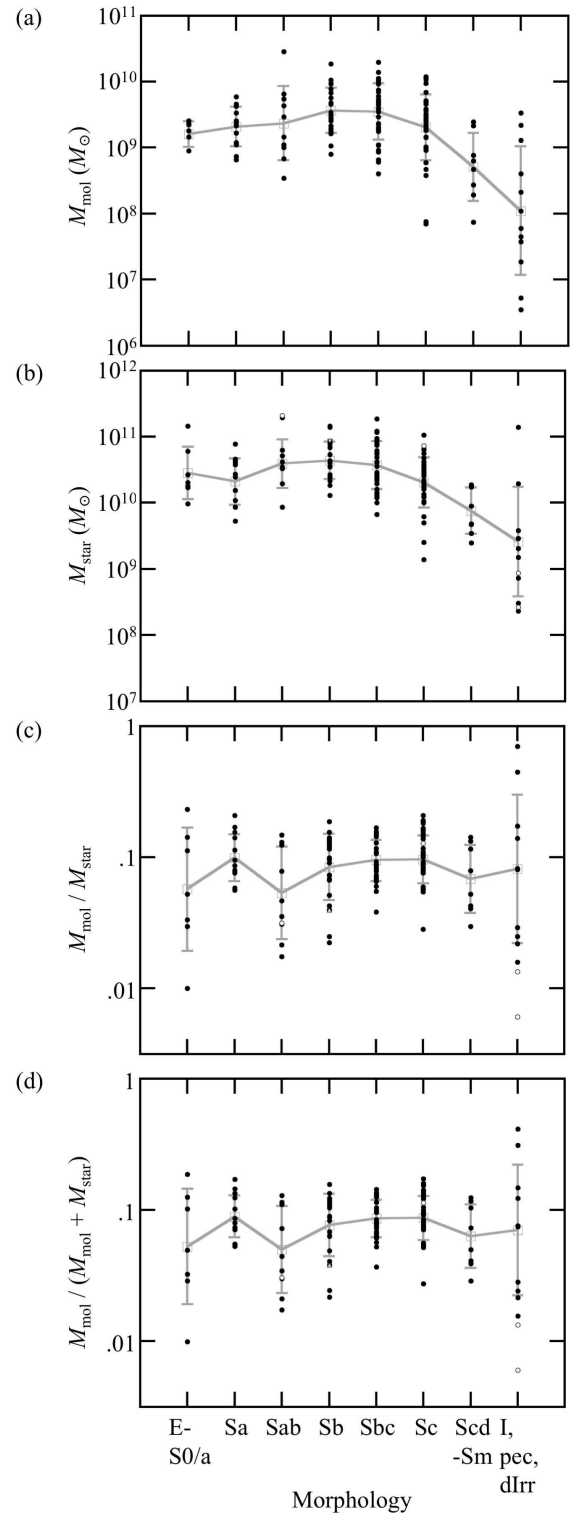


Fig. 20. Distribution of the total molecular gas mass M_{mol} (a), total stellar mass M_{star} (b), fraction of the molecular gas mass to the stellar mass $M_{\text{mol}}/M_{\text{star}}$ (c), and fraction of the molecular gas mass to the total mass $M_{\text{mol}}/(M_{\text{mol}} + M_{\text{star}})$ (d) along the morphological type. The open circles indicate the data with a large uncertainty (see text). The open downward triangle in (b) indicates an upper limit on M_{star} , while the open upward triangle in (c) and (d) indicates a lower limit on $M_{\text{mol}}/M_{\text{star}}$ and $M_{\text{mol}}/(M_{\text{mol}} + M_{\text{star}})$. The open squares linked with the lines are the averaged value with the standard deviation for each morphological type.

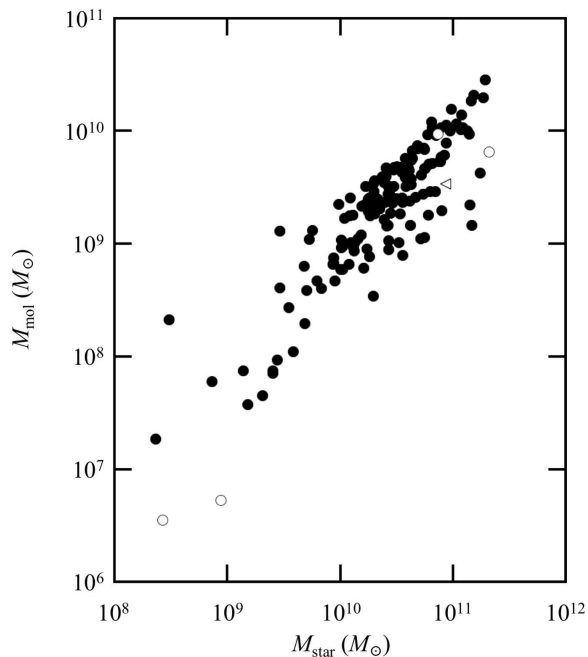


Fig. 21. Relation between the molecular gas mass M_{mol} and the stellar mass M_{star} . The typical errors are smaller than the size of each marker. The open circles indicate M_{star} with a considerable uncertainty. The open leftward triangle indicates an upper limit on M_{star} .

around $M_{\text{star}} \sim 10^{10} M_{\odot}$ (Jiang et al. 2015; Morokuma-Matsui & Baba 2015; Bolatto et al. 2017; Saintonge et al. 2017) was observed. We also showed herein the same plots divided by the morphologies in figures 23 and 24. A power law was fitted in each plot (solid line). Table 5 lists the fitted slope and Pearson’s product moment correlation coefficient. Although no clear tendency was seen along the Hubble sequence, $M_{\text{mol}}/M_{\text{star}}$ decreased with M_{star} in the early-type galaxies (E – S0 and Sa), but increased in the late-type spirals (Sc and Scd – Sm). It also effectively showed an uncorrelated scatter in intermediate types and irregular galaxies (figure 23). The fraction seemed to increase with M_{star} for the SB galaxies; however, no clear difference was seen among the SA and SAB galaxies (figure 24). Thus, this tendency probably resulted from the bias of our samples because SB had predominantly less massive galaxies with irregular or peculiar morphology.

6.3 Molecular gas content in the barred and non-barred spirals

Figures 25 – 27 show a comparison of the distributions of M_{mol} , M_{star} , and $M_{\text{mol}}/M_{\text{star}}$ over different bar morphological types. The M_{mol} and M_{star} histograms for the non-barred and barred spirals were very similar, although some SB galaxies had a very low M_{mol} or M_{star} .

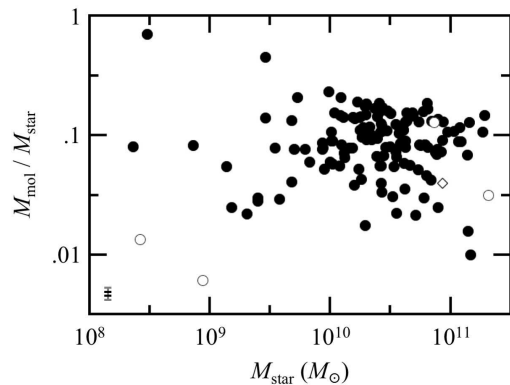


Fig. 22. Molecular gas to stellar mass fraction $M_{\text{mol}}/M_{\text{star}}$ versus stellar mass M_{star} . The open circles indicate M_{star} (and $M_{\text{mol}}/M_{\text{star}}$) with a considerable uncertainty. The open diamond indicates the upper limit on M_{star} (and lower limit on $M_{\text{mol}}/M_{\text{star}}$). The typical (black) and maximum (gray) errors are shown in the bottom-left corner.

A Kolmogorov-Smirnov (K-S) test cannot reject the null hypothesis that the M_{mol} or M_{star} distribution coincides in the barred and non-barred spirals at a significant level of 10%. The $M_{\text{mol}}/M_{\text{star}}$ fraction did not correlate with the presence of bars, with each type spanning the same range of $M_{\text{mol}}/M_{\text{star}}$, although there seems a slight preference for higher values in the SA galaxies. A K-S test cannot reject the null hypothesis that the two populations are drawn from the same distribution at a significant level of 10%.

In contrast to our results that M_{mol} , M_{star} , and $M_{\text{mol}}/M_{\text{star}}$ do not depend on the bar presence, previous works showed that $M_{\text{mol}}/M_{\text{star}}$ may be lower in the barred spirals. Figure 28 shows the histograms of M_{star} and $M_{\text{mol}}/M_{\text{star}}$ for the non-barred and barred galaxies, respectively, in the EDGE sample (Bolatto et al. 2017). Data from the COMING overlaid as dashed lines suggested that the barred spiral galaxies in our sample were less massive in M_{star} and prone to have a higher $M_{\text{mol}}/M_{\text{star}}$. The EDGE sample consisted of rather more massive galaxies in stellar mass than the COMING samples, especially for the barred spiral galaxies. A K-S test indicated the hypothesis that both survey samples coming from the same population are rejected at 1% significance. Although the K-S test did not indicate a significant difference for the non-barred galaxies between both samples, it implied that the hypothesis was rejected at 2.5% significance for the barred galaxies. The possibility of a lower $M_{\text{mol}}/M_{\text{star}}$ in the barred galaxies was suggested in Bolatto et al. (2017), although their K-S test indicated a low significance.

Our sample selection was biased toward the FIR bright galaxies, that is, gas-rich galaxies, which may result in this discrepancy. Figure 29 shows the fraction of the barred

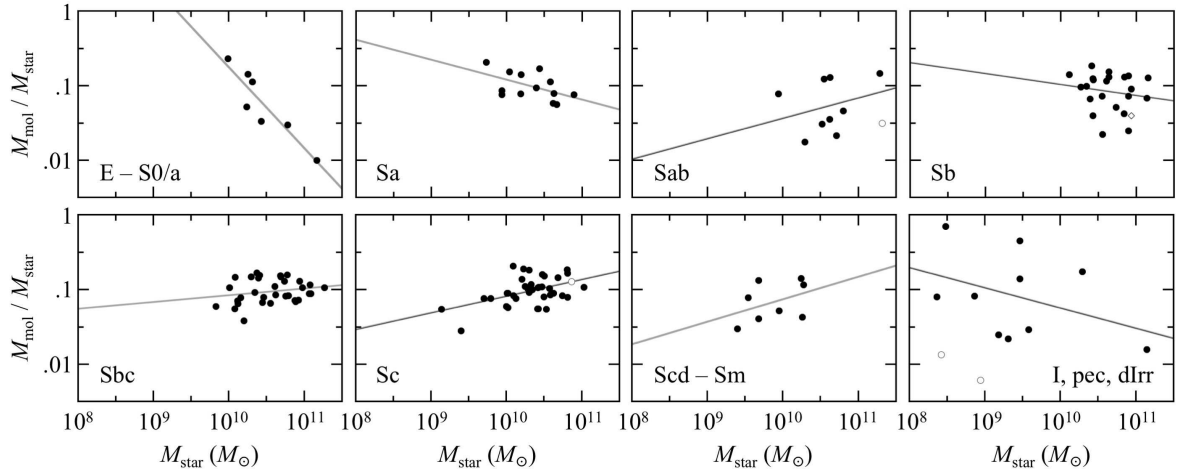


Fig. 23. Same as figure 22, but as a function of the Hubble types. The solid line indicates the power law fitting. The data shown as open circles and open diamond are not used for the fitting.

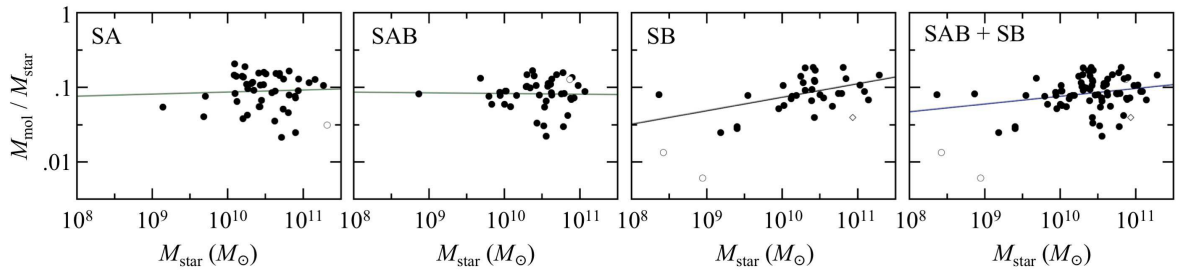


Fig. 24. Same as figure 23, but as a function of the existence of a bar or not. The galaxies not classified into these categories are not shown.

galaxies in our sample (SAB+SB) (f_{bar}) for a given M_{star} as well as that of EDGE (Bolatto et al. 2017) and S⁴G (Díaz-García et al. 2016). The dependency of f_{bar} on M_{star} was different from the previous works. Díaz-García et al. (2016) indicated that the bar fraction increased with the stellar mass in the S⁴G samples. Algorry et al. (2017) studied the population of the barred galaxies in the EAGLE cosmological simulation and found that the gas mass fraction decreased with the bar strength parameter. In other words, barred spiral galaxies were prone to having a lower gas mass fraction. Spinoso et al. (2017) predicted that gas is driven inward and consumed by star formation in the barred galaxies in cosmological simulations. Observational results also concurred with those predictions (Cheung et al. 2013; Chown et al. 2019). Our sample consisted of gas-rich galaxies; barred spiral galaxies with high M_{star} and low f_{gas} were not included; and those with lower M_{star} and higher $M_{\text{mol}}/M_{\text{star}}$ were selectively included in our sample, thereby causing similar M_{mol} , M_{star} , and $M_{\text{mol}}/M_{\text{star}}$ distributions between the barred and non-barred spiral galaxies seen in our sample.

7 Summary and conclusion

In this study, we simultaneously conducted COMING, an OTF-mapping survey project, targeting 147 nearby galaxies in ¹²CO, ¹³CO, and C¹⁸O $J=1-0$ lines using the NRO 45 m radio telescope. The spatial resolution was 17". The velocity resolution was set to 10 km s⁻¹. The sensitivity was typically $T_{\text{MB}} = 70$ mK. Each mapping region covered 70% of the optical diameter D_{25} , which was expected to encompass all CO emissions, as indicated by the previous observations. The targets were selected from nearby galaxies based on the FIR flux. In other words, they were strongly biased to the FIR brightness. Some interacting galaxies were selected despite not satisfying the selection criteria because the counterpart of the paired galaxies satisfied the criteria. We only completed observations for 147 out of the 238 galaxies in the selected sample because of the observing limitations. The fractions of the barred and non-barred galaxies in the sample were similar, but we concentrated on those with the Hubble-type Sb–Sc. The galaxies with smaller disc lengths were a dominant component of the observed sample. The FITS cubes with 6"

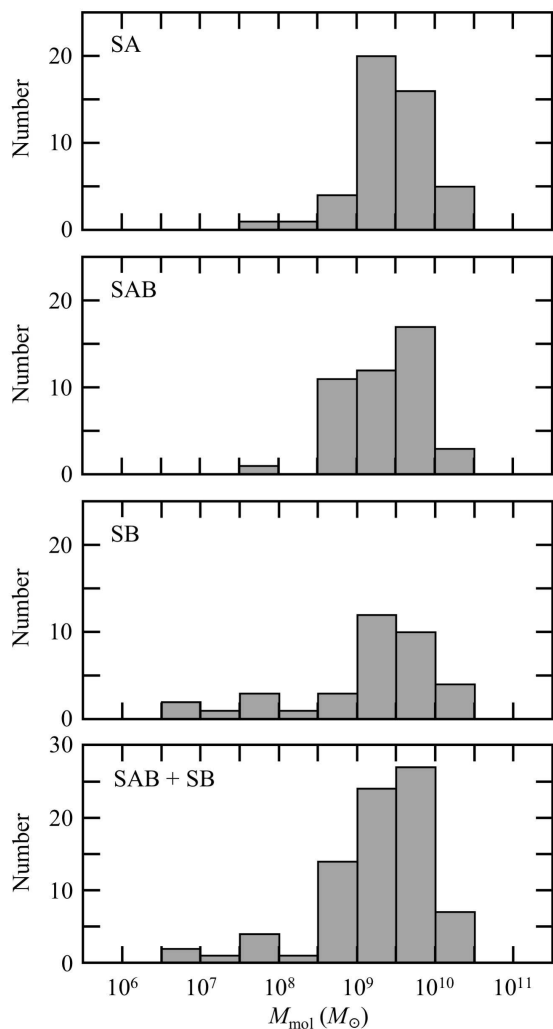


Fig. 25. Histograms of the total molecular gas mass M_{mol} for bar types SA, SAB, SB, and SAB + SB.

spacing in the three lines are publicly available at the JVO archive.

We developed an observation ranking system and automatic data reduction tools to optimize resource observation and ensure that reduction is fully reproducible and highly efficient. We quantified the relative positions between the direction of the telescope and the available targets and made assessments based on the target elevation and size while considering the system noise and other factors to maximize the quantity of the observed galaxies in the allotted time. This system was introduced in the last two observation seasons and resulted in the reduction of the total observing time to complete a map typically by 37%. We also developed the tools **auto-flag** and **auto-rebase**. The former quantified the undulation of the spectral baselines and removed heavily undulated spectra in

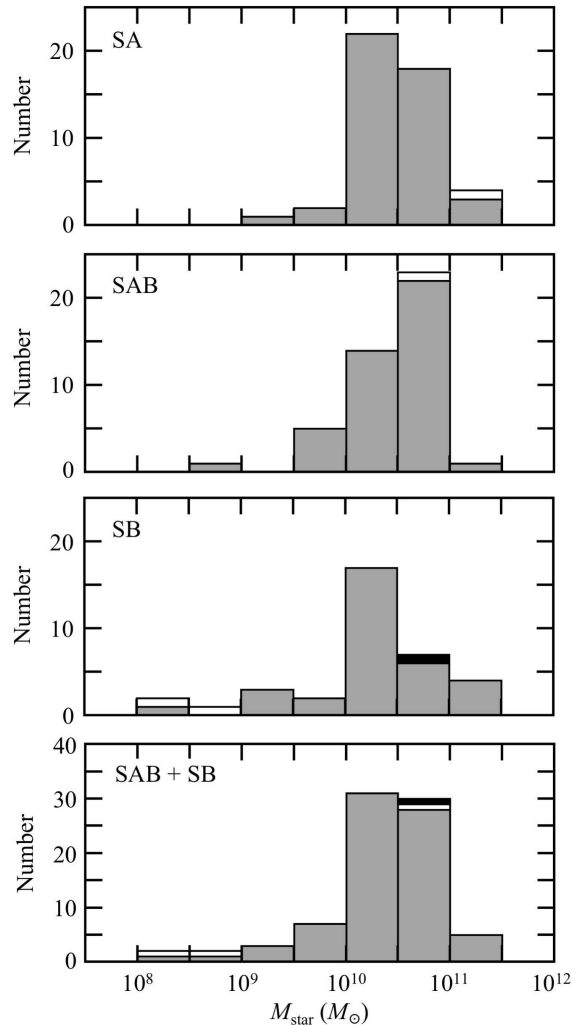


Fig. 26. Same as figure 25, but for the stellar mass M_{star} . The open columns indicate M_{star} with a considerable uncertainty. The black filled column indicates the upper limit on M_{star} .

the OTF data. Meanwhile, **auto-rebase** determined the zero levels in the spectra with ambiguous features. These tools are a part of the COMING ART PYTHON package designed to optimize the objectivity and reproducibility of the reduction process.

The radii and the total stellar mass of the observed galaxies were measured from the WISE $3.4\ \mu\text{m}$ archival data. The radius, $R_{3.4\ \mu\text{m}}$, was 30% larger than the optical radius for most targets. The total stellar mass, M_{star} , was measured within $R_{3.4\ \mu\text{m}}$ following the method of Wen et al. (2013). Our derived M_{star} was approximately 20% less massive than the mass derived in S⁴G (Sheth et al. 2010) for 115 overlapping galaxies between our project and S⁴G. The offset may be caused by our conservative star masking method which masks slightly larger area than the extent of stars and background subtraction, and possibly a mi-

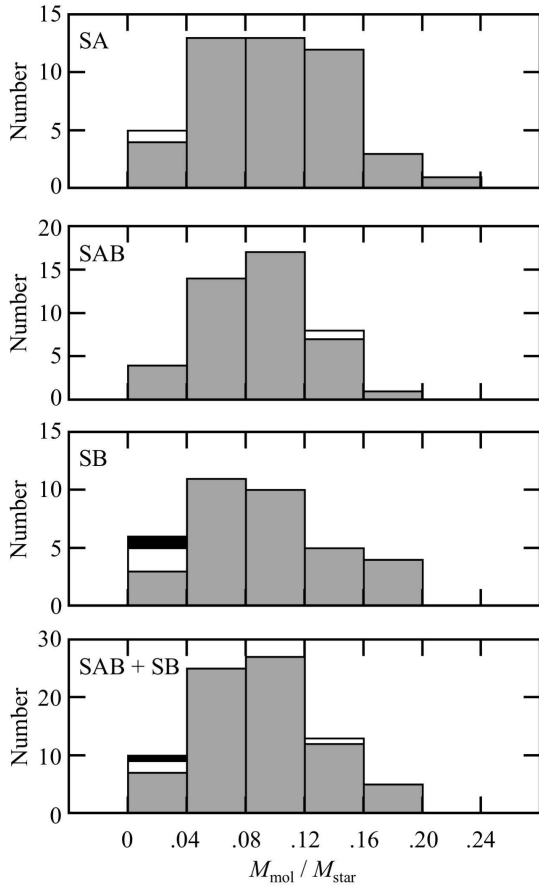


Fig. 27. Same as figure 25, but for $M_{\text{mol}}/M_{\text{star}}$. The open columns indicate $M_{\text{mol}}/M_{\text{star}}$ with a considerable uncertainty. The black filled column indicates the lower limit on $M_{\text{mol}}/M_{\text{star}}$.

nor offset between the WISE $3.4\mu\text{m}$ band and the Spitzer $3.6\mu\text{m}$ band flux at a higher magnitude (Wen et al. 2013).

The ^{12}CO emission was detected in most of the observed galaxies, while the ^{13}CO emission was detected in approximately a third of the galaxies with a low S/N ratio. The C^{18}O emission was detected in only $\lesssim 10$ targets. Some integrated intensity maps in ^{12}CO indicated a similar distribution to the stellar distribution, while some displayed quite different morphologies. Some galaxies also showed differences in the locations of the ^{12}CO and ^{13}CO emission, although the S/N ratio of ^{13}CO was rather low in most cases. This result implied that the molecular gas properties in the galactic discs were not uniform. The C^{18}O maps were only successfully created in three of our targets, namely NGC 891, NGC 1055 and NGC 3034. Additionally, the first- and second-degree moment maps in CO were created for the majority of our sample.

The total molecular gas mass, M_{mol} , measured using the standard conversion factor correlated well with M_{star} over three orders of magnitude. Moreover, the ratio $M_{\text{mol}}/M_{\text{star}}$

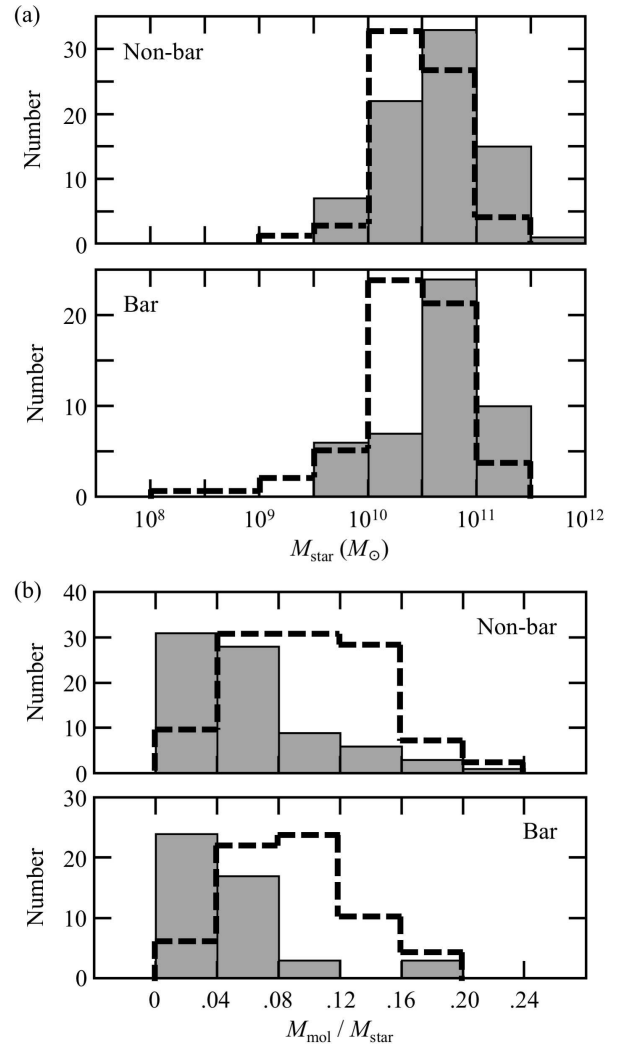


Fig. 28. (a) Histograms of the total stellar mass M_{star} for the non-barred and barred galaxies in the EDGE sample (Bolatto et al. 2017). The dashed line indicates the COMING results shown in figure 26 for SA and SAB + SB. (b) Same as (a), but for $M_{\text{mol}}/M_{\text{star}}$. The dashed line indicates the COMING results shown in figure 27 for SA and SAB + SB. The COMING results are normalized for the peak to correspond to that of the EDGE results, and the data with uncertainty or upper/lower limit data are not used.

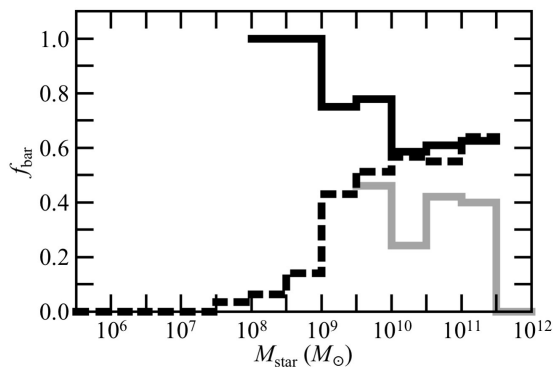


Fig. 29. Bar fraction f_{bar} of the COMING sample as a function of the stellar mass M_{star} (black solid). The data with a large uncertainty or the upper limit data are not used. The fractions of the EDGE sample (Bolatto et al. 2017) (gray solid) and S⁴G (Díaz-García et al. 2016) (black dashed) are shown.

did not depend on the Hubble type. Galaxies with Sb and Sbc types have the tendency to host a larger M_{mol} or M_{star} , although the scatter is considerable. The trend of $M_{\text{mol}}/M_{\text{star}}$ relation was consistent with that in the previous works, although the scatter was considerable. However, $M_{\text{mol}}/M_{\text{star}}$ seemed to decrease with M_{star} in early-type galaxies and vice versa in late-type galaxies.

M_{mol} and $M_{\text{mol}}/M_{\text{star}}$ did not show dependence on the presence of bars, but this was likely the result of our sample selection criteria. We saw no differences in the mass distribution of M_{mol} and M_{star} between the barred and non-barred spirals; however, we found that the SB types had a lower mass tail in the M_{mol} and M_{star} distribution. No difference of $M_{\text{mol}}/M_{\text{star}}$ was seen between the barred and non-barred spirals, although the previous works suggested the possibility of a comparatively lower $M_{\text{mol}}/M_{\text{star}}$ in the barred spirals (Bolatto et al. 2017). The fraction of the barred spirals as a function of M_{star} also showed a trend opposite to that in the previous works. This difference was caused by our sample selection, in which we prioritized observing the FIR bright (thus, molecular gas-rich) galaxies. The barred spirals are effective at funneling molecular gas toward their central regions, resulting in a molecular gas deficit in their discs. Thus, the molecular gas-rich barred spirals had a lower M_{star} .

This survey was conducted toward approximately 150 galaxies, observing the ^{12}CO distribution over their entire disc area and revealing the large-scale distribution of their entire molecular gas budget. These data act as a benchmark for comparison with the targeted observations of more distant galaxies, interferometric observations of our sample galaxies, observations in higher- J lines, and those with very high spatial resolutions of specific regions of external galaxies. Our sample was composed of nearby

galaxies, and, as such, a wealth of archival data across multiple wavelengths was already available. Thus, COMING acts as an excellent resource for studies of the interstellar medium and star formation in galaxies on kpc scales.

Supplementary data

The following supplementary data is available at PASJ online.

Supplementary figures 1–134.

WISE $3.4\mu\text{m}$ image, integrated intensity map, first-degree moment map and second-degree moment map of ^{12}CO ($J = 1 - 0$) for all the observed galaxies [panels (c) and (d) were not presented in 17 figures], integrated intensity maps of ^{13}CO ($J = 1 - 0$), and C^{18}O ($J = 1 - 0$) for some galaxies are shown in each figure.

Acknowledgments

The authors thank the referee for very many and invaluable comments and suggestions, which significantly improved the manuscript. We would also like to gratefully acknowledge Alex Pettitt for his helping to improve the paper greatly. We are grateful to the NRO staff for the operation of the 45 m telescope and their continuous efforts to improve the performance of the instruments. This work is based on one of the legacy programs of the Nobeyama 45 m radio telescope, which is operated by Nobeyama Radio Observatory, a branch of National Astronomical Observatory of Japan. This research has made use of the NASA/IPAC Extragalactic Database (NED) which is operated by the Jet Propulsion Laboratory, California Institute of Technology, under contract with the National Aeronautics and Space Administration. This publication makes use of data products from the Wide-field Infrared Survey Explorer, which is a joint project of the University of California, Los Angeles, and the Jet Propulsion Laboratory/California Institute of Technology, funded by the National Aeronautics and Space Administration. HK is supported by JSPS KAKENHI Grant Number 18K13593.

References

- Alatalo, K., et al. 2013, MNRAS, 432, 1796
- Alatalo, K., et al. 2015, MNRAS, 450, 3874
- Algorry, D. G., et al. 2017, MNRAS, 469, 1054
- Anderson, J. M., & Ulvestad, J. S. 2005, ApJ, 627, 674
- Antonio García-Barreto, J., & Rosado, M. 2001, AJ, 121, 2540
- Argyle, R. W., & Eldridge, P. 1990, MNRAS, 243, 504
- Arnold, J. A., et al. 2014, ApJ, 791, 80
- Ball R. 1986, ApJ, 307, 453
- Bauermeister, A., et al. 2013, ApJ, 768, 132
- Becker, R. H., White, R. L., & Helfand, D. J. 1995, ApJ, 450, 559
- Bolatto, A. D., et al. 2017, ApJ, 846, 159
- Bolatto, A. D., Wolfire, M., & Leroy, A. K. 2013, ARA&A, 51,

- 207
- Boselli, A., Cortese, L., & Boquien, M. 2014a, *A&A*, 564, 65
- Boselli, A., Cortese, L., Boquien, M., Boissier, S., Catinella, B., Lagos, C., & Saintonge, A. 2014b, *A&A*, 564, 66
- Bottinelli, L., Gougouenheim, L., Paturel, G., & de Vaucouleurs, G. 1984a, *A&AS*, 56, 381
- Bottinelli, L., Gougouenheim, L., Paturel, G., & Teerikorpi, P. 1984b, *A&A*, 156, 157
- Bravo-Alfaro, H., Brinks, E., Baker, A. J., Walter, F., & Kunth, D. 2004, *AJ*, 127, 264
- Bresolin, F., Schaerer, D., González, R. M., & Stasińska, G. 2005, *A&A*, 441, 981
- Broeils, A. H., & van Woerden, H. 1994, *A&AS*, 107, 129
- Bushouse, A. H., Telesco, C. M., & Werner, M. W. 1998, *AJ*, 115, 938
- Cao, Y., Wong, T., Xue, R., Bolatto, A. D., Blitz, L., Vogel, S. N., Leroy, A. K., & Rosolowsky, E. 2017, *ApJ*, 847, 33
- Caso, J. P., Bassino, L. P., & Gómez, M. 2015, *MNRAS*, 453, 4421
- Chabrier, G. 2003, *ApJ*, 586, L133
- Cheung, E., et al. 2013, *ApJ*, 779, 162
- Chown, R., et al. 2019, *MNRAS*, 484, 5192
- Chung, A., van Gorkom, J. H., Kenney, J. D. P., Crowl, H., & Vollmer, B. 2009a, *AJ*, 138, 1741
- Chung, E. J., Rhee, M. -H., Kim, H., Yun, M. S., Heyer, M., & Young, J. S. 2009b, *ApJS*, 184, 199
- Clements, E. D. 1981, *MNRAS*, 197, 829
- Clements, E. D. 1983, *MNRAS*, 204, 811
- Colombo, D., et al. 2014, *ApJ*, 784, 3
- Condon, J. J., & Broderick, J. J. 1991, *AJ*, 102, 1663
- Condon, J. J., Cotton, W. D., Greisen, E. W., Yin, Q. F., Perley, R. A., Taylor, G. B., & Broderick, J. J. 1998, *AJ*, 115, 1693
- Cooray, S., Takeuchi, T. T., Yoda, M., & Sorai, K. 2019, *PASJ*, submitted
- Cormier, D., et al. 2018, *MNRAS*, 475, 3909
- Crosthwaite, L. P., Turner, J. L., Buchholz, L., Ho, P. T. P., & Martin, R. N. 2002, *AJ*, 123, 1892
- Daddi, E., et al. 2010, *ApJ*, 713, 686
- Daigle, O., Carignan, C., Amram, P., Hernandez, O., Chemin, L., Balkowski, C., & Kennicutt, R. 2006, *MNRAS*, 367, 469
- de Blok, W. J. G., Walter, F., Brinks, E., Trachternach, C., Oh, S.-H., & Kennicutt, R. C., Jr. 2008, *AJ*, 136, 2648
- Dessauges-Zavadsky, M., et al. 2015, *A&A*, 577, 50
- Dessauges-Zavadsky, M., et al. 2017, *A&A*, 605, 81
- de Vaucouleurs, G., de Vaucouleurs, A., Corwin Jr., H. G., Buta, R. J., Paturel, G., & Fouque, P. 1991, *Third Reference Catalogue of Bright Galaxies* (New York: Springer)
- Dhungana, G., et al. 2016, *ApJ*, 822, 6
- Díaz, R. J., Dottori, H., Vera-Villamizar, N., & Carranza, G. 2003, *ApJ*, 597, 860
- Díaz-García, S., Salo, H., Laurikainen, E., & Herrera-Endoqui, M. 2016, *A&A*, 587, 160
- Donovan Meyer, J., et al. 2013, *ApJ*, 772, 107
- Elmegreen, D. M., Kaufman, M., Brinks, E., Elmegreen, B. G., & Sundin, M. 1995, *ApJ*, 453, 100
- Emerson, D. T., & Gräve, R., 1988, *A&A*, 190, 353
- Epinat, B., Amram, P., & Marcelin, M. 2008a, *MNRAS*, 390, 466
- Epinat, B., et al. 2008b, *MNRAS*, 388, 500
- Erroz-Ferrer, et al. 2015, *MNRAS*, 451, 1004
- Evans, I. N., et al. 2010, *ApJS*, 189, 37
- Fingerhut, R. L., et al. 2010, *ApJ*, 716, 792
- Fiorentino, G., Musella, I., & Marconi, M. 2013, *MNRAS*, 434, 2866
- Fraser-McKelvie, A., Brown, M. J. I., Pimblett, K. A., Dolley, T., Crossett, J. P., & Bonne, J. 2016, *MNRAS*, 462, L11
- Friedrich, S., Davies, R. I., Hicks, E. K. S., Engel, H., Müller-Sánchez, F., Genzel, R., & Tacconi, L. J. 2010, *A&A*, 519, 79
- Fuentes-Carrera, I., et al. 2004, *A&A*, 415, 451
- García-Burillo, S., Guélin, M., & Cernicharo, J. 1993, *A&A*, 274, 123
- García-Burillo, S., Guélin, M., & Neinger, N. 1997, *A&A*, 319, 450
- García Gómez, C., & Athanassoula, E. 1993, *A&AS*, 100, 431
- Garrido, O., Marcelin, M., Amram, P., & Boulesteix, J. 2002, *A&A*, 387, 821
- Geha, M., Guhathakurta, P., & van der Marel, R. P. 2005, *AJ*, 129, 2617
- Guhathakurta, P., van Gorkom, J. H., Kotanyi, C. G., & Balkowski, C. 1988, *AJ*, 96, 851
- Haan, S., Schinnerer, E., Mundell, C. G., García-Burillo, S., & Combes, F. 2008, *AJ*, 135, 232
- Hatakeyama, T., et al. 2017, *PASJ*, 69, 67
- Helfer, T. T., Thornley, M. D., Regan, M. W., Wong, T., Sheth, K., Vogel, S. N., Blitz, L., & Bock, D. C.-J. 2003, *ApJS*, 145, 259
- Helou, G., & Walker, D. W. 1988, *Infrared astronomical satellite (IRAS) catalogs and atlases. Volume 7*
- Hernandez, O., Carignan, C., Amram, P., Chemin, L., & Daigle, O. 2005, *MNRAS*, 360, 1201
- Herrnstein, J. R., Moran, J. M., Greenhill, L. J., & Trotte, A. S. 2005, *ApJ*, 629, 719
- Honma, M., Sofue, Y., & Arimoto, N. 1995, *A&A*, 304, 1
- Hota, A., & Saikia, D. J. 2006, *MNRAS*, 371, 945
- Huchra, J. P., Vogeley, M. S., & Geller, M. J. 1999, *ApJS*, 121, 287
- Hunt, L. K., et al. 2008, *A&A*, 482, 133
- Hunter, D. A., et al. 2012, *AJ*, 144, 134
- Irwin, J. A., & Sofue, Y. 1996, *ApJ*, 464, 738
- Jackson, N., Battye, R. A., Browne, I. W. A., Joshi, S., Muxlow, T. W. B., & Wilkinson, P. N. 2007, *MNRAS*, 376, 371
- James, P. A., et al. 2004, *A&A*, 414, 23
- Jarrett, T. H., Chester, T., Cutri, R., Schneider, S. E., & Huchra, J. P. 2003, *AJ*, 125, 525
- Jiang, X.-J., Wang, Z., Gu, Q., Wang, J., & Zhang, Z.-Y. 2015, *ApJ*, 799, 92
- Kamazaki, T., et al. 2012, *PASJ*, 64, 29
- Kaneko, H., Kuno, N., Iono, D., Tamura, Y., Tosaki, T., Nakanishi, K., & Sawada, T. 2013, *PASJ*, 65, 20
- Kautsch, S. J., Grebel, E. K., Barazza, F. D., & Gallagher III, J. S. 2006, *A&A*, 445, 765

- Kenney, J. D., & Young, J. S. 1988, *ApJS*, 66, 261
- Kennicutt, R. C., Jr., & Edgar, B. K. 1986, *ApJ*, 300, 132
- Kennicutt, R. C., Jr., & Evans II, N. J. 2012, *ARA&A*, 50, 531
- Kim, S. C., Park, H. S., Kyeong, J., Lee, J. H., Ree, C. H., & Kim, M. 2012, *PASJ*, 64, 23
- King, D., & Irwin, J. A. 1997, *New Astron.*, 2, 251
- Koda, J., et al. 2009, *ApJ*, 700, L132
- Koda, J., et al. 2012, *ApJ*, 761, 41
- Koda, J., Sofue, Y., Kohno, K., Nakanishi, H., Onodera, S., Okumura, S. K., & Irwin, J. A. 2002, *ApJ*, 573, 105
- Komugi, S., Sofue, Y., Kohno, K., Nakanishi, H., Onodera, S., Egusa, F., & Muraoka, K. 2008, *ApJS*, 178, 225
- Koopmann, R. A., Kenney, J. D. P., Young, J. 2001, *ApJS*, 135, 125
- Kregel, M., & Sancisi, R. 2001, *A&A*, 376, 59
- Krips, M. 2007, *A&A*, 464, 553
- Kroupa, P. 2001, *MNRAS*, 322, 231
- Kuno, N., et al. 2007, *PASJ*, 59, 117
- Kuno, N., et al. 2011, General Assembly and Scientific Symposium, XXXth URSI, JP2-19
- Kuno, N., & Nakai, N. 1997, *PASJ*, 49, 279
- Kuno, N., Tosaki, T., Nakai, N., & Nishiyama, K. 1997, *PASJ*, 49, 275
- Kuzio de Naray, R., Arsenault, C. A., Spekkens, K., Sellwood, J. A., McDonald, M., Simon, J. D., & Teuben, P. 2012, *MNRAS*, 427, 2523
- Laine, S., & Gottesman, S. T. 1998, *MNRAS*, 297, 1041
- Lelli, F., Verheijen, M., & Fraternali, F. 2014, *A&A*, 566, 71
- Leroy, A. K., et al. 2009, *AJ*, 137, 4670
- Leroy, A. K., et al. 2013, *AJ*, 146, 19
- Li, J. G., Seaquist, E. R., Wrobel, J. M., Wang, Z., & Sage, L. J. 1993, *ApJ*, 413, 150
- Li, W. D., Modjaz, M., Halderson, E., Shefler, T., King, J. Y., Treffers, R. R., Filippenko, A. V. 1998, *IAU Circ.*, 6978, 3
- Lindt-Krieg, E., Eckart, A., Neri, R., Krips, M., Pott, J. -U., Garcia-Burillo, S., & Combes, F. 2008, *A&A*, 479, 377
- Liu, J.-F., & Bregman, J. N. 2005, *ApJS*, 157, 59
- Lynds, B. T. 1980, *ApJ*, 238, 17
- Masters, K. L., et al. 2010, *MNRAS*, 405, 783
- Mathewson, D. S., Ford, V. L., & Buchhorn, M. 1992, *ApJS*, 81, 413
- Mei, S., et al. 2007, *ApJ*, 655, 144
- Meidt, S. E., et al. 2013, *ApJ*, 779, 45
- Minamidani, T., et al. 2016, *Proc. SPIE* 9914, Millimeter, Submillimeter, and Far-Infrared Detectors and Instrumentation for Astronomy VIII, 99141Z
- Minchin, R. F., et al. 2010, *AJ*, 140, 1093
- Miyamoto, Y., Seta, M., Nakai, N., Watanabe, Y., Salak, D., & Ishii, S. 2018, *PASJ*, 70, L1
- Momose, R., et al. 2013, *ApJ*, 772, L13
- Momose, R., Okumura, S. K., Koda, J., & Sawada, T. 2010, *ApJ*, 721, 383
- Monet, D. 1998, USNO-A2.0, U.S. Naval Observatory
- Morokuma-Matsui, K., & Baba, J. 2015, *MNRAS*, 454, 3792
- Morokuma-Matsui, K., Sorai, K., Watanabe, Y., & Kuno, N. 2015, *PASJ*, 67, 2
- Moshir, M., et al. 1990, *Infrared Astronomical Satellite Catalogs, The Faint Source Catalog, Version 2.0*
- Mühle, S., Klein, U., Wilcots, E. M., & Hüttemeister, S. 2005, *AJ*, 130, 524
- Mundell, C. G., Pedlar, A., Axon, D. J., Meaburn, J. & Unger, S. W. 1995, *MNRAS*, 277, 641
- Muñoz-Mateos, J. C., et al. 2013, *ApJ*, 771, 59
- Muraoka, K., et al. 2016, *PASJ*, 68, 89
- Muraoka, K., et al. 2019, *PASJ*, accepted
- Nagar, N. M., Falcke, H., Wilson, A. S., & Ulvestad, J. S. 2002, *A&A*, 392, 53
- Nakai, N., Kuno, N., Handa, T., & Sofue, Y. 1994, *PASJ*, 46, 527
- Nakanishi, H., et al. 2006, *ApJ*, 651, 804
- NEDTEAM 1992, Redshift obtained from Literature by the NED Team prior to November 1992
- NEDTEAM 2011, Computations for objects requiring measurements performed by NED team members
- NEDTEAM 2012, Computations for objects requiring measurements performed by NED team members
- Nilson, P. 1973, *Uppsala General Catalogue of Galaxies, Acta Universitatis Upsalienis, Nova Regiae Societatis Upsaliensis, Series V: A Vol. 1*
- Nishiyama, K., & Nakai, N. 2001, *PASJ*, 53, 713
- Nishiyama, K., Nakai, N., & Kuno, N. 2001, *PASJ*, 53, 757
- Oey, M. S., Parker, J. S., Mikles, V. J., & Zhang, X. 2003, *AJ*, 126, 2317
- Pan, H.-A., & Kuno, N. 2017, *ApJ*, 839, 133
- Paturel, G., Petit, C., Garnier, R., & Prugniel, P. 2000, *A&AS*, 475, 480
- Paturel, G., Petit, C., Prugniel, Ph., Theureau, G., Rousseau, J., Brouty, M., Dubois, P., Cambrésy, L. 2003, *A&A*, 412, 45
- Pejcha, O., & Prieto, J. L. 2015, *ApJ*, 799, 215
- Petrov, L., & Taylor, G. B. 2011, *AJ*, 142, 89
- Ponomareva, A. A., Verheijen, M. A. W., & Bosma, A. 2016, *MNRAS*, 463, 4052
- Popping, G., Caputi, K. I., Somerville, R. S., & Trager, S. C. 2012, *MNRAS*, 425, 2386
- Popping, G., et al. 2015, *MNRAS*, 454, 2258
- Poznanski, D., et al. 2009, *ApJ*, 694, 1067
- Querejeta, M., et al. 2015, *ApJS*, 215, 5
- Rahman, N., et al. 2012, *ApJ*, 745, 183
- Regan, M. W., Teuren, P. J., & Vogel, S. N. 1996, *AJ*, 112, 2549
- Richards, E. E., et al. 2016, *MNRAS*, 460, 689
- Riffel, R. A., Storchi-Bergmann, T. & Riffel, R. 2015, *MNRAS*, 451, 3587
- Rodríguez, Ó., Clocchiatti, A., & Hamuy, M. 2014, *AJ*, 148, 107
- Rodríguez-Rico, C. A., Viallefond, F., Zhao, J. -H., Goss, W. M., & Anantharamaiah, K. R. 2004, *ApJ*, 616, 783
- Rupen, M. P. 1991, *AJ*, 102, 48
- Saintonge, A., et al. 2011, *MNRAS*, 415, 32
- Saintonge, A., et al. 2013, *ApJ*, 778, 2
- Saintonge, A., et al. 2017, *ApJS*, 233, 22
- Sakamoto, K., Okumura, S. K., Ishizuki, S., & Scoville, N. Z. 1999, *ApJS*, 124, 403
- Sakamoto, S., Hasegawa, T., Handa, T., Hayashi, M., & Oka, T. 1997, *ApJ*, 486, 276

- Salak, D., et al. 2019, PASJ, accepted
- Salo, H., et al. 2015, ApJS, 219, 4
- Sawada, T., et al. 2008, PASJ, 60, 445
- Schinnerer, E., et al. 2013, ApJ, 779, 42
- Schmitt, H. R., Kinney, A. L., Storch-Bergmann, T., & Antonucci, R. 1997, ApJ, 477, 623
- Schruba, A., et al. 2011, AJ, 142, 37
- Shappee, B. J., et al. 2016, ApJ, 826, 144
- Sheth, K., et al. 2010, PASP, 122, 1397
- Sheth, K., Vogel, S. N., Regan, M. W., Thornley, M. D., & Teuben, P. J. 2005, ApJ, 632, 217
- Sil'chenko, O. K., & Afanasiev, V. L. 2006, Astron. Lett., 32, 534
- Sloan Digital Sky Survey Team 2004a, Sloan Digital Sky Survey Data Release 2 as obtained Nov. 18, 2004a from <http://www.sdss.org/dr2/products/spectra/getspectra.html>
- Sloan Digital Sky Survey Team 2004b, Sloan Digital Sky Survey Data Release 3 as obtained Sep. 28, 2004b from <http://www.sdss.org/dr3/products/spectra/getspectra.html>
- Sloan Digital Sky Survey Team 2005, Sloan Digital Sky Survey Data Release 4 as obtained Aug. 17, 2005 from <http://www.sdss.org/dr4/products/spectra/getspectra.html>
- Sloan Digital Sky Survey Team 2006, Sloan Digital Sky Survey Data Release 5 as obtained Jun. 28, 2006 from <http://www.sdss.org/dr5/products/catalogs/index.html>
- Sloan Digital Sky Survey Team 2007, Sloan Digital Sky Survey Data Release 6 as obtained Sep. 17, 2007 from <http://www.sdss.org/dr6/products/catalogs/index.html>
- Smith, B. J., & Wallin, J. F. 1992, ApJ, 393, 544
- Sofue, Y., Koda, J., Nakanishi, H., Onodera, S., Kohno, K., Tomita, A., & Okumura, S. K. 2003, PASJ, 55, 17
- Solomon, P. M., Downes, D., & Radford, J. E. 1992, ApJ, 398, L29
- Spinoso, D., Bonoli, S., Dotti, M., Mayer, L., Madau, P., & Bellovary, J. 2017, MNRAS, 465, 3729
- Springob, C. M., Haynes, M. P., Giovanelli, R., & Kent, B. R. 2005, ApJS, 160, 149
- Springob, C. M., Masters, K. L., Haynes, M. P., Giovanelli, R., & Marinoni, C. 2007, ApJS, 172, 599
- Springob, C. M., Masters, K. L., Haynes, M. P., Giovanelli, R., & Marinoni, C. 2009, ApJS, 182, 474
- Stil, J. M., Gray, A. D., & Harnett, J. I. 2005, ApJ, 625, 130
- Stil, J. M., & Israel, F. P. 2002, A&A, 392, 473
- Stone, R. C., Pier, J. R., & Monet, D. G. 1999, AJ, 118, 2488
- Sun, J., et al. 2018, ApJ, 860, 172
- Tamburro, D., Rix, H. -W., Walter, F., Brinks, E., de Blok, W. J. G., Kennicutt, R. C., & Mac Low, M. -M. 2008, AJ, 136, 2872
- Taniguchi, Y., & Ohyama, Y. 1998, ApJ, 507, L121
- Taniguchi, Y., Ohyama, Y., & Sanders, D. B. 1999, ApJ, 522, 214
- Terry, J. N., Paturel, G., & Ekholm, T. 2002, A&A, 393, 57
- Theureau, G., Bottinelli, L., Coudreau-Durand, N., Gouguenheim, L., Hallet, N., Loulergue, M., Paturel, G., & Teerikorpi, P. 1998, A&AS, 130, 333
- Theureau, G., Hanski, M. O., Coudreau, N., Hallet, N., & Martin, J. -M. 2007, A&A, 465, 71
- Thilker, D. A., Walterbos, R. A. M., Braun, R., & Hoopes, C. G. 2002, AJ, 124, 3118
- Toloba, E., et al. 2014, ApJS, 215, 17
- Torres-Flores, S., Amram, P., Mendes de Oliveira, C., Plana, H., Balkowski, C., Marcelin, M., & Olave-Rojas, D. 2014, MNRAS, 442, 2188
- Tosaki, T., et al. 2011, PASJ, 63, 1171
- Trentham, N., & Hodgkin, S. 2002, MNRAS, 333, 423
- Tully, R. B. 1988, Nearby Galaxy Catalogue (Cambridge: Cambridge University Press)
- Tully, R. B., et al. 2013, AJ, 146, 86
- Tully, R. B., Rizzi, L., Shaya, E. J., Courtois, H. M., Makarov, D. I., & Jacobs, B. A. 2009, AJ, 138, 323
- Two Micron All Sky Survey Team 2000, 2MASS Point Source Catalog. Release 2
- Two Micron All Sky Survey Team 2003, 2MASS Extended objects. Final release
- Ulvestad, J. S., & Wilson, A. S. 1984, ApJ, 285, 439
- Vaduvescu, O., & McCall, M. L. 2008, A&A, 487, 147
- van den Bergh, S. 1976, ApJ, 206, 883
- van Driel, W., & Buta, R. J. 1991, A&A, 245, 7
- van Eymeren, J., Jütte, E., Jog, C. J., Stein, Y., & Dettmar, R. -J. 2011, A&A, 530, 29
- Viallefond, F., Allen, R. J., & de Boer, J. A. 1980, A&A, 82, 207
- Vigott, M., Grueff, G., Perley, R., Clark, B. G., & Bridle, A. H. 1989, AJ, 98, 419
- Villanueva, V., et al. 2017, MNRAS, 470, 3775
- Villi, M., Nakano, S., Aoki, M., Skiff, B. A., & Hanzl, D. 1998, IAU Circ., 6899, 1
- Walter, F., Brinks, E., de Blok, W. J. G., Bigiel, F., Kennicutt, Jr., R. C., Thornley, M. D., & Leroy, A. 2008, AJ, 136, 2563
- Walter, F., Dahlem, M., & Lisenfeld, U. 2004, ApJ, 606, 258
- Walter, F., Weiss, A., Martin, C., & Scoville, N. 2002, AJ, 123, 225
- Wang, Z., et al. 2004, ApJS, 154, 193
- Watanabe, Y., Sorai, K., Kuno, N., & Habe, A. 2011, MNRAS, 411, 1409
- Wen, X. -Q., Wu, H., Z., Y. -N., Lam, M. I., Wu, C. -J., Wicker, J., & Zhao, Y. -H. 2013, MNRAS, 433, 2946
- Weyant, A., Michael Wood-Vasey, W., Allen, L., Garnavich, P. M., Jha, S. W., Joyce, R., & Matheson, T. 2014, ApJ, 784, 105
- Whiting, A. B., Hau, G. K. T., Irwin, M., & Verdugo, M. 2007, AJ, 133, 715
- Wilson, C. D., et al. 2012, MNRAS, 424, 3050
- Wright, E. L., et al. 2010, AJ, 140, 1868
- XMM-Newton Survey Science Centre Consortium 2010, The XMM-Newton Serendipitous Source Catalogue. 2XMM v1.2 Downloaded from <http://xmmssc-www.star.le.ac.uk> on 1/11/2012
- Yajima, Y., et al. 2019, PASJ, accepted
- Yamamura, I., Makiuti, S., Ikeda, N., Fukuda, Y., Oyabu, S., Koga, T., & White, G. J. 2010, AKARI/FIS All-Sky Survey Point Source Catalogues (ISAS/JAXA)
- Yamauchi, A., Nakai, N., Sato, N., & Diamond, P. 2004, PASJ, 56, 605

- Young, J. S., et al. 1995, *ApJS*, 98, 219
- Young, J. S., & Scoville, N. Z. 1991, *ARA&A*, 29, 581
- Young, L. M., Rosolowsky, E., van Gorkom, J. H., & Lamb, S. A. 2006, *ApJ*, 650, 166
- Zahid, H. J., Dima, G. I., Kewley, L. J., Erb, D. K., & Davé, R. 2012, *ApJ*, 757, 54
- Zschaechner, L. K., Rand, R. J., & Walterbos, R. 2015, *ApJ*, 799, 61

Table 1. Galaxy parameters of the targets.

Galaxy	PGC	Morphology	D_{25} ($'$)	Distance (Mpc)		PA ($^{\circ}$)	i ($^{\circ}$)	Notes		S_{100} (Jy)	S_{140} (Jy)	
(1)	(2)	(3)	(4)	(5)	(6)	(7)	(8)	(9)	(10)	(11)	(12)	(13)
isolated galaxies												
IC 10	1305	IBm	6.31		0.74	17	132.0	52	26	24	71.25	33.0
NGC 150	2052	SB(rs)b?	3.89		24.20	17	108.9	59.3	46	‡	17.85	16.3
NGC 157	2081	SAB(rs)bc	4.17		12.10	17	-136.0	48.0	46	‡	37.73	25.2
NGC 278	3051	SAB(rs)b	2.09		15.9	2	52	21	14	‡	45.19	32.3
NGC 337	3572	SB(s)d	2.88		18.90	17	119.6	44.5	46		17.34	15.0
NGC 470	4777	SA(rs)b	2.82		41.30	17	155.4	58.0	46	‡	12.24	13.5
NGC 520	5193	pec	4.47		8.02	1	130.0	60	26 †	‡	48.40	33.8
NGC 613	5849	SB(rs)bc	5.50		26.4	18	-54.1	38.8			49.14	34.9
NGC 628	5974	SA(s)c	10.47		9.020	4	20	7	53	60	11.97	
NGC 660	6318	SB(s)a pec	8.32		13.60	17	-138.5	72	26 †	‡	103.74	76.4
NGC 701	6826	SB(rs)c	2.45		20.80	17	44.7	58.6	46	‡	13.77	14.0
NGC 891	9031	SA(s)b? edge-on	13.49		9.12	17	-157.0	88.6	45		147.93	54.2
NGC 1022	10010	(R ⁺)SB(s)a	2.40		18.5	19	85.0	30	26 †	§	27.44	20.6
NGC 1055	10208	SBb? edge-on	7.59		20.30	17	102.5	61	26 †	‡	60.44	45.0
NGC 1084	10464	SA(s)c	3.24		20.90	17	-141.6	57.2	46	‡	55.04	44.5
NGC 1087	10496	SAB(rs)c	3.72		14.90	17	1.4	50.5	46	‡	29.55	23.2
NGC 1156	11329	IB(s)m	3.31		7.6	6	-88.12	52.11	58		10.56	
NGC 1241	11887	SB(rs)b	2.82		61.40	17	-45	52	26 †	12	10.21	10.9
UGC 2765	13121	S0/a	3.98	2	19.5	16	150.0	57	26 †	‡	12.05	13.2
NGC 1482	14084	SA0 ⁺ pec edge-on	2.45		19.6	19	-61.5	55.2	46	‡	46.52	37.9
UGCA 86	14241	Im?	0.79		2.98	17	-73	45	51		11.90	
IC 356	14508	SA(s)ab pec	5.25		21.6	18	105.0	43	26	‡	24.44	10.1
NGC 1530	15018	SB(rs)b	4.57		20.40	17	-172	45	41	‡	24.17	19.2
NGC 1569	15345	IBm	3.63		3.25	17	112	63	37, 52		51.71	24.7
NGC 2146	18797	SB(s)ab pec	6.03		27.7	15	-43.5	62	26 †	‡	187.36	140.9
NGC 2273	19688	SB(r)a?	3.24		31.6	15	51	53	57		10.27	
NGC 2339	20222	SAB(rs)bc	2.69		36.60	17	174	44	50	‡	32.24	30.3
NGC 2268	20458	SAB(r)bc	3.24		30.60	17	-112	58	50	7	14.53	13.8
NGC 2276	21039	SAB(rs)c	2.82		36.8	19	-113	48	15		29.50	19.9
NGC 2633	24723	SB(s)b	2.45		29.10	17	-176.3	50.1	46	‡	27.01	22.9
NGC 2681	24961	(R ⁺)SAB0/a(rs)	3.63		16.40	17	116.6	11.2	46	‡	11.37	
NGC 2742	25640	SA(s)c?	3.02		27.8	12	-93.5	59.9	46	‡	10.57	11.5
NGC 2715	25676	SAB(rs)c	4.90		17.50	17	-159.1	67.8	46	‡		11.0
NGC 2775	25861	SA(r)ab	4.27		17.0	19	163.5	35.4	46	14	10.47	10.6
NGC 2748	26018	SABc	3.02		19.80	17	-138.8	72.8	46	‡	19.46	15.8
NGC 2782	26034	SAB(rs)a pec	3.47		15.7	16	-105	30	23		13.81	12.1
NGC 2841	26512	SA(r)b?	8.13		14.60	17	152.6	73.7	10		14.00	
NGC 2903	27077	SAB(rs)bc	12.59		9.46	17	-155	67	31		104.08	62.1
NGC 2967	27723	SA(s)c	3.02		22.2	2	64.0	16.5	46		15.08	15.3
NGC 2976	28120	SAC pec	5.89		3.63	17	-25.5	64.5	10		29.71	16.0
NGC 2985	28316	(R ⁺)SA(rs)ab	4.57		22.4	19	-3	40	19		19.49	16.5
NGC 3034	28655	I0 edge-on	11.22		3.53	17	68	81	44		1144.97	1053
NGC 3079	29050	SB(s)c edge-on	7.94		20.60	17	169	79	29		88.95	70.2
NGC 3077	29146	I0 pec	5.37		3.81	17	63.8	38.9	46	62	25.11	15.8
NGC 3166	29814	SAB0/a(rs)	4.79		22.0	19	-100.4	55.7	46	48	13.48	11.7

Table 1. (Continued)

Galaxy	PGC	Morphology	D_{25}		Distance		PA	i	Notes		S_{100}	S_{140}
(1)	(2)	(3)	(4)	(5)	(6)	(7)	(8)	(9)	(10)	(11)	(12)	(13)
NGC 3169	29855	SA(s)a pec	4.37		23.20	17	-123.7	39.0	46	‡	19.94	18.8
NGC 3177	30010	SA(rs)b	1.45		24.1	16	-42.5	28.8	46	‡	18.01	15.8
NGC 3147	30019	SA(rs)bc	3.89		39.30	17	142.79	35.19	58		24.63	22.8
NGC 3198	30197	SB(rs)c	8.51		13.40	17	-145.0	71.5	10		14.84	11.5
Mrk 33	31141	Im pec?	1.00		24.9	19	124.0	42.6	46	6		
NGC 3310	31650	SAB(r)bc pec	3.09		11.6	1	150	56	30		41.76	28.1
NGC 3338	31883	SA(s)c	5.89		23.70	17	97.1	60.9	46	‡	10.11	
NGC 3344	31968	(R)SAB(r)bc	7.08		9.82	17	-37.3	27.0	46	‡	20.72	
NGC 3351	32007	SB(r)b	7.41		10.7	12	-168	41	53	60	35.30	27.7
NGC 3367	32178	SB(rs)c	2.51		30.8	1	51	30	2		13.01	12.4
NGC 3359	32183	SB(rs)c	7.24		20.80	17	-8	51	4		14.32	10.5
NGC 3368	32192	SAB(rs)ab	7.59		9.900	20	169.0	57.5	21		27.44	20.5
NGC 3370	32207	SA(s)c	3.16		25.60	5	-38.1	55.1	46	40		12.0
NGC 3437	32648	SAB(rs)c?	2.51		25.10	17	-61.5	65.9	46	‡	20.64	18.7
NGC 3471	33074	Sa	1.74		24.2	18	10.5	48.6	46	‡	12.23	10.3
NGC 3521	33550	SAB(rs)bc	10.96		14.20	17	-19	63	31		85.05	65.2
NGC 3556	34030	SB(s)cd edge-on	8.71		10.00	17	-102.2	78.3	28		61.31	26.4
NGC 3583	34232	SB(s)b	2.82		27.9	16	131.3	38.6	46	‡	17.98	17.8
NGC 3627	34695	SAB(s)b	9.12		9.04	17	176	52	31		105.60	
NGC 3628	34697	Sb pec edge-on	14.79		10.30	17	102.4	87	25		103.12	57.8
NGC 3655	34935	SA(s)c?	1.55		38.40	17	-100.3	23.5	46	‡	19.10	17.5
NGC 3672	35088	SA(s)c	4.17		27.40	17	7.8	67.2	46	‡	22.70	21.5
NGC 3675	35164	SA(s)b	5.89		19.60	17	176	67.8	42		35.20	33.8
NGC 3686	35268	SB(s)bc	3.24		15.9	18	19.5	35.2	46	‡	11.72	10.8
NGC 3810	36243	SA(rs)c	4.27		16.40	17	-154.3	42.2	46	‡	31.40	26.3
NGC 3813	36266	SA(rs)b?	2.24		23.30	17	83.1	68.2	46	‡		20.3
NGC 3888	36789	SAB(rs)c	1.74		39.7	16	121.2	41.8	46	‡	11.39	11.0
NGC 3893	36875	SAB(rs)c?	4.47		15.7	14	-13	30	19		35.07	27.3
NGC 3938	37229	SA(s)c	5.37		17.9	11	-154.0	20.9	46	‡	22.18	14.2
NGC 3949	37290	SA(s)bc?	2.88		19.10	17	-58.2	52.9	46	‡	25.23	19.9
UGC 6973	37719	Sab? edge-on	2.63		23.4	18	39.0	64.8	46	‡		40.0
NGC 4027	37773	SB(s)dm	3.16		19.6	10	-9.2	35.9	46	‡	28.04	26.2
NGC 4030	37845	SA(s)bc	4.17		29.90	17	29.6	39.0	46	‡	46.34	51.3
NGC 4041	37999	SA(rs)bc?	2.69		30.2	2	-138.7	23.4	46	‡	31.49	29.8
NGC 4045	38031	SAB(r)a	2.69		33.70	17	-92.1	48.4	46	‡	13.80	16.6
NGC 4085	38283	SAB(s)c?	2.82		20.80	17	-104.7	75.0	46	‡	14.74	14.1
NGC 4088	38302	SAB(rs)bc	5.75		14.50	17	-126.8	68.9	46	‡	51.72	42.8
NGC 4214	39225	IAB(s)m	8.51		2.93	17	65	30	34		25.47	14.1
NGC 4258	39600	SAB(s)bc	18.62		7.31	17	-29	72	40			23.8
NGC 4303	40001	SAB(rs)bc	6.46		16.5	8	-36.4	27.0	46	‡	61.69	39.8
NGC 4433	40894	SAB(s)ab	2.19		44.10	17	5	64	11 †	‡	25.88	22.6
NGC 4527	41789	SAB(s)bc	6.17		16.5	8	69.5	70	26	‡	63.52	43.5
NGC 4536	41823	SAB(rs)bc	7.59		16.5	8	-54.5	64.2	46	‡	44.98	35.9
NGC 4559	42002	SAB(rs)cd	10.72		7.31	17	-36.8	63.1	46	14	18.01	11.6
NGC 4579	42168	SAB(rs)b	5.89		16.5	8	92.1	41.7	46	‡	17.91	11.0
NGC 4605	42408	SB(s)c pec	5.75		5.55	17	-67	69	40		30.53	15.6

Table 1. (Continued)

Galaxy	PGC	Morphology	D_{25}		Distance		PA	i	Notes		S_{100}	S_{140}
(1)	(2)	(3)	(4)	(5)	(6)	(7)	(8)	(9)	(10)	(11)	(12)	(13)
NGC 4602	42476	SAB(rs)bc	3.39		37.80	17	100.7	67.9	46	‡	13.63	11.4
NGC 4632	42689	SAC	3.09		14.40	17	60.5	65.9	46	‡	10.84	10.6
NGC 4666	42975	SABc?	4.57		14.70	13	-135	70	61		77.14	58.2
NGC 4750	43426	(R)SA(rs)ab	2.04		26.1	19	-50.0	40	26 †	‡	14.48	13.3
NGC 4753	43671	I0	6.03		24.5	3	82.2	57.2	46	1		10.3
NGC 4818	44191	SAB(rs)ab pec?	4.27		11.90	17	-175.5	67.2	46	‡	26.55	24.1
NGC 5005	45749	SAB(rs)bc	5.75		18.00	17	67.0	66.7	46	‡	59.38	45.7
NGC 5055	46153	SA(rs)bc	12.59		9.04	17	98	61	31		101.24	46.2
NGC 5248	48130	SAB(rs)bc	6.17		13.00	17	103.9	38.6	46	‡	43.97	33.6
NGC 5364	49555	SA(rs)bc pec	6.76		18.2	16	-144.4	47.9	46	‡	11.42	
NGC 5480	50312	SA(s)c?	1.74		30.6	16	37.2	37.5	46	‡	10.13	10.6
NGC 5678	51932	SAB(rs)b	3.31		35.70	17	-177.5	56.9	46	‡	25.42	22.8
NGC 5665	51953	SAB(rs)c pec?	1.91		18.20	17	154.7	51.7	46	‡	13.03	12.3
NGC 5676	51978	SA(rs)bc	3.98		34.70	17	-131.9	59.8	46	‡	30.61	30.8
NGC 5713	52412	SAB(rs)bc pec	2.75		19.5	7	-157	33	9		37.22	34.7
NGC 5792	53499	SB(rs)b	6.92		26.40	17	-98.5	64	26 †	‡	19.30	17.8
NGC 5907	54470	SA(s)c? edge-on	12.59		17.10	17	-24	86.5	18		36.01	25.8
NGC 6015	56219	SA(s)cd	5.37		19.00	17	-150	62	15		10.80	12.3
NGC 6503	60921	SA(s)cd	7.08		6.25	17	-60.2	73.5	32		25.39	20.5
NGC 6574	61536	SAB(rs)bc?	1.41		41.90	17	165	45	36		27.82	29.4
NGC 6643	61742	SA(rs)c	3.80		21.30	17	37	60	19		31.78	29.9
NGC 6764	62806	SB(s)bc	2.29		23.70	17	75	68	55 †	22	11.90	
NGC 6951	65086	SAB(rs)bc	3.89		23.30	20	135	30	31		37.14	25.3
NGC 7331	69327	SA(s)b	10.47		13.90	17	167.7	75.8			82.19	69.2
NGC 7448	70213	SA(rs)bc	2.69		28.20	17	-10.6	62.9	46	‡	18.14	14.9
NGC 7479	70419	SB(s)c	4.07		36.80	17	-158	51	33		24.93	17.2
NGC 7541	70795	SB(rs)bc? pec	3.47		32.10	17	99.0	72.8	46	‡	39.93	35.6
NGC 7625	71133	SA(rs)a pec	1.58		23.0	19	-151.4	37.4	35		18.85	19.4
NGC 7721	72001	SA(s)c	3.55		28.00	20	-164.2	69.8	46	‡	12.03	12.9
NGC 7798	73163	SBc	1.38	1	32.6	19	70.5	31.9	46	‡	10.03	
interacting galaxies												
NGC 772 / NGC 770					32.2	9						
NGC 770	7517	E3?	1.17		32.2	9	-165	44	11 †	20		
NGC 772	7525	SA(s)b	7.24		32.2	9	-45.0	37	26 †	20	21.66	20.7
NGC 2207 / IC 2163					38.1	9						
NGC 2207	18749	SAB(rs)bc pec	4.27		38.1	9	-40	35	13		24.38	18.1
IC 2163	18751	SB(rs)c pec	3.02		38.1	9	65	40	13			
Arp 283					29.6	9						
NGC 2798	26232	SB(s)a pec	2.57		29.6	9	158.7	60.7	46	9	29.13 ‡	21.3 ‡
NGC 2799	26238	SB(s)m?	1.86		29.6	9	125	75	11 †	9	29.13 ‡	21.3 ‡
Arp 245					29.0	*						
NGC 2992	27982	Sa pec	3.55		29.0	16	-157.5	65	26 †	16	14.44	13.2
NGC 2993	27991	Sa pec	1.35		29.0	*	-20.0	20	55 †	§	15.51	12.3
Arp 094					19.6	9						
NGC 3226	30440	E2? pec	3.16		19.6	9	25.0	37	26 †	§		
NGC 3227	30445	SAB(s)a pec	5.37		19.6	9	158	56	38		17.46	17.2

Table 1. (Continued)

Galaxy	PGC	Morphology	D_{25}		Distance		PA	i	Notes		S_{100}	S_{140}
(1)	(2)	(3)	(4)	(5)	(6)	(7)	(8)	(9)	(10)	(11)	(12)	(13)
NGC 4298 / NGC 4302					16.5	8						
NGC 4298	39950	SA(rs)c	3.24		16.5	8	-48.9	54.8	46	8	19.71	12.0
NGC 4302	39974	Sc? edge-on	5.50		16.5	8	180	90	64			12.8
NGC 4383 / UGC 7504					16.5	8						
UGC 7504	40506	dIrr	1.00	3, 4	16.5	8	168	73	39 †	54		
NGC 4383	40516	Sa? pec	1.95		16.5	8	-171.7	44.4	46	8	12.40	
Arp 269					4.60	9						
NGC 4485	41326	IB(s)m pec	2.29		4.60	9	-14.3	44.6	46	59		
NGC 4490	41333	SB(s)d pec	6.31		4.60	9	115.0	65	26 †	‡	77.96	34.1
VV 219					16.5	8						
NGC 4567	42064	SA(rs)bc	2.95		16.5	8	80	46	27		47.59 ‡	46.2 ‡
NGC 4568	42069	SA(rs)bc	4.57		16.5	8	23	64	27		47.59 ‡	46.2 ‡
Arp 116					16.5	8						
NGC 4647	42816	SAB(rs)c	2.88		16.5	8	98.5	39.3	63		15.77	16.4
NGC 4649	42831	E2	7.41		16.5	8	-72.5	35.9	26	3		
Arp 271					40.0	9						
NGC 5426	50083	SA(s)c pec	2.95		40.0	9	177.5	59	17		16.46 ‡	
NGC 5427	50084	SA(s)c pec	2.82		40.0	9	53.2	34	17		16.46 ‡	14.7
Arp 090					42.5	9						
NGC 5929	55076	Sab? pec	0.95		42.5	9	62	26	47, 56	43	13.74 ‡	13.0 ‡
NGC 5930	55080	SAB(rs)b pec	1.58		42.5	9	-25.0	45.0	5		13.74 ‡	13.0 ‡
Arp 284					38.6	9						
NGC 7714	71868	SB(s)b? pec	1.91		38.6	9	-42	30	49		11.29 ‡	
NGC 7715	71878	Im pec edge-on	2.57		38.6	9	73	79	11 †	§	11.29 ‡	

Notes.

Column (1): Galaxy name. Indented pairs are observed as a pair galaxy listed just above the line. Two galaxy names are listed with “/” if no commonly used name is provided.

Column (2): PGC number.

Column (3): Morphology.

Column (4): Optical diameter (D_{25}) in arcmin.

Column (5): Reference of morphology and D_{25} . No remark means RC3 (de Vaucouleurs et al. 1991). (1) Huchra et al. 1999 (morphology). (2) NED (morphology). (3) Nilson 1973 (D_{25}). (4) Trentham & Hodgkin 2002 (morphology).

Column (6): Distance of galaxies in Mpc. The distances of the galaxies identified as members of the Virgo cluster are adopted as the same value of 16.5 Mpc. The distances of the interacting galaxies are considered similar to each other.

Column (7): Reference of distance. (1) Bottinelli et al. 1984a. (2) Bottinelli et al. 1984b. (3) Caso et al. 2015. (4) Dhungana et al. 2016. (5) Fiorentino et al. 2013. (6) Kim et al. 2012. (7) Mathewson et al. 1992. (8) Mei et al. 2007. (9) NED (Hubble flow distance of double galaxy). (10) Pejcha, & Prieto 2015. (11) Poznanski et al. 2009. (12) Rodríguez et al. 2014. (13) Shappee et al. 2016. (14) Springob et al. 2009. (15) Terry et al. 2002. (16) Theureau et al. 2007. (17) Tully et al. 2013. (18) Tully et al. 2009. (19) Tully 1988. (20) Weyant et al. 2014. *: No data. Then the distance of NGC 2992 is adopted.

Column (8): Position angle (PA) of the major axis of the galaxies in -180° to $+180^\circ$. The angle is the PA of the receding side if we can judge. The north is 0° , and a positive value corresponds to the eastern side.

Column (9): Inclination of galaxy discs. The face-on disc is 0° . This value corresponds to the angle of $\arccos(b/a)$, except for the galaxy discs. Here, a and b are the semi-major and -minor axes of the galaxy, respectively.

Column (10): Reference and notes of position angle (PA) and inclination (i). †: We refer the value shown in NED.

Column (11): Reference for judging the receding side of the PA. ‡: Judging the receding side from our velocity field map. §: The ambiguity of 180° for the PA is unresolved because of missing kinematical information. ||: No kinematical information.

According to our velocity field and a following paper (Salak et al. 2019), the PA and i seem to be incorrect at least for our mapping area. (1) Alatalo et al. 2013. (2) Antonio García-Barreto & Rosado 2001. (3) Arnold et al. 2014. (4) Ball et al. 1986. (5) Bolatto et al. 2017. (6) Bravo-Alfaro et al. 2004. (7) Broeils & van Woerden 1994. (8) Chung et al. 2009a. (9) Daigle et al. 2006. (10) de Blok et al. 2008. (11) de Vaucouleurs et al. 1991. (12) Díaz et al. 2003. (13) Elmegreen et al. 1995. (14) Epinat et al. 2008a. (15) Epinat et al. 2008b. (16) Friedrich et al. 2010. (17) Fuentes-Carrera et al. 2004. (18) García-Burillo et al. 1997. (19) Garrido et al. 2002. (20) Geha et al. 2005. (21) Haan et al. 2008. (22) Hota & Saikia 2006. (23) Hunt et al. 2008. (24) Hunter et al. 2012. (25) Irwin & Sofue 1996. (26) Jarrett et al. 2003. (27) Kenney & Young 1988. (28) King & Irwin 1997. (29) Koda et al. 2002. (30) Kregel & Sancisi 2001. (31) Kuno et al. 2007. (32) Kuzio de Naray et al. 2012. (33) Laine & Gottesman 1998. (34) Lelli et al. 2014. (35) Li et al. 1993. (36) Lindt-Krieg et al. 2008. (37) Mühle et al. 2005. (38) Mundell et al. 1995. (39) Nilson 1973. (40) Ponomareva et al. 2016. (41) Regan et al. 1996. (42) Richards et al. 2016. (43) Riffel et al. 2015. (44) Rodriguez-Rico et al. 2004. (45) Rupen 1991. (46) Salo et al. 2015. (47) Schmitt et al. 1997. (48) Sil'chenko & Afanasiev 2006. (49) Smith & Wallin 1992. (50) Springob et al. 2007. (51) Stil et al. 2005. (52) Stil & Israel 2002. (53) Tamburro et al. 2008. (54) Toloba et al. 2014. (55) Two Micron All Sky Survey Team 2003. (56) Ulvestad & Wilson 1984. (57) van Driel & Buta 1991. (58) van Eymeren et al. 2011. (59) Viallefond et al. 1980. (60) Walter et al. 2008. (61) Walter et al. 2004. (62) Walter et al. 2002. (63) Young et al. 2006. (64) Zschaechner et al. 2015.

Column (12), (13): FIR flux in Jy for IRAS 100 μm and AKARI 140 μm . ‡: Unresolved in FIR observation.

Table 2. Observation periods and system noise temperatures.

Season	Date	Typical T_{sys} (K)	
		^{12}CO	^{13}CO & C^{18}O
1	2015 Apr. 4 – 2015 May 6	560	300
2	2015 Dec. 21 – 2016 May 24	340	170
3	2016 Nov. 28 – 2017 March 17	360	180
4	2017 Dec. 24 – 2018 Apr. 23	390	180

Table 3. Sample observational parameters.

Galaxy	$\alpha_{J2000.0}$	$\delta_{J2000.0}$		Mapping size	PA of +X	$V_{LSR}(\text{km s}^{-1})$		Season	
(1)	(2)	(3)	(4)	(5)	(6)	(7)	(8)	(9)	(10)
isolated galaxies									
IC 10	00 ^h 20 ^m 17 ^s .34	+59°18'13".6		366" × 330"	125°	14	-340	3	2
NGC 150	00 ^h 34 ^m 15 ^s .48	-27°48'12".9		234" × 138"	118°		1569		3
NGC 157	00 ^h 34 ^m 46 ^s .76	-08°23'47".2		198" × 150"	30°		1655		2
NGC 278	00 ^h 52 ^m 04 ^s .31	+47°33'01".8		186" × 186"	116°	10	644	3	2
NGC 337	00 ^h 59 ^m 50 ^s .09	-07°34'40".7		186" × 150"	130°		1649	9	3
NGC 470	01 ^h 19 ^m 44 ^s .85	+03°24'35".8		198" × 150"	155°		2350		2
NGC 520	01 ^h 24 ^m 35 ^s .07	+03°47'32".7		258" × 150"	130°		2195		2
NGC 613	01 ^h 34 ^m 18 ^s .170	-29°25'06".10	14	282" × 246"	120°		1457		4
NGC 628	01 ^h 36 ^m 41 ^s .747	+15°47'01".18	8	366" × 366"	25°	15	654	3	3
NGC 660	01 ^h 43 ^m 02 ^s .400	+13°38'42".20	22	366" × 162"	170°		845	3	2
NGC 701	01 ^h 51 ^m 03 ^s .84	-09°42'09".4		186" × 126"	40°		1815		3
NGC 891	02 ^h 22 ^m 33 ^s .41	+42°20'56".9	29	582" × 198"	22°		527		3
NGC 1022	02 ^h 38 ^m 32 ^s .705	-06°40'38".74	28	174" × 162"	115°		1434	7	3
NGC 1055	02 ^h 41 ^m 45 ^s .23	+00°26'35".4		366" × 210"	105°		982		3, 4
NGC 1084	02 ^h 45 ^m 59 ^s .908	-07°34'42".48	26	210" × 138"	35°		1387		3
NGC 1087	02 ^h 46 ^m 25 ^s .164	-00°29'55".14	26	222" × 150"	5°		1500		3
NGC 1156	02 ^h 59 ^m 42 ^s .300	+25°14'16".20	15	210" × 186"	25°		375		4
NGC 1241	03 ^h 11 ^m 14 ^s .64	-08°55'19".7		222" × 174"	140°		3963		4
UGC 2765	03 ^h 32 ^m 03 ^s .41	+68°22'06".2		222" × 138"	165°		1674		3
NGC 1482	03 ^h 54 ^m 38 ^s .965	-20°30'09".65	32	150" × 114"	103°		1738	##	3
UGCA 86	03 ^h 59 ^m 48 ^s .30	+67°08'18".6	31	114" × 102"	25°	1	70		2
IC 356	04 ^h 07 ^m 46 ^s .91	+69°48'44".8		306" × 246"	90°		890		3
NGC 1530	04 ^h 23 ^m 27 ^s .10	+75°17'44".1		270" × 186"	130°	4	2447		3
NGC 1569	04 ^h 30 ^m 49 ^s .059	+64°50'52".60	5	198" × 138"	120°		-87		2
NGC 2146	06 ^h 18 ^m 37 ^s .71	+78°21'25".3		294" × 258"	56°		897		2
NGC 2273	06 ^h 50 ^m 08 ^s .6575	+60°50'44".901	1	210" × 162"	50°		1829		3
NGC 2339	07 ^h 08 ^m 20 ^s .54	+18°46'48".9		174" × 150"	175°		2177		2
NGC 2268	07 ^h 14 ^m 17 ^s .44	+84°22'56".2	*	270" × 270"	90°		2214		3
NGC 2276	07 ^h 27 ^m 14 ^s .36	+85°45'16".4	†	222" × 222"	90°		2406		3
NGC 2633	08 ^h 48 ^m 04 ^s .58	+74°05'55".9		186" × 138"	175°		2151		2
NGC 2681	08 ^h 53 ^m 32 ^s .740	+51°18'49".22	8	222" × 222"	107°	9	690		3
NGC 2742	09 ^h 07 ^m 33 ^s .53	+60°28'45".6		198" × 138"	87°		1285		3
NGC 2715	09 ^h 08 ^m 06 ^s .20	+78°05'06".6		258" × 138"	22°		1324		3
NGC 2775	09 ^h 10 ^m 20 ^s .12	+07°02'16".6	‡	258" × 222"	155°		1337		3
NGC 2748	09 ^h 13 ^m 43 ^s .02	+76°28'31".2		186" × 114"	38°		1466	6	3
NGC 2782	09 ^h 14 ^m 05 ^s .1124	+40°06'49".316	12	234" × 198"	108°	9	2538		4
NGC 2841	09 ^h 22 ^m 02 ^s .634	+50°58'35".47	16	342" × 210"	154°	8	637		2
NGC 2903	09 ^h 32 ^m 10 ^s .11	+21°30'03".0		558" × 306"	25°	7	549	4 ***	1
NGC 2967	09 ^h 42 ^m 03 ^s .295	+00°20'11".18	26	186" × 186"	65°		1870		3
NGC 2976	09 ^h 47 ^m 15 ^s .46	+67°54'59".0		390" × 246"	143°		9		1
NGC 2985	09 ^h 50 ^m 22 ^s .23	+72°16'43".1		234" × 198"	180°		1323		3
NGC 3034	09 ^h 55 ^m 52 ^s .725	+69°40'45".78	10	558" × 306"	65°	15	209		3, 4
NGC 3079	10 ^h 01 ^m 57 ^s .8034	+55°40'47".242	21 §	306" × 246"	169°	5	1142	10 ***	1
NGC 3077	10 ^h 03 ^m 19 ^s .07	+68°44'02".1		294" × 246"	45°		20		2
NGC 3166	10 ^h 13 ^m 45 ^s .778	+03°25'29".89	26	258" × 186"	87°		1332		3
NGC 3169	10 ^h 14 ^m 15 ^s .0502	+03°27'57".875	1	282" × 186"	45°		1221		3

Table 3. (Continued)

Galaxy	$\alpha_{J2000.0}$	$\delta_{J2000.0}$	Mapping size	PA of +X	V_{LSR} (km s ⁻¹)	Season			
(1)	(2)	(3)	(4)	(5)	(6) (7)	(8) (9) (10)			
NGC 3177	10 ^h 16 ^m 34 ^s .136	+21°07'22".99	26	138" × 126"	135°	1293	3		
NGC 3147	10 ^h 16 ^m 53 ^s .6509	+73°24'02".695	17 ‡	246" × 222"	155°	2801	2		
NGC 3198	10 ^h 19 ^m 54 ^s .952	+45°32'58".64	8	438" × 222"	35°	8	663	2	
Mrk 33	10 ^h 32 ^m 31 ^s .997	+54°24'02".05	8	114" × 114"	138°	12	1458	3	
NGC 3310	10 ^h 38 ^m 45 ^s .860	+53°30'12".18	26	222" × 210"	10°	13	981	2	
NGC 3338	10 ^h 42 ^m 07 ^s .540	+13°44'49".20	25	306" × 198"	100°		1292	3	
NGC 3344	10 ^h 43 ^m 31 ^s .15	+24°55'20".0		354" × 330"	150°	4	584	3	
NGC 3351	10 ^h 43 ^m 57 ^s .700	+11°42'13".70	24	378" × 258"	13°	15	772	3	
NGC 3367	10 ^h 46 ^m 34 ^s .954	+13°45'03".09	26	162" × 162"	70°	13	3008	3	
NGC 3359	10 ^h 46 ^m 36 ^s .863	+63°13'27".25	26	366" × 258"	170°		1016	3	
NGC 3368	10 ^h 46 ^m 45 ^s .740	+11°49'11".80	30	354" × 258"	5°	3	891	2	
NGC 3370	10 ^h 47 ^m 04 ^s .051	+17°16'25".04	26	186" × 138"	148°		1272	3	
NGC 3437	10 ^h 52 ^m 35 ^s .75	+22°56'02".9		186" × 114"	122°		1277	3	
NGC 3471	10 ^h 59 ^m 09 ^s .012	+61°31'50".46	26	150" × 102"	14°		2120	3	
NGC 3521	11 ^h 05 ^m 48 ^s .5810	-00°02'09".110	27	558" × 342"	166°	7	798	3, 4	
NGC 3556	11 ^h 11 ^m 30 ^s .97	+55°40'26".8		390" × 162"	80°		699	2	
NGC 3583	11 ^h 14 ^m 10 ^s .890	+48°19'06".67	26	174" × 150"	125°		2126	3	
NGC 3627	11 ^h 20 ^m 14 ^s .964	+12°59'29".54	8	402" × 234"	176°	7	724	3	
NGC 3628	11 ^h 20 ^m 16 ^s .970	+13°35'22".86	8	690" × 198"	104°		844	2	
NGC 3655	11 ^h 22 ^m 54 ^s .617	+16°35'24".11	26	138" × 114"	30°		1466	3	
NGC 3672	11 ^h 25 ^m 02 ^s .47	-09°47'43".4		222" × 138"	12°		1846	3	
NGC 3675	11 ^h 26 ^m 08 ^s .58	+43°35'09".3		306" × 210"	178°		770	2	
NGC 3686	11 ^h 27 ^m 43 ^s .970	+17°13'27".06	26	186" × 162"	15°		1152	3	
NGC 3810	11 ^h 40 ^m 58 ^s .760	+11°28'16".10	24	222" × 186"	24°	10	991	2	
NGC 3813	11 ^h 41 ^m 18 ^s .657	+36°32'48".50	26	150" × 126"	87°		1462	2	
NGC 3888	11 ^h 47 ^m 34 ^s .370	+55°58'02".00	23	138" × 126"	120°		2396	3	
NGC 3893	11 ^h 48 ^m 38 ^s .19	+48°42'39".0		246" × 174"	165°		977	2	
NGC 3938	11 ^h 52 ^m 49 ^s .45	+44°07'14".6		270" × 258"	180°	15	813	2	
NGC 3949	11 ^h 53 ^m 41 ^s .720	+47°51'31".34	26	186" × 138"	120°		803	2	
UGC 6973	11 ^h 58 ^m 52 ^s .201	+42°43'20".91	26	198" × 138"	43°		708	2	
NGC 4027	11 ^h 59 ^m 30 ^s .17	-19°15'54".8		210" × 174"	167°		1658	3	
NGC 4030	12 ^h 00 ^m 23 ^s .627	-01°06'00".34	26	234" × 198"	27°		1453	§§§	3
NGC 4041	12 ^h 02 ^m 12 ^s .202	+62°08'14".00	26	186" × 186"	70°	13	1238	2	
NGC 4045	12 ^h 02 ^m 42 ^s .238	+01°58'36".51	26	186" × 150"	95°		1968	3	
NGC 4085	12 ^h 05 ^m 22 ^s .710	+50°21'10".63	26	174" × 102"	78°		758	3	
NGC 4088	12 ^h 05 ^m 34 ^s .19	+50°32'20".5		294" × 162"	43°		766	2	
NGC 4214	12 ^h 15 ^m 39 ^s .17	+36°19'36".8		474" × 402"	65°	8	297	2	
NGC 4258	12 ^h 18 ^m 57 ^s .5046	+47°18'14".303	9	786" × 366"	176°	3	455	2	
NGC 4303	12 ^h 21 ^m 54 ^s .895	+04°28'25".13	2	318" × 306"	138°	2	1563	2	
NGC 4433	12 ^h 27 ^m 38 ^s .59	-08°16'42".3		150" × 102"	5°		2971	3	
NGC 4527	12 ^h 34 ^m 08 ^s .421	+02°39'13".19	8 **	330" × 186"	67°		1727	3	
NGC 4536	12 ^h 34 ^m 27 ^s .050	+02°11'17".29	26	330" × 186"	125°	11	1796	3	
NGC 4559	12 ^h 35 ^m 57 ^s .647	+27°57'35".97	8	546" × 270"	150°	15	820	3	
NGC 4579	12 ^h 37 ^m 43 ^s .5220	+11°49'05".498	12	294" × 258"	95°	6	1516	2	
NGC 4605	12 ^h 39 ^m 59 ^s .38	+61°36'33".1		306" × 174"	125°		153	2	
NGC 4602	12 ^h 40 ^m 36 ^s .85	-05°07'58".8		186" × 102"	103°	4	2528	3	
NGC 4632	12 ^h 42 ^m 32 ^s .03	-00°04'57".4		198" × 126"	63°		1711	3	

Table 3. (Continued)

Galaxy (1)	$\alpha_{J2000.0}$ (2)	$\delta_{J2000.0}$ (3)	(4)	Mapping size (5)	PA of +X (6) (7)	$V_{LSR}(\text{km s}^{-1})$ (8) (9)	Season (10)	
NGC 4666	12 ^h 45 ^m 08 ^s .591	-00°27'42".79	26	246" × 126"	42°		1516	3
NGC 4750	12 ^h 50 ^m 07 ^s .271	+72°52'28".72	8	162" × 162"	130°	4	1616	3
NGC 4753	12 ^h 52 ^m 22 ^s .11	-01°11'58".9		246" × 174"	80°		1235	3
NGC 4818	12 ^h 56 ^m 48 ^s .90	-08°31'31".1		210" × 114"	180°		1074	3
NGC 5005	13 ^h 10 ^m 56 ^s .231	+37°03'33".14	3	306" × 186"	65°	3	953	2
NGC 5055	13 ^h 15 ^m 49 ^s .33	+42°01'45".4		618" × 414"	105°	15	514	4
NGC 5248	13 ^h 37 ^m 32 ^s .024	+08°53'06".64	26	318" × 258"	110°	10	1157	2
NGC 5364	13 ^h 56 ^m 12 ^s .00	+05°00'52".1		294" × 210"	30°		1245	3
NGC 5480	14 ^h 06 ^m 21 ^s .579	+50°43'30".38	26	138" × 114"	180°		1858	3
NGC 5678	14 ^h 32 ^m 05 ^s .610	+57°55'17".20	22	210" × 138"	5°		1924	2
NGC 5665	14 ^h 32 ^m 25 ^s .742	+08°04'43".11	26	162" × 126"	145°		2209	3
NGC 5676	14 ^h 32 ^m 46 ^s .846	+49°27'28".45	26	234" × 150"	47°		2114	2
NGC 5713	14 ^h 40 ^m 11 ^s .505	-00°17'20".31	26	198" × 174"	10°		1882	3
NGC 5792	14 ^h 58 ^m 22 ^s .71	-01°05'27".9		366" × 150"	84°		1923	3
NGC 5907	15 ^h 15 ^m 53 ^s .770	+56°19'43".58	11	534" × 150"	155°		681	2
NGC 6015	15 ^h 51 ^m 25 ^s .23	+62°18'36".1		330" × 162"	28°		846	4
NGC 6503	17 ^h 49 ^m 26 ^s .432	+70°08'39".72	8	318" × 162"	123°	10	59	2
NGC 6574	18 ^h 11 ^m 51 ^s .23	+14°58'54".4		126" × 114"	160°		2284	2
NGC 6643	18 ^h 19 ^m 46 ^s .41	+74°34'06".1		222" × 150"	44°	10	1496	2
NGC 6764	19 ^h 08 ^m 16 ^s .370	+50°55'59".58	4	162" × 126"	62°		2415	4
NGC 6951	20 ^h 37 ^m 14 ^s .09	+66°06'20".3		222" × 210"	157°	7	1434	3
NGC 7331	22 ^h 37 ^m 04 ^s .014	+34°24'55".87	8	474" × 258"	168°	8	830	2
NGC 7448	23 ^h 00 ^m 03 ^s .59	+15°58'49".2		186" × 126"	170°		2183	3
NGC 7479	23 ^h 04 ^m 56 ^s .65	+12°19'22".4		234" × 186"	25°		2366	2
NGC 7541	23 ^h 14 ^m 43 ^s .890	+04°32'03".70	13	198" × 114"	102°		2662	3
NGC 7625	23 ^h 20 ^m 30 ^s .13	+17°13'32".0		138" × 138"	35°	13	1618	3
NGC 7721	23 ^h 38 ^m 48 ^s .65	-06°31'04".3		186" × 114"	20°		1999	3
NGC 7798	23 ^h 59 ^m 25 ^s .50	+20°44'59".5		126" × 126"	100°	13	2389	3
interacting galaxies								
NGC 772 / NGC 770								
	01 ^h 59 ^m 16 ^s .61	+18°59'30"	33 ††	426" × 426"	180°		2425 †††	3
NGC 770	01 ^h 59 ^m 13 ^s .64	+18°57'16".8					2416	
NGC 772	01 ^h 59 ^m 19 ^s .58	+19°00'27".1					2433	
NGC 2207 / IC 2163								
	06 ^h 16 ^m 25 ^s .005	-21°22'27".35	33	438" × 306"	90°		2673 †††	3
NGC 2207	06 ^h 16 ^m 22 ^s .030	-21°22'21".60	28				2701	
IC 2163	06 ^h 16 ^m 27 ^s .980	-21°22'33".10	28				2644	
Arp 283	09 ^h 17 ^m 26 ^s .9	+41°59'48"	18	342" × 342"	180°		1795 †††	1
NGC 2798	09 ^h 17 ^m 22 ^s .793	+41°59'59".02	8				1727	
NGC 2799	09 ^h 17 ^m 31 ^s .03	+41°59'38".7					1743	
Arp 245	09 ^h 45 ^m 45 ^s	-14°20'48"	19	546" × 414"	180°		2336 †††	3
NGC 2992	09 ^h 45 ^m 42 ^s .050	-14°19'34".98	2				2284	
NGC 2993	09 ^h 45 ^m 48 ^s .33	-14°22'05".9					2389	
Arp 094	10 ^h 23 ^m 28 ^s .8	+19°52'54"	18 ††	402" × 342"	180°		1120	2
NGC 3226	10 ^h 23 ^m 27 ^s .0083	+19°53'54".680	1				1161	1
NGC 3227	10 ^h 23 ^m 30 ^s .5790	+19°51'54".180	1				1149	
NGC 4298 / NGC 4302								

Table 3. (Continued)

Galaxy	$\alpha_{J2000.0}$	$\delta_{J2000.0}$	Mapping size	PA of +X	$V_{LSR}(\text{km s}^{-1})$	Season
(1)	(2)	(3)	(4)	(5)	(6) (7)	(8) (9) (10)
	12 ^h 21 ^m 37 ^s .62	+14°36′08″.05	33	366″ × 366″	180°	1124 ††† 4
NGC 4298	12 ^h 21 ^m 32 ^s .760	+14°36′22″.20	25			1140
NGC 4302	12 ^h 21 ^m 42 ^s .480	+14°35′53″.90	25			1108
NGC 4383 / UGC 7504						
	12 ^h 25 ^m 23 ^s .56	+16°26′59″.23	33	282″ × 246″	180°	1686 ††† 3
UGC 7504	12 ^h 25 ^m 21 ^s .60	+16°25′46″.0	20			1667 8
NGC 4383	12 ^h 25 ^m 25 ^s .523	+16°28′12″.46	26			1705
Arp 269	12 ^h 30 ^m 33 ^s .7	+41°40′21″	18 §§	306″ × 306″	180°	307 5 2
NGC 4485	12 ^h 30 ^m 31 ^s .13	+41°42′04″.2				500
NGC 4490	12 ^h 30 ^m 36 ^s .239	+41°38′38″.03	8			585
VV 219	12 ^h 36 ^m 33 ^s .5	+11°14′54″	18	306″ × 306″	180°	2249 ††† 4
NGC 4567	12 ^h 36 ^m 32 ^s .710	+11°15′28″.80	24			2255
NGC 4568	12 ^h 36 ^m 34 ^s .260	+11°14′20″.00	24			2243
Arp 116	12 ^h 43 ^m 36 ^s	+11°34′00″	18	426″ × 426″	180°	1264 ††† 4
NGC 4647	12 ^h 43 ^m 32 ^s .31	+11°34′54″.7	6			1413
NGC 4649	12 ^h 43 ^m 39 ^s .975	+11°33′09″.74	26			1115
Arp 271	14 ^h 03 ^m 25 ^s .5	−06°02′59″	18	390″ × 270″	180°	2617 ††† 3
NGC 5426	14 ^h 03 ^m 24 ^s .85	−06°04′08″.8				2606
NGC 5427	14 ^h 03 ^m 26 ^s .05	−06°01′50″.9				2629
Arp 090	15 ^h 26 ^m 06 ^s .690	+41°40′21″.00	7	162″ × 162″	180°	2610 ††† 4
NGC 5929	15 ^h 26 ^m 06 ^s .161	+41°40′14″.40	3			2556
NGC 5930	15 ^h 26 ^m 07 ^s .941	+41°40′33″.82	3			2665
Arp 284	23 ^h 36 ^m 18 ^s .1	+02°09′21″	18	366″ × 306″	90°	2761 ††† 3
NGC 7714	23 ^h 36 ^m 14 ^s .098	+02°09′18″.58	5			2776
NGC 7715	23 ^h 36 ^m 22 ^s .142	+02°09′23″.45	8			2747

Notes.

Column (1) Galaxy name. Same as the column (1) in table 1.

Columns (2) and (3): Adopted galaxy center coordinates. No remarks in column (4) indicates that the coordinates correspond to the reference position of the observations.

Column (4) Reference and notes of the galaxy center that is listed on the top of NED. No remarks: Two Micron All Sky Survey Team 2003. 1: Anderson & Ulvestad 2005. 2: Argyle & Eldridge 1990. 3: Becker et al. 1995. 4: Clements 1981. 5: Clements 1983. 6: Condon & Broderick 1991. 7: Condon et al. 1998. 8: Evans et al. 2010. 9: Herrnstein et al. 2005. 10: Jackson et al. 2007. 11: Kautsch et al. 2006. 12: Krips 2007. 13: Li et al. 1998. 14: Liu & Bregman 2005. 15: Minchin et al. 2010. 16: Monet 1998. 17: Nagar et al. 2002. 18: NEDTEAM 2011. 19: NEDTEAM 2012. 20: Paturel et al. 2000. 21: Petrov & Taylor 2011. 22: SDSS DR2. 23: SDSS DR3. 24: SDSS DR4. 25: SDSS DR5. 26: SDSS DR6. 27: Stone et al. 1999. 28: Two Micron All Sky Survey Team 2000. 29: Vigott et al. 1989. 30: Villi et al. 1998. 31: Whiting et al. 2007. 32: XMM-Newton Serendipitous Source Catalogue. 33: Averaged the coordinates of the two galaxies.

*: Observed in the Galactic coordinates, $(l, b) = (127^{\circ}40'11''.939, 27^{\circ}42'33''.173)$.†: Observed in the Galactic coordinates, $(l, b) = (129^{\circ}14'20''.697, 27^{\circ}32'47''.348)$.‡: We observed NGC 2775 wrongly with the reference position of $(\alpha_{J2000.0}, \delta_{J2000.0}) = (09^{\text{h}}10^{\text{m}}20^{\text{s}}.12, +07^{\circ}02'16''.06)$.§: We observed NGC 3079 with the reference position of $(\alpha_{J2000.0}, \delta_{J2000.0}) = (10^{\text{h}}01^{\text{m}}57^{\text{s}}.80, +55^{\circ}40'47''.2)$.||: We observed NGC 3169 with the reference position of $(\alpha_{J2000.0}, \delta_{J2000.0}) = (10^{\text{h}}14^{\text{m}}15^{\text{s}}.050, +03^{\circ}27'57''.875)$.‡: We observed NGC 3147 with the reference position of $(\alpha_{J2000.0}, \delta_{J2000.0}) = (10^{\text{h}}16^{\text{m}}53^{\text{s}}.65, +73^{\circ}24'02''.695)$.***: We observed NGC 4527 wrongly with the reference position of $(\alpha_{J2000.0}, \delta_{J2000.0}) = (12^{\text{h}}34^{\text{m}}08^{\text{s}}.427, +02^{\circ}39'13''.19)$.

††: We adopted the declination different from the average of both galaxies to avoid observing a large blank sky.

‡‡: We observed Arp 094 wrongly with the reference position of $(\alpha_{J2000.0}, \delta_{J2000.0}) = (10^{\text{h}}23^{\text{m}}28^{\text{s}}.08, +19^{\circ}52'54''.)$

§§: The original reference is unidentified.

Column (5) Mapping size in the observation coordinates, X (major axis) \times Y (minor axis).

Column (6) Position angle (PA) of the direction of +X.

Column (7) Reference and notes of PA. No remarks: de Vaucouleurs et al. 1991. 1: Fingerhut et al. 2010. 2: Guhathakurta et al. 1988. 3: Helfer et al. 2003. 4: Jarrett et al. 2003. 5: Koda et al. 2002. 6: Koopmann et al. 2001. 7: Kuno et al. 2007. 8: Leroy et al. 2009. 9: Moshir et al. 1990. 10: Nishiyama & Nakai 2001. 11: Paturel et al. 2003. 12: SDSS DR6. 13: Two Micron All Sky Survey Team 2003. 14: Vaduvescu & McCall 2008. 15: Wilson et al. 2012.

||||: Not kinematically determined but PA of observation.

Column (8) Tracking velocity with respect to the local standard of rest (LSR) in radio definition. In most cases, it corresponds to the receding velocity of galaxies.

Column (9) Reference and notes of V_{LSR} . No remarks: de Vaucouleurs et al. 1991. 1: Boselli et al. 2014a. 2: Bushouse et al. 1998. 3: Huchra et al. 1999. 4: Kuno et al. 2007. 5: NEDTEAM 1992. 6: Springob et al. 2005. 7: Theureau et al. 1998. 8: Toloba et al. 2014. 9: Wilson et al. 2012. 10: Yamauchi et al. 2004. ‡‡: We adopted a wrong value. $V_{LSR} = 1737 \text{ km s}^{-1}$ is the correct value. ***: Not referring NED. †††: Averaged the two galaxies values. ‡‡‡: We miscalculated the average velocity of the two galaxies, and the adopted value differed by 60 km s^{-1} from both galaxies. §§§: We adopted a wrong value. $V_{LSR} = 1452 \text{ km s}^{-1}$ is the correct value. |||||: The value listed in the reference differs by more than 200 km s^{-1} from both galaxies.

Column (10) Observation period in table 2.

Table 4. Measured radius, stellar mass, ^{12}CO luminosity, and molecular gas mass.

galaxy	$R_{3.4\ \mu\text{m}}$ (arcsec)	$\log_{10} M_{\text{star}}(M_{\odot})$	$\log_{10} L'_{12\text{CO}}(\text{K km s}^{-1} \text{pc}^2)$	$\log_{10} M_{\text{mol}}(M_{\odot})$
isolated galaxies				
IC 10	339	$8.423 \pm .008$ *	$5.915 \pm .008$	$6.551 \pm .008$
NGC 150	129	$10.425 \pm .010$	$8.391^{+.013}_{-.014}$	$9.027^{+.013}_{-.014}$
NGC 157	156	$10.156 \pm .009$	$8.412 \pm .004$	$9.049 \pm .004$
NGC 278	105	$10.336^{+.009}_{-.010}$	$8.693 \pm .005$	$9.329 \pm .005$
NGC 337	99	$9.953 \pm .009$	$8.036^{+.014}_{-.015}$	$8.672^{+.014}_{-.015}$
NGC 470	109	$10.732 \pm .010$	$8.805 \pm .012$	$9.441 \pm .012$
NGC 520	155	$9.462 \pm .009$	$7.973 \pm .003$	$8.609 \pm .003$
NGC 613	187	$11.086 \pm .010$	$9.395 \pm .004$	$10.031 \pm .004$
NGC 628	277	$10.247^{+.009}_{-.010}$	$8.653 \pm .003$	$9.289 \pm .003$
NGC 660	247	$10.436 \pm .010$	$9.029 \pm .002$	$9.665 \pm .002$
NGC 701	102	$10.018 \pm .009$	$8.140^{+.014}_{-.015}$	$8.776^{+.014}_{-.015}$
NGC 891	401	$10.638 \pm .010$	$9.192 \pm .001$	$9.828 \pm .001$
NGC 1022	129	$10.185^{+.009}_{-.010}$	$8.444 \pm .008$	$9.080 \pm .008$
NGC 1055	215	$10.844 \pm .010$ †	$9.327 \pm .003$	$9.963 \pm .003$
NGC 1084	179	$10.581 \pm .010$	$8.875 \pm .005$	$9.511 \pm .005$
NGC 1087	116	$10.002 \pm .009$	$8.139^{+.010}_{-.011}$	$8.775^{+.010}_{-.011}$
NGC 1156	149	$9.182^{+.008}_{-.009}$	$6.941^{+.030}_{-.032}$	$7.577^{+.030}_{-.032}$
NGC 1241	109	$11.142 \pm .010$	$9.339 \pm .009$	$9.975 \pm .009$
UGC 2765	140	$10.236^{+.009}_{-.010}$	$8.317 \pm .009$	$8.953 \pm .009$
NGC 1482	121	$10.311^{+.009}_{-.010}$	$8.728 \pm .005$	$9.364 \pm .005$
UGCA 86	30	$6.729 \pm .006$ ‡	$5.906 \pm .017$ §	$6.542 \pm .017$ §
IC 356	298	$11.318^{+.010}_{-.011}$ *	$9.179 \pm .004$	$9.815 \pm .004$
NGC 1530	167	$10.424 \pm .010$	$8.882 \pm .005$	$9.518 \pm .005$
NGC 1569	207	$8.942 \pm .008$	$6.090^{+.034}_{-.037}$ ¶	$6.726^{+.034}_{-.037}$ ¶
NGC 2146	261	$11.285^{+.010}_{-.011}$	$9.818 \pm .002$	$10.454 \pm .002$
NGC 2273	118	$10.665 \pm .010$	$8.776 \pm .009$	$9.412 \pm .009$
NGC 2339	101	$10.790 \pm .010$	$9.073 \pm .006$	$9.709 \pm .006$
NGC 2268	132	$10.618 \pm .010$	$8.914 \pm .008$	$9.550 \pm .008$
NGC 2276	180	$10.866 \pm .010$ **	$9.337 \pm .005$	$9.973 \pm .005$
NGC 2633	94	$10.406 \pm .010$	$9.041 \pm .004$	$9.677 \pm .004$
NGC 2681	151	$10.427 \pm .010$	$8.315 \pm .008$	$8.951 \pm .008$
NGC 2742	113	$10.421 \pm .010$	$8.528 \pm .012$	$9.164 \pm .012$
NGC 2715	158	$10.010 \pm .009$	$8.329^{+.008}_{-.009}$	$8.965^{+.008}_{-.009}$
NGC 2775	209	$10.712 \pm .010$	$8.408 \pm .009$	$9.044 \pm .009$
NGC 2748	130	$10.121 \pm .009$	$8.301^{+.010}_{-.011}$	$8.937^{+.010}_{-.011}$
NGC 2782	148	$9.938 \pm .009$	$8.238^{+.009}_{-.010}$	$8.874^{+.009}_{-.010}$
NGC 2841	453	$10.898 \pm .010$	$8.660 \pm .004$	$9.296 \pm .004$
NGC 2903	438	$10.608 \pm .010$	$9.013 \pm .002$	$9.649 \pm .002$
NGC 2967	101	$10.208^{+.009}_{-.010}$	$8.713 \pm .006$	$9.349 \pm .006$
NGC 2976	282	$9.140^{+.008}_{-.009}$	$7.241 \pm .006$	$7.877 \pm .006$
NGC 2985	235	$10.799 \pm .010$	$8.829 \pm .007$	$9.465 \pm .007$
NGC 3034	663	$10.293^{+.009}_{-.010}$	$8.896 \pm .001$	$9.532 \pm .001$
NGC 3079	317	$10.808 \pm .010$	$9.443 \pm .001$	$10.079 \pm .001$
NGC 3077	265	$9.309 \pm .009$	$7.016^{+.013}_{-.014}$	$7.652^{+.013}_{-.014}$
NGC 3166	179	$10.781 \pm .010$	$8.619 \pm .007$	$9.255 \pm .007$
NGC 3169	182	$10.890 \pm .010$	$9.136 \pm .005$	$9.772 \pm .005$
NGC 3177	55	$10.110 \pm .009$	$8.622 \pm .005$	$9.258 \pm .005$

Table 4. (Continued)

galaxy	$R_{3.4\ \mu\text{m}}$ (arcsec)	$\log_{10} M_{\text{star}} (M_{\odot})$	$\log_{10} L'_{12\ \text{CO}} (\text{K km s}^{-1} \text{ pc}^2)$	$\log_{10} M_{\text{mol}} (M_{\odot})$
NGC 3147	144	$11.268^{+0.010}_{-0.011}$	$9.660 \pm .003$	$10.296 \pm .003$
NGC 3198	329	$10.128 \pm .009$	$8.375 \pm .006$	$9.011 \pm .006$
Mrk 33	52	$9.581 \pm .009$	$7.409^{+0.049}_{-0.055}$	$8.046^{+0.049}_{-0.055}$
NGC 3310	174	$9.829 \pm .009$	$7.971 \pm .008$	$8.607 \pm .008$
NGC 3338	217	$10.479 \pm .010 \dagger\dagger$	$9.046 \pm .005$	$9.682 \pm .005$
NGC 3344	214	$10.077 \pm .009$	$8.182 \pm .008$	$8.818 \pm .008$
NGC 3351	239	$10.388 \pm .010$	$8.578 \pm .004$	$9.214 \pm .004$
NGC 3367	89	$10.497 \pm .010$	$8.768 \pm .007$	$9.404 \pm .007$
NGC 3359	226	$10.300^{+0.009}_{-0.010}$	$8.924 \pm .006$	$9.560 \pm .006$
NGC 3368	346	$10.520 \pm .010$	$8.373 \pm .005$	$9.009 \pm .005$
NGC 3370	88	$10.093 \pm .009$	$8.375 \pm .013$	$9.011 \pm .013$
NGC 3437	106	$10.286^{+0.009}_{-0.010}$	$8.661 \pm .009$	$9.297 \pm .009$
NGC 3471	64	$9.934 \pm .009$	$8.183 \pm .012$	$8.819 \pm .012$
NGC 3521	474	$11.066 \pm .010$	$9.379 \pm .002$	$10.015 \pm .002$
NGC 3556	391	$10.245^{+0.009}_{-0.010}$	$8.759 \pm .002$	$9.395 \pm .002$
NGC 3583	98	$10.543 \pm .010$	$8.771^{+0.007}_{-0.008}$	$9.407^{+0.007}_{-0.008}$
NGC 3627	334	$10.605 \pm .010 \dagger\dagger$	$9.031 \pm .002$	$9.667 \pm .002$
NGC 3628	441	$10.638 \pm .010$	$9.123 \pm .002$	$9.759 \pm .002$
NGC 3655	65	$10.683 \pm .010$	$9.208 \pm .005$	$9.844 \pm .005$
NGC 3672	145	$10.625 \pm .010$	$8.942 \pm .006$	$9.578 \pm .006$
NGC 3675	345	$10.895 \pm .010$	$9.123 \pm .003$	$9.759 \pm .003$
NGC 3686	111	$10.008 \pm .009$	$8.399 \pm .007$	$9.035 \pm .007$
NGC 3810	148	$10.328^{+0.009}_{-0.010}$	$8.761^{+0.004}_{-0.005}$	$9.397^{+0.004}_{-0.005}$
NGC 3813	154	$10.263^{+0.009}_{-0.010}$	$8.611 \pm .006$	$9.247 \pm .006$
NGC 3888	68	$10.529 \pm .010$	$8.632^{+0.011}_{-0.012}$	$9.268^{+0.011}_{-0.012}$
NGC 3893	183	$10.295^{+0.009}_{-0.010}$	$8.679 \pm .004$	$9.315 \pm .004$
NGC 3938	173	$10.431 \pm .010$	$8.829 \pm .004$	$9.465 \pm .004$
NGC 3949	149	$10.203^{+0.009}_{-0.010}$	$8.149 \pm .011$	$8.785 \pm .011$
UGC 6973	138	$10.544 \pm .010$	$9.001 \pm .004$	$9.637 \pm .004$
NGC 4027	113	$10.272^{+0.009}_{-0.010}$	$8.700^{+0.006}_{-0.007}$	$9.336^{+0.006}_{-0.007}$
NGC 4030	172	$11.077 \pm .010$	$9.506 \pm .003$	$10.142 \pm .003$
NGC 4041	112	$10.685 \pm .010$	$9.236 \pm .005$	$9.872 \pm .005$
NGC 4045	138	$10.628 \pm .010$	$8.891 \pm .009$	$9.527 \pm .009$
NGC 4085	133	$10.023 \pm .009$	$8.340 \pm .010$	$8.976 \pm .010$
NGC 4088	201	$10.390 \pm .010$	$8.910 \pm .003$	$9.546 \pm .003$
NGC 4214	258	$8.864 \pm .008$	$7.141 \pm .010$	$7.777 \pm .010$
NGC 4258	725	$10.551 \pm .010$	$8.732 \pm .002$	$9.368 \pm .002$
NGC 4303	205	$10.773 \pm .010$	$9.334 \pm .003$	$9.970 \pm .003$
NGC 4433	78	$10.625 \pm .010$	$9.103 \pm .006$	$9.739 \pm .006$
NGC 4527	217	$10.688 \pm .010$	$9.222 \pm .003$	$9.858 \pm .003$
NGC 4536	224	$10.464 \pm .010$	$8.725 \pm .005$	$9.361 \pm .005$
NGC 4559	269	$9.679 \pm .009$	$8.164 \pm .005$	$8.800 \pm .005$
NGC 4579	258	$10.839 \pm .010$	$8.831 \pm .005$	$9.467 \pm .005$
NGC 4605	256	$9.401 \pm .009$	$7.214^{+0.013}_{-0.014}$	$7.850^{+0.013}_{-0.014}$
NGC 4602	136	$10.754 \pm .010$	$9.033 \pm .007$	$9.669 \pm .007$
NGC 4632	113	$9.700 \pm .009$	$7.949^{+0.011}_{-0.012}$	$8.585^{+0.011}_{-0.012}$
NGC 4666	220	$10.573 \pm .010$	$8.952 \pm .003$	$9.588 \pm .003$
NGC 4750	128	$10.618 \pm .010$	$8.531 \pm .011$	$9.167 \pm .011$

Table 4. (Continued)

galaxy	$R_{3.4\ \mu\text{m}}$ (arcsec)	$\log_{10} M_{\text{star}} (M_{\odot})$	$\log_{10} L'_{12\text{CO}} (\text{K km s}^{-1} \text{pc}^2)$	$\log_{10} M_{\text{mol}} (M_{\odot})$
NGC 4753	311	$11.146 \pm .010$	$8.709 \pm .009$	$9.345 \pm .009$
NGC 4818	173	$9.940 \pm .009$	$8.196^{+.004}_{-.005}$	$8.832^{+.004}_{-.005}$
NGC 5005	264	$10.922 \pm .010$	$9.148 \pm .003$	$9.784 \pm .003$
NGC 5055	586	$10.737 \pm .010$ ††	$9.213 \pm .002$	$9.849 \pm .002$
NGC 5248	217	$10.369^{+.009}_{-.010}$	$8.958 \pm .003$	$9.594 \pm .003$
NGC 5364	226	$10.445 \pm .010$ ††	$8.636 \pm .008$	$9.272 \pm .008$
NGC 5480	80	$10.226^{+.009}_{-.010}$	$8.871 \pm .008$	$9.507 \pm .008$
NGC 5678	215	$10.895 \pm .010$	$9.394 \pm .003$	$10.030 \pm .003$
NGC 5665	82	$9.790 \pm .009$	$8.035 \pm .011$	$8.671 \pm .011$
NGC 5676	145	$10.940 \pm .010$	$9.415 \pm .003$	$10.051 \pm .003$
NGC 5713	98	$10.296^{+.009}_{-.010}$	$8.830 \pm .004$	$9.466 \pm .004$
NGC 5792	240	$10.931 \pm .010$ §§	$8.896 \pm .007$	$9.532 \pm .007$
NGC 5907	362	$10.814 \pm .010$ ††	$9.076 \pm .003$	$9.712 \pm .003$
NGC 6015	251	$10.257^{+.009}_{-.010}$	$8.251 \pm .013$	$8.887 \pm .013$
NGC 6503	343	$9.682 \pm .009$	$7.655 \pm .006$	$8.291 \pm .006$
NGC 6574	64	$10.974 \pm .010$	$9.367 \pm .006$	$10.003 \pm .006$
NGC 6643	138	$10.471 \pm .010$	$8.874 \pm .005$	$9.510 \pm .005$
NGC 6764	133	$10.117 \pm .009$	$8.330^{+.012}_{-.013}$	$8.966^{+.012}_{-.013}$
NGC 6951	154	$10.873 \pm .010$ ††	$9.091 \pm .005$	$9.727 \pm .005$
NGC 7331	470	$10.935 \pm .010$	$9.256 \pm .002$	$9.892 \pm .002$
NGC 7448	88	$10.346^{+.009}_{-.010}$	$8.674 \pm .008$	$9.310 \pm .008$
NGC 7479	154	$11.029 \pm .010$	$9.427 \pm .004$	$10.063 \pm .004$
NGC 7541	147	$10.787 \pm .010$	$9.070 \pm .006$	$9.706 \pm .006$
NGC 7625	64	$10.188^{+.009}_{-.010}$	$8.701 \pm .005$	$9.337 \pm .005$
NGC 7721	120	$10.411 \pm .010$	$8.521 \pm .011$	$9.157 \pm .011$
NGC 7798	56	$10.301^{+.009}_{-.010}$	$8.628 \pm .008$	$9.264 \pm .008$
interacting galaxies				
NGC 772 / NGC 770		$11.186 \pm .010$	$9.680 \pm .004$	$10.316 \pm .004$
NGC 770	101	$9.988 \pm .009$	$8.715^{+.012}_{-.013}$	$9.351^{+.012}_{-.013}$
NGC 772	228	$11.157 \pm .010$	$9.631 \pm .004$	$10.267 \pm .004$
NGC 2207 / IC 2163		$11.123 \pm .007$	$9.364 \pm .006$	$10.000 \pm .006$
NGC 2207	119	$10.888 \pm .010$	$9.093 \pm .009$	$9.729 \pm .009$
IC 2163	95	$10.745 \pm .010$	$9.030 \pm .009$	$9.666 \pm .009$
Arp 283		$10.449^{+.008}_{-.009}$	$8.780 \pm .009$	$9.416 \pm .009$
NGC 2798	94	$10.392 \pm .010$	$8.732 \pm .009$	$9.368 \pm .009$
NGC 2799	101	$9.542 \pm .009$	$7.801^{+.035}_{-.038}$	$8.437^{+.035}_{-.038}$
Arp 245		$10.716 \pm .008$	$8.973 \pm .008$	$9.609 \pm .008$
NGC 2992	160	$10.614 \pm .010$	$8.742 \pm .011$	$9.378 \pm .011$
NGC 2993	66	$10.036 \pm .009$	$8.589 \pm .011$	$9.225 \pm .011$
Arp 094		$10.748 \pm .007$	$9.201 \pm .004$	$9.837 \pm .004$
NGC 3226	172	$10.256^{+.009}_{-.010}$	$8.774^{+.007}_{-.008}$	$9.410^{+.007}_{-.008}$
NGC 3227	240	$10.579 \pm .010$	$8.997 \pm .005$	$9.633 \pm .005$
NGC 4298 / NGC 4302		$10.537 \pm .007$	$9.043 \pm .004$	$9.679 \pm .004$
NGC 4298	153	$10.091 \pm .009$	$8.773 \pm .005$	$9.409 \pm .005$
NGC 4302	255	$10.344^{+.009}_{-.010}$	$8.709 \pm .005$	$9.345 \pm .005$
NGC 4383 / UGC 7504		$9.751^{+.008}_{-.009}$	$8.483 \pm .006$	$9.119 \pm .006$
UGC 7504	75	$8.481 \pm .008$	$7.691^{+.015}_{-.016}$	$8.327^{+.015}_{-.016}$
NGC 4383	83	$9.727 \pm .009$	$8.407 \pm .006$	$9.043 \pm .006$

Table 4. (Continued)

galaxy	$R_{3.4\ \mu\text{m}}$ (arcsec)	$\log_{10} M_{\text{star}} (M_{\odot})$	$\log_{10} L'_{12\text{CO}} (\text{K km s}^{-1} \text{ pc}^2)$	$\log_{10} M_{\text{mol}} (M_{\odot})$
Arp 269		$9.438 \pm .008$	$7.335 \pm .007$	$7.971 \pm .007$
NGC 4485	113	$8.363 \pm .008$	$6.633^{+.017}_{-.018}$	$7.269^{+.017}_{-.018}$
NGC 4490	243	$9.400 \pm .009$	$7.238 \pm .007$	$7.874 \pm .007$
VV 219		$10.575 \pm .007$	$9.124 \pm .003$	$9.760 \pm .003$
NGC 4567	147	$10.084 \pm .009$	$8.616 \pm .006$	$9.252 \pm .006$
NGC 4568	183	$10.406 \pm .010$	$8.963 \pm .003$	$9.599 \pm .003$
Arp 116		$11.237 \pm .009$	$8.993 \pm .004$	$9.629 \pm .004$
NGC 4647	255	$10.419 \pm .010$	$8.808 \pm .005$	$9.444 \pm .005$
NGC 4649	417	$11.165 \pm .010$	$8.531 \pm .009$	$9.167 \pm .009$
Arp 271		$10.985^{+.007}_{-.008}$	$9.557 \pm .004$	$10.193 \pm .004$
NGC 5426	100	$10.501 \pm .010$	$9.047 \pm .008$	$9.683 \pm .008$
NGC 5427	108	$10.812 \pm .010$	$9.397 \pm .005$	$10.033 \pm .005$
Arp 090		$10.744 \pm .007$	$8.421^{+.020}_{-.021}$	$9.057^{+.020}_{-.021}$
NGC 5929	80	$10.292^{+.009}_{-.010}$	$7.900^{+.039}_{-.043}$	$8.536^{+.039}_{-.043}$
NGC 5930	71	$10.554 \pm .010$	$8.266^{+.022}_{-.024}$	$8.902^{+.022}_{-.024}$
Arp 284		$10.472 \pm .009$	$9.021 \pm .009$	$9.657 \pm .009$
NGC 7714	80	$10.428 \pm .010$	$8.874^{+.010}_{-.011}$	$9.510^{+.010}_{-.011}$
NGC 7715	118	$9.462 \pm .009$	$8.478^{+.015}_{-.016}$	$9.114^{+.015}_{-.016}$

Notes.

Column (1): Galaxy name. Same as the column (1) in table 1.

Column (2): The $3.4\ \mu\text{m}$ radius ($R_{3.4\ \mu\text{m}}$) in arcsec.Column (3): Logarithmic total stellar mass in M_{\odot} .Column (4): Logarithmic total integrated intensity of ^{12}CO in $\text{K km s}^{-1} \text{ pc}^2$.Column (5): Logarithmic total molecular gas mass in M_{\odot} .

*: Uncertain because of many foreground stars.

†: Slightly uncertain due to a foreground bright star and a spider diffraction pattern.

‡: Uncertain due to a foreground star cluster.

§: Uncertain due to the Galactic emission.

||: Uncertain because of several foreground stars, including a bright one and spider diffraction patterns.

‡: Slightly lower limit due to masking the channel corresponding to the Galactic emission.

***: Uncertain due to two foreground stars and spider diffraction patterns.

††: Slightly uncertain because of a foreground bright star.

†††: Slight upper limit caused by not masking two slightly bright stars on the galaxy.

§§: Upper limit due to a foreground bright star and spider diffraction patterns.

Table 5. Correlation between the total molecular gas mass fraction and the total stellar mass.

Morphology	Samples	Power*	Correlation coefficient	Remarks
Hubble types				
E – S0/a	7	-1.09	-0.92	
Sa	13	-0.27	-0.52	
Sab	10	0.27	0.28	†
Sb	23	-0.15	-0.16	‡
Sbc	34	0.09	0.21	
Sc	39	0.22	0.46	§
Scd – Sm	8	0.30	0.40	
I, pec, dIrr	13	-0.27	-0.39	
with or without a bar				
SA	47	0.03	0.05	†
SAB	44	-0.01	-0.02	§
SB	36	0.18	0.48	‡
SAB + SB	80	0.10	0.25	**

*: Index a in $M_{\text{mol}}/M_{\text{star}} \propto M_{\text{star}}^a$.

†: IC 356 is included in the number of samples, but not in the statistics.

‡: NGC 5792 is included in the number of samples, but not in the statistics.

§: NGC 2276 is included in the number of samples, but not in the statistics.

||: IC 10 and NGC 1569 are included in the number of samples, but not in the statistics.

‡: IC 10, NGC 1569, and NGC 5792 are included in the number of samples, but not in the statistics.

** : IC 10, NGC 1569, NGC 2276, and NGC 5792 are included in the number of samples, but not in statistics.